AQUEOUS BIPHASIC 3D CELL CULTURE MICRO-TECHNOLOGY

A Dissertation

Presented to

The Graduate Faculty of The University of Akron

In Partial Fulfillment

of the Requirements for the Degree

Doctor of Philosophy

Ehsan Atefi

December, 2015

AQUEOUS BIPHASIC 3D CELL CULTURE MICRO-TECHNOLOGY

Ehsan Atefi

Dissertation

Approved:

_____
Advisor
Dr. Hossein Tavana

_____
Committee Member
Dr. Rebecca. K. Willits

_____
Committee member
Dr. Gang Cheng

_____
Committee member
Dr. Yang. H. Yun

_____
Committee member
Dr. Ali Dhinojwala

Accepted:

_____
Department Chair
Dr. Brian Davis

_____
Dean of the College
Dr. Rex Ramsier

_____
Interim Dean of the Graduate School
Dr. Chand Midha

_____
Date

ABSTRACT

Three-dimensional (3D) cell culture technologies have gained a considerable momentum in compound screening applications to identify novel anti-cancer drugs. Increasing evidence shows substantial differences between responses of cancer cells to drug compounds in monolayer cultures (2D) traditionally used in drug discovery and in vivo during preclinical tests. 3D cell cultures more closely resemble tumors in terms of close cell-cell and cell-extracellular matrix interactions, non-uniform distribution of soluble factors, and presence of hypoxic cells. As such, they provide a relevant tumor model to elicit more realistic responses from cells treated with drugs. Screening of libraries of compounds to identify novel drugs requires high throughput 3D culture platforms that produce consistently sized cancer cell spheroids and allow convenient drug testing and analysis of cellular responses.

In this study, we introduce a novel, automated technology for 3D culture of cancer cell spheroids in a high throughput format. Aqueous two-phase systems (ATPS) are used for producing spheroids with robotic tools and standard equipment. ATPS are formed by mixing appropriate mass concentrations of two biocompatible polymers such as dextran (DEX) and polyethylene glycol (PEG). A nano-liter drop of the denser aqueous DEX phase containing cancer cells is robotically dispensed into each well of a non-adherent 96-well plate containing the immersion PEG phase solution. A round drop containing cells forms at the bottom of the well while overlaid with the aqueous PEG phase. Cells remain in the

DEX drop and form a spheroid, which receives nutrients from the immersion phase through diffusion into the drop.

The fidelity of the ATPS spheroid culture technology depends on favorable partition of cells to the DEX drop. We investigate partition of cancer cells in ATPS and demonstrate the effect of interfacial tension between the two aqueous phases on the distribution of cells in ATPS. To facilitate this study, we determine ultralow interfacial tensions of ATPS using an axisymmetric drop shape analysis (ADSA) methodology with sessile and pendant drops and develop mathematical criteria for reliable measurements. To develop a fundamental understanding of the role of interfacial tension of ATPS in cell partition, we develop a theoretical model to predict the energy associated with displacement of a particle (cell) in ATPS. This model, which also uses our contact angle measurements with ATPS/cell systems as an input, shows that a very small interfacial tension, i.e., on the scale of ~30 $\mu J/m^2$, results in a minimum free energy when cells locate in the bottom DEX phase, corroborating with our experimental cell partition data and spheroid formation with ATPS. Finally, the utility of this new technology for compound screening is demonstrated by high throughput testing of several anti-cancer drugs against spheroids of skin and breast cancer cells. Incorporating this robotic technology in the oncology drug discovery pipeline will expedite discovery of novel anti-cancer drugs with a relevant tumor model.

ACKNOWLEDGEMENTS

First and foremost, I would like to express my sincere gratitude to my research advisor, Dr. Hossein Tavana for his guidance, patience, support and enthusiastic encouragement toward the development of my researches at The University of Akron. Besides completing a PhD dissertation, he directed me in publishing papers and presenting my researches. During my PhD study, he was always there to give me necessary support and assistance. Without his support, I could not have completed my research.

I would like to thank Dr. Rebecca. K. Willits, Dr. Ali Dhinojwala, Dr. Yang. H. Yun, and Dr. Gang Cheng for serving as my committee members and providing valuable insights to elevate the quality of my research.

Special thanks go to Dr. J. Adin Mann for all his helps and supports. He was always there to listen and provide me with sincere advices, encouragements and guidance. I would also like to thank Dr. Dale H. Mugler for providing valuable helps and comments. He has provided, with kindness, valuable suggestions which are precious to me.

I would like to thank my friends and colleagues for their helps. My gratitude is also extended to my family, for the endless support, deep love, and continuous encouragement. I am forever grateful to them, and I would like to dedicate this work to my family.

TABLE OF CONTENTS

LIST OF FIGURES

Figure Page

LIST OF TABLES

CHAPTER I

INTRODUCTION

Cancer, a group of diseases involving abnormal function of cells, accounts for 12.5% of deaths all around the world according to the statistics published by the World Health Organization[1]. The National Cancer Institute estimates that there will be 1,658,370 new cases diagnosed and 589,430 deaths will occur in 2015, only in the United States. This ranks cancer as the second leading cause of mortality in the United States. It is estimated that more than 39% of people will experience cancer during their lifetime[1]. Some recent statistics show that approximately $125 billion was spent for cancer care in 2010 that could reach $156 billion in 2020[1]. As such, cancer is a major burden both on individuals and on the global economy, underlying the importance of studies to better understand the disease and to develop effective therapies[1].

In addition to surgery, there are two main therapies for cancer: radiation therapy and chemotherapy[2]. The goal of radiation therapy is to damage the DNA of cancer cells, making them undergo programmed cell death, apoptosis. Nevertheless, recent studies show that some cancer cells may become resistant to this therapy and evade apoptosis. In addition, despite being a localized treatment, radiotherapy generates side effects including damage to red blood cells and surrounding normal cells in the tissue[3]. Chemotherapies are also used to prevent cell growth and induce apoptosis. These drugs work primarily on actively dividing cells through impairing specific or all stages of cell cycle. Major types of

chemotherapeutics are: (i) alkylating agents that directly target DNA of cells at any stage of cell cycle, (ii) antimetabolites that interfere with DNA and RNA through substituting for normal building blocks, (iii) antibiotics that interfere with enzymes involved in DNA replication, and (iv) mitotic inhibitors that prevent replication of cells by inhibiting cells from entering the mitosis phase[4]. In addition to inducing cancer cell death, traditional chemotherapies are toxic to normal cells and generate major side effects[4], [5].

Recent progress in developing high throughput screening technologies has helped decipher alterations in gene expression of cancer cells and resulting changes in activation of certain molecular pathways for specific cancers. This information has been used to develop targeted therapeutics against specific molecules (genes or proteins) that are abundant in cancer cells as a strategy to reduce toxic effects on normal cells[6]. Small molecule inhibitors of genes and proteins and hormonal therapy compounds to block/reduce production of hormones necessary for cancer cell growth are examples of targeted therapeutics. Significant advancement in the understanding of biology of cancers combined with better detection and treatment regimens have resulted in higher survival rates of patients in most cancers, including lung, breast, and prostate[7], [8]. Nevertheless, survival rates drop sharply at advanced stages of the disease and remain high for less studied cancers such as melanoma[1]. For example according to the American Cancer Society, the 5-year survival rate for breast cancer patients drops from 100% at stage I to only 22% at stage IV[1]. Considering that chemotherapy is the main treatment option for most cancer patients and that existing drugs barely cure patients, there is still a major need for developing more effective anti-cancer drugs to improve disease-free survival.

Discovery of new drugs is a highly time, money, and resource consuming process[9], [10]. A collection of thousands of compounds undergoes target validation, lead discovery, and medicinal chemistry to select a library of few hundred compounds for subsequent in vitro screening with cellular disease models. At this step, the affinity and selectivity of compounds against cells of interest is studied using various assays to refine the library for candidate compounds for in vivo animal tests. Compounds showing efficacy in animal models may be approved for three phases of clinical trials with volunteer human patients[11]. This process often takes about ten years to complete, generates an expense of ~ $2-3 billion, and leads to a single drug or two for final approval by the US Food and Drug Administration (FDA). During 1997-2011, twelve major pharmaceutical companies spent a combined $802,428 billion on drug research and development, with Pfizer, Inc. leading the pack spending a total of $108,178 billion. While there were almost 900 anti-cancer drug candidates in clinical trials or under FDA review in 2011, only twelve were actually approved that year[12].

It is believed that a major contributor to this inefficiency is the use of irrelevant cellular disease models for screening of compounds libraries. Traditionally, pharmaceutical companies have been testing chemical compounds with monolayer of cells of interest to determine the efficacy of the compounds to eliminate cancer cells and understand underlying molecular mechanisms and pathways involved[6], [13]–[16]. A primary reason for interest in the use of monolayer (two-dimensional, 2D) cell cultures is the ease of forming cultures in microwell plates and the compatibility of these platforms with standard robotic screening tools for drug and reagent addition and downstream analysis of cellular responses. However, recent molecular analyses of cells have identified

considerable differences at gene and protein expression levels between cells harvested from tumors and cells in monolayer cultures[8], [17], [18]. Monolayer cell cultures lack major factors of tumor microenvironment including intimate intercellular interactions between cancer cells and between cancer cells and stromal cells, cancer cells-extracellular matrix interactions, and concentration profiles of endogenous and exogenous chemical compounds (Figure 1-1)[19], [20], [21]. Hence, majority of compounds that show high efficacy against 2D cultures of cancer cells fail when tested in vivo with animal models or later in clinical trials. For example, it is substantiated that close cell-cell interactions between tumor cells can result in resistance to chemotherapies through various mechanisms such as overexpression of the p-glycoprotein 1 (also known as multidrug resistance protein 1, MDR1) that acts as an efflux pump to rid cells of drugs[8]. Clearly, such phenomena cannot be captured with monolayer cultures. It is now recognized that improving the process of anti-cancer drug discovery requires using more realistic in vitro tumor models that better mimic tumor microenvironment in vivo.

1.1. In Vitro Cellular Models for Compound Screening

Under certain conditions, when cancer cells are maintained on a non-adherent surface, cell-cell interactions will result in the formation of a three-dimensional (3D) cluster known as cancer cell spheroid or tumor spheroid. Spheroids present several similar characteristics to avascular or poorly-vascularized tumors[13], [22]–[24]. These include morphological similarities, close cell-cell interactions, gradients of metabolic factors, nutrients, and oxygen due to diffusion limitations, and hypoxia. In a cancer cell spheroid, cells at different stages of cell cycle may exist. This difference in proliferative stage of cells

mimics tumor cells. Therefore only a limited number of these cells may respond to certain chemotherapeutics such as taxanes that target actively proliferating cells. On the other hand, majority of cells in a 2D culture are highly proliferative and produce a uniform response to such drugs[25]–[27]. Limited supply of nutrients and oxygen to cells in the core of spheroids may generate hypoxic cells. The presence of hypoxia is associated with chemotherapy drug resistance through various molecular mechanisms such as overexpression of efflux pumps[4]. Obviously, such phenomena cannot be observed with monolayer cultures due to uniform concentrations of nutrients and oxygen in the culture[28]–[33].

Therefore, available evidence strongly supports incorporating 3D cultures in various areas of cancer research including oncology drug discovery. In the following section, existing methods of 3D culture of cells are briefly reviewed and their advantages and disadvantages are discussed.

1.2. Three-Dimensional (3D) Cell Culture Techniques

Several methods of 3D cell culture have been developed to generate tumor spheroids in vitro. Conventionally, rotary vessels and spinner flasks have been used for spheroid formation. In rotary-wall vessel system, cells are held suspended in a cylinder with rotating walls containing collagen-coated beads. Cells experience a microgravity-free situation, attach to microbeads, and form multiple aggregates. Spinner flasks use a rotary device to constantly mix the cell suspension and keep the cells suspended to cluster into spheroids. Both these approaches require specialized equipment and have experimentally involved protocols that limit their broad application[34].

Liquid overlay technique is an extensively used approach and is based on the use of non-adherent or ultralow-attachment culture plates[35]. The technique involves simple steps of preparing cell suspension and adding a defined volume of the suspension to the culture plate. Cells sink to the bottom of the plate and aggregate. Performing this technique in well plates can generates a large number of spheroids necessary for drug screening applications. However, the possibility of forming a single spheroid in each well with a consistent size distribution and geometry across the plate is difficult and highly dependent on particular cells. Testing compounds on spheroid of varying size/geometry influences the drug pharmacokinetics (such as movement of the drug into and out of the cells and metabolism of the drug) and should be avoided[36]–[41].

Microfluidic models for 3D culture of cells have been developed to generate close cell-cell interactions. Commonly, this approach involves designing devices in which microwells of several hundred micrometers in diameter are embedded[42]. A cell suspension is introduced into the device from an inlet port. Some of flowing cells are trapped in the microwells while the remaining cells exit the device through an outlet port. Cells within wells aggregate and form a spheroid. Various designs have been used to enable drug studies and investigating the effects of hydrodynamic stress, chemical gradients, and fluid flow on anti-cancer drug efficacy[43]. This technique requires device fabrication, which is a costly process. Operating the device requires experience and special trainings. It also exposes all spheroids to a single treatment condition[44]. Other shortcomings of this approach are difficulty of harvesting spheroids for biochemical analyses of drug response of cells, and incompatibility with existing standard screening equipment and robotics for automated addition of drugs and analysis reagents[45].

Traditional hanging drop technique enables formation of uniform spheroids in cell-containing culture media drops held hanging from a substrate[46]. Due to gravity, cells aggregate at the drop apex region and form a spheroid. To allow compound screening with spheroids generated using this technique, a special microwell plate compatible with commercial liquid handlers has been designed[47]. The plate contains arrays of holes to accommodate formation of one spheroid in a drop hanging from the hole. The plate also includes chambers to reduce the evaporation of media from hanging drops that have a volume of 10-30 µl[48], [49]. Although modifications to the traditional hanging drop technique has made this approach compatible with available high throughput equipment, handling of liquid drops and maintenance of the spheroids in culture within drops for several days to weeks is very challenging as drops may fall off the plate or merge. In addition, spheroids must be transferred to a standard microwell plate for any downstream biochemical analysis using standard plate readers[49]. The process of transferring spheroids is also very difficult. Table 1-1 compares the advantages and disadvantages of routinely used 3D cell culture techniques[50], [51], [26], [52]–[61].

In this thesis, we introduce a novel high throughput 3D cell culture technique that addresses the disadvantages of existing methods. This technique uses polymeric aqueous two-phase systems (ATPS) as media for pattering cells into spheroids. In the following sections, ATPS are defined and their key properties are explained. Due to the important role of partition of cancer cells in ATPS on spheroid formation, factors that influence this process, including the interfacial tension between two forming phases of ATPS and contact angle between cells and forming phases are discussed.

1.3. Aqueous Two-Phase Systems

Aqueous two-phase systems (ATPS) are routinely formed by dissolving two polymers, or one polymer and one salt, in an aqueous solvent. A polymeric ATPS forms when the concentration of each of the two phase-constituting polymers exceeds a minimum[62]–[64], [65]. A phase diagram specific to an ATPS describes the range of weight fractions for each polymer to result in two separate aqueous phases and gives the composition of each of the two forming phases (Figure 1-2). A binodal curve in the phase diagram separates regions of two coexisting, equilibrated phases from a single aqueous phase. A tie line connects two nodes on the binodal curve and represent the compositions of equilibrated phases. Each point on a tie line represents an initial pair of concentrations of polymers that results in forming the two phases with compositions represented with the node points, but with differing volumes (Figure 1-2)[65], [66].

1.4. Cell Partition in ATPS

The immiscibility of the two phases allows separation and purification of a variety of biomolecules through favorable partitioning to one of the forming phases. Nucleic acids and proteins, subcellular organelles and plasma membranes, and different types of cells effectively partition in ATPS[67]. Selective partitioning of biomolecules to one phase has been recently utilized in a number of novel applications such as gene and cell microarrays, cell migration, tissue engineering, and biochemical assays. Aqueous multi-phase systems have also been used for fractionation of mixtures of large particles based on differences in density of equilibrated phases[68]–[76]. The ease of making and working with immiscible aqueous solutions without special equipment makes them a highly desirable and

inexpensive technology for laboratory and industrial scale processes[74], [77]–[83]. Several factors affect the partition of biomolecules in ATPS. These include the hydrophobicity of phases, electrochemical potential of phases, pH, concentration of phase-forming polymers, molecular weights of polymers, interfacial tension between equilibrated phases, and cell size and surface properties [74], [77], [78], [84], [85]. For cell partition in ATPS, the phase chemical potential energy of cells is presented using thermodynamic models as[86]

$$\vartheta_c = \vartheta_c^o + KTln(\varepsilon_c[Cell]) + A_c\gamma_{lc} + Ze\delta_c \qquad (1\text{-}1)$$

Here, ϑ_c denotes the chemical potential of cells, ϑ_c^o presents the standard chemical potential, K denotes Boltzmann constant, T is the absolute temperature, ε_c denotes the cell activity (represents deviation from an ideal mixture), $[Cell]$ represents the number of cells partitioned to a phase, A_c and γ_{lc} denote the cell surface area and cell-aqueous phase interfacial tension, respectively, Z denotes total cell surface charges, e presents the elementary charge, and δ_c denotes the phase electrical potential[86].

Equation 1-1 is valid for both forming phases. In a state of equilibrium, cells partitioned to either of equilibrated phases generate an equal level of chemical potential energy[86]. Hence, equating the cell chemical potentials in the top and bottom forming phases, presented with equation 1-2, returns the partition coefficient of cells (μ_{eq}) as a function of difference in interfacial tensions of cell-aqueous phases and in electrical potential energies[86].

$$\ln\left(\frac{[Cell]_2}{[Cell]_1}\right) = \ln(\mu_{eq}) = \alpha(\gamma_{2c} - \gamma_{1c}) + \beta(\delta_{2c} - \delta_{1c}) + \tau_{eq} \qquad (1\text{-}2)$$

Here, τ_{eq} is a coefficient accounting for differences in standard chemical potential and cell activities in top and bottom forming phases. In addition, α and β are constants, and indices

1 and 2 represent equilibrated top and bottom phases, respectively. Therefore, the partition coefficient is a linear function of surface free energy and electrical potential. Assuming an equal electrical potential of equilibrated phases made with two nonionic polymers such as polyethylene glycol (PEG) and dextran (DEX), and using the Young equation 1-3 below, the partition coefficient is determined from equation 1-4 as a function of interfacial tension between the two equilibrated phases (γ_{12}) and the contact angle (θ) of cells and the interface of the two phases.

$$\gamma_{1c} - \gamma_{2c} = \gamma_{12} Cos\theta \quad (1\text{-}3)$$

$$\ln(\mu_{eq}) = \alpha\gamma_{12} Cos\theta + \tau_{eq} \quad (1\text{-}4)$$

1.5. Contact Angle

Contact angle is defined as the angle formed between a substrate and a tangent to the periphery of a liquid drop resting on it, at the point where the drop meets the solid surface maintained in a fluid (Figure 1-3)[87], [88]. Contact angles are widely used to study various wetting phenomena in research laboratories and several industries. Contact angles provide a quantitative measure of wettability of surfaces. A small contact angle shows affinity of the liquid to wet the surface; conversely, a large contact angle indicates that the liquid has a low tendency to spread on the substrate[88], [89]. Several techniques have been developed to measure the contact angle of sessile drop of a liquid on a surface. Goniometry, Wilhelmy plate, capillary rise, and drop shape methods are the most widely used methods. Goniometry requires a goniometer and a telescope tilted 1-2º out of the horizontal to observe the contact region of a static sessile drop on the surface. A tangent is manually aligned to the periphery of the sessile drop at the point of contact with the surface

to measure the contact angle. This method is simple but measured contact angles are subject to human error. With some training, this method can give contact angles with a best accuracy of ±2-3º[90]. In Wilhelmy plate method, a solid substrate oriented perpendicular to a liquid-vapor interface of known surface tension is immersed into or withdrawn from the liquid. The force exerted on the plate during this process is measured and used to calculate advancing and receding contact angles, corresponding to immersion and withdrawal phases, respectively[90]. The Wilhelmy plate method can be modified to measure the rise of liquid of known surface tension at a vertical plate due to the capillary effect. This approach is called capillary rise technique. The rise of liquid is then used to determine the contact angle at the solid-liquid interface through Laplace equation. Automated versions of this method can produce contact angles with an accuracy of a fraction of a degree[91]. Drop shape techniques for contact angle measurements are based on fitting a curve to the profile of a sessile drop[92]. The first derivative of an optimized mathematical fit at the contact point of the drop and the solid surface returns the contact angle. Several different types of curve fitting have been used including circle, ellipse, polynomial, and Laplacian. A major advantage of the first three curve fitting methods is the ability to estimate contact angles within ±1-2º at best, but without a need for any physical properties of the liquid[93]. On the other hand, the Laplacian curve fitting approach requires the density and an estimate of the surface tension of the liquid as inputs to determine the contact angle. This approach can reproducibly return contact angles accurate to ±0.2º[94], [95].

1.6. Interfacial Tension Measurements

Cohesive forces among liquid molecules are responsible for the phenomenon of surface tension[96]. In a bulk liquid, each molecule is surrounded with similar molecules and experiences attractive forces in all the directions that balance out each other, resulting in a net force of zero. However, a liquid molecule located at the interface with another fluid (gas or liquid) experiences a force imbalance due to the different types of molecules in the second phase[97]–[100]. This results in a net force exerted on molecules at the interface commonly referred to as surface tension or interfacial tension. Interfacial tension accounts for the shape of interfaces of drops (e.g., sessile and pendant drops)[101], [102]. Several methods have been developed for interfacial tension measurements[100]. In a spinning drop method, a drop of lighter phase is formed in the denser phase within a rotary tube. The spinning drop is imaged and its radius is measured[103]. Considering that the drop shape is due to the balance between energy generated from the rotation and the interfacial tension, one can calculate the interfacial tension through minimizing the total energy of the drop as

$$\gamma = \frac{\Delta\rho\omega^2}{4}R^3, \tag{1-5}$$

where R represents the radius of the drop (assuming the drop as a cylinder), $\Delta\rho$ denotes the density difference, ω represents the angular velocity of the tube, and γ denotes the interfacial tension[104].

Wilhelmy plate and capillary rise methods are also used to determine surface tension, using contact angle as an input, from equations 1-6 and 1-7, respectively.

$$\gamma = \frac{f}{PCos\theta V\Delta\rho g} \tag{1-6}$$

$$\gamma = \frac{\rho g h r}{2 Cos\theta} \quad (1\text{-}7)$$

Here, f is the exerted force on solid surface, P denotes the perimeter of solid surface in contact with the liquid, g is the gravitational acceleration, θ is the contact angle, V represents the displaced volume of the liquid, $\Delta\rho$ denotes the density difference, h is the height of the liquid column, and r represents the radius of the tube[105].

Approaches based on drop shape are the widely used for interfacial tension measurements[106]. In essence, the shape of a sessile or pendant drop is defined by a balance between gravitational and interfacial tension forces. When the gravitational and interfacial forces are of the same order, "well-deformed" drops can be formed and used for the interfacial tension measurements[107]. Axisymmetric drop shape analysis (ADSA) is the most widely used drop shape technique known for its high accuracy of resolving interfacial tensions[108]. This method computes the interfacial tension of liquid-fluid systems through fitting a theoretical Laplacian curve to the profile of a pendant or a sessile drop and solving the Laplace equation through numerical integration (Figure 1-4). Required inputs are the drop image and the density difference between the drop phase and the continuous surrounding phase[109]. The ADSA methodology used in this work is explained below step by step[110].

(i) The drop profile is extracted using edge detectors such as Canny or Susan. The extracted edge of the drop is considered as a series of experimental pixel points for the curve fitting process.

(ii) ADSA numerically integrates the Laplace equation to produce a theoretical Laplacian curve. Laplace Equation 1-8 represents the state of mechanical equilibrium between two fluids separated with a curved interface.

$$\gamma \left(\frac{1}{R_1}+\frac{1}{R_2}\right) = \Delta P, \quad (1\text{-}8)$$

where γ denotes the surface/interfacial tension, R_1 and R_2 represent the first and second principle radii of curvature, and ΔP denotes the pressure difference across the interface. The pressure changes linearly as a function of vertical displacement, in the absence of external forces other than gravity according to

$$\Delta P = \Delta P_0 + (\Delta\rho) g z \quad (1\text{-}9)$$

$$\Delta P_0 = \gamma \left(\frac{2}{R_0}\right) \quad (1\text{-}10)$$

Here, ΔP_0 denotes the pressure difference at the drop apex considered on a reference plane, R_0 is the radius of curvature at the apex, z is the vertical displacement from the reference plane, and $\Delta\rho$ represents the density difference between the two phases.

(iii) The radii of curvature are calculated based on the arc length (s) and inclination angle (φ) with respect to the horizontal direction (x) (Figure 1-4):

$$\frac{1}{R_1} = \frac{d\varphi}{ds} \quad (1\text{-}11)$$

$$\frac{1}{R_2} = \frac{sin\varphi}{x} \quad (1\text{-}12)$$

The inclination angle and the arc length are geometrically related through

$$cos\varphi = \frac{dx}{ds} \quad (1\text{-}13)$$

$$sin\varphi = \frac{dz}{ds} \quad (1\text{-}14)$$

Substituting equations 1-9 through 1-14 into the Laplace equation (equation 1-8) results in

$$\frac{d\varphi}{ds} = \frac{2}{R_0} + \frac{\Delta\rho g}{\gamma} z - \frac{sin\varphi}{x} \quad (1\text{-}15)$$

This equation along with equations 1-13 and 1-14 forms a set of ordinary differential equations with variables x, z, and φ as a function of the arc length, s. The boundary conditions are x(0)=z(0)= $\varphi(0) = 0$, and $\frac{d\varphi}{ds} = \frac{1}{R_0}$ at s=0.

Simultaneous numerical integration of the above set of equations is done using a variable step size Runge-Kutta method with an initial value of surface/interfacial tension and the exact value of density difference. The numerical integration stops when the vertical displacement vector, z, reaches the height of the experimental drop profile.

(iv) The positions of pixel points on the experimental profile are used to determine the normal distance between each pixel point and a point on the theoretical drop profile. Assuming (x_i, z_i) as an arbitrary point on the theoretical drop profile and (X_i, Z_i) as an arbitrary point on the experimental profile, the normal distance is calculated using equation 1-16 below

$$e_i = \frac{1}{2}[(x_i - X_i)^2 + (z_i - Z_i)^2] \quad (1\text{-}16)$$

(v) A global error function is defined as the sum of distances between experimental points and their neighboring theoretical points as

$$E = \sum_1^N e_i, \quad (1\text{-}17)$$

where N is total number of points on the experimental drop profile.

(vi) This global function is minimized using techniques such as Levenberg-Marquardt and Newton-Raphson, and steps i-vi are repeated until a predefined minimum error of $E < 10^{-7}$ is reached. Therefore, the best Laplacian fit is determined and the interfacial tension is resolved.

1.7. Aims and Scope

In this thesis, a new 3D cell culture technology based on the use of aqueous two-phase systems (ATPS) is introduced to enable reproducible formation of uniformly sized cancer cell spheroids. This high throughput technology is compatible with off-the-shelf equipment and easy to implement with minimal expertise. The resulting spheroids are individually addressable with chemical compounds and accessible for further analysis as demonstrated in this work.

Characterization of ATPS is discussed in detail in chapter II. A new theoretical approach is introduced for construction of binodal curves. Compared with a previously established titration technique for binodal curve formation, this method is faster, requires less sample, and simultaneously returns compositions of equilibrated phases. In chapter III, a polynomial fitting method is presented for contact angle measurements. This method is a modified version of existing polynomial fitting techniques but with higher accuracy to estimate contact angles within ~1° of ADSA. This approach is subsequently used to measure contact angles at the interface of live cells and a liquid-liquid interface in chapter V. The use of ADSA to measure ultralow interfacial tensions of ATPS, i.e., three to four orders of magnitude smaller than those of conventional liquid-fluid systems, is presented in chapter IV. Computational aspects of ADSA and experimental procedure of forming sessile and pendant drops are modified compared to previous versions of ADSA. Resulting data from the previous two chapters III and IV are used in chapter V, where partition of cancer cells in ATPS is studied experimentally and theoretically to determine the role of interfacial tensions of ATPS on distribution of cells between the two phases and their interface. The number of cells partitioned to top, bottom, and interface of ATPS of different

compositions is measured experimentally. A theoretical thermodynamic model is developed to elucidate the effect of interfacial tension on cell partition in ATPS. Based on this study, a particular ATPS formulation is selected for spheroid generation in chapter VI. This capability is utilized to introduce a new high throughput 3D cell culture technology. This approach is explained in detail and optimized to consistently generate uniformly sized spheroids in standard 96-well plates. To demonstrate the feasibility of using this technology for drug screening, proof-of-concept drug treatment experiments are reported with two cancer cell lines and several clinically used chemotherapy drugs in chapter VII. Finally, major conclusions of this thesis and potential future directions are discussed in chapters VIII and IX, respectively.

Table 1-1 Advantages and disadvantages of major existing 3D cell culture techniques

Technique	Advantages	Disadvantages
Liquid overlay cultures	Easy to perform, static method	Small population, substratum contact, spheroid formation highly affected by growth environment, exposes all spheroids to the same treatment condition
Spinner flask	Inexpensive, easy to handle, produces large quantities of spheroids	High shear forces applied to spheroids, lack of control on spheroid density, poor consistency of size of spheroids, exposes all spheroids to the same treatment condition
Microcarrier beads	Cultures difficult-to-grow, control over spheroid geometry, allows co-culture	Requires embedding into a spinner flask or a rotary system, exposes all spheroids to the same treatment condition
Rotary cell culture system	Minimal substrates contact, quick spheroid formation, allows co-culture, resembles microgravity, low shear stress	Expensive, difficult to handle, poor control on spheroid size and density, exposes all spheroids to the same treatment condition
Hanging droplet	High throughput, control over spheroid size and density compatible with automation platforms	Difficult to handle, difficult to change media and add drugs, subject to media evaporation during incubation
Microfluidic	Generates large number of spheroids, low shear forces	Difficult to harvest spheroids, difficult to handle during drug screening, exposes all spheroids to the same treatment condition

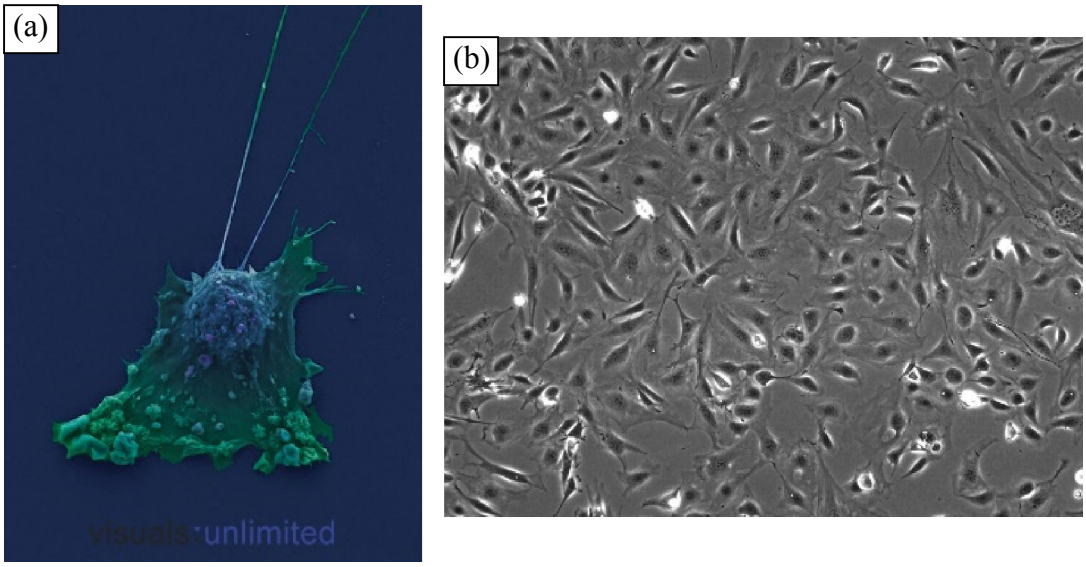

Figure 1-1 An image of a real tumor is compared with an image of cell monolayer both from breast cancer cells. (a) Electron microscopic image of a breast cancer cell tumor captured in vivo. Reprinted with permission from www.visualsunlimited.com (b) The brightfield microscopic image from a cell monolayer cultured with breast cancer cells[111]. Unlike 2D structure of the cell monolayer, cancer cells reside in a 3D environment in vivo.

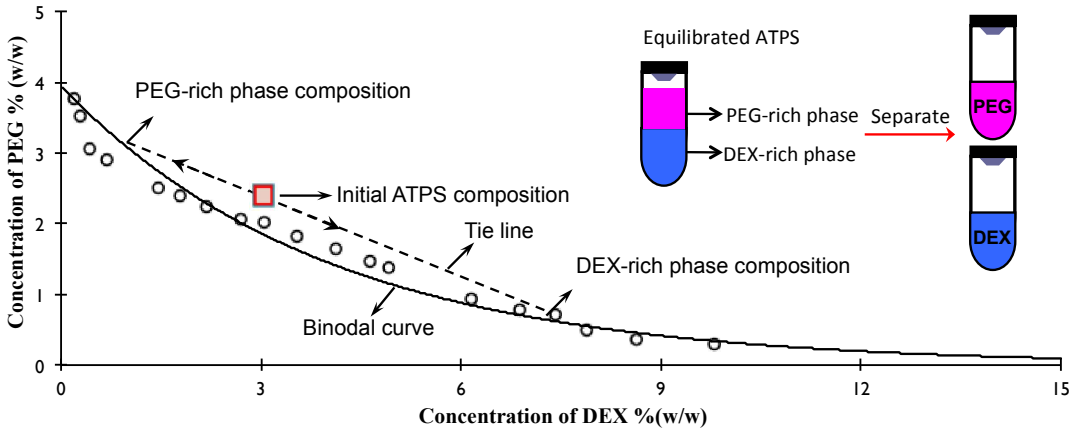

Figure 1-2 Phase diagram of an ATPS with polyethylene glycol (PEG, Mw: 35kDa) and dextran (DEX, Mw: 500kDa) as phase-forming polymers was experimentally constructed. The binodal curve (solid curve) was obtained by curve fitting to experimental data (open circles). The dashed line is only a schematic tie-line to show the locations of initial and final compositions of a two-phase solution. Only those combinations of concentrations of the two polymers above the binodal curve will result in two distinct phases. The inset schematic shows an equilibrated ATPS separated into two distinct PEG-rich and DEX-rich phases.

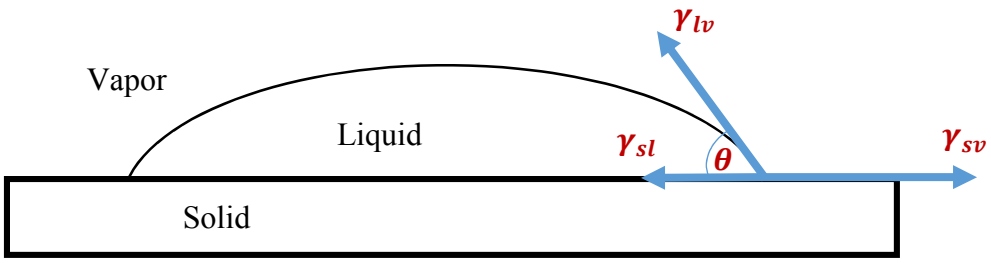

Figure 1-3 A schematic sessile drop resting on a solid surface. γ_{lv}, γ_{sv}, and γ_{sl} denote liquid-vapor, solid-vapor, and solid-liquid interfacial tensions, respectively, and θ is the contact angle. The Young equation resulting from thermodynamic equilibrium relates the interfacial tensions and contact angle, $\gamma_{lv}cos\theta = \gamma_{sv} - \gamma_{sl}$.

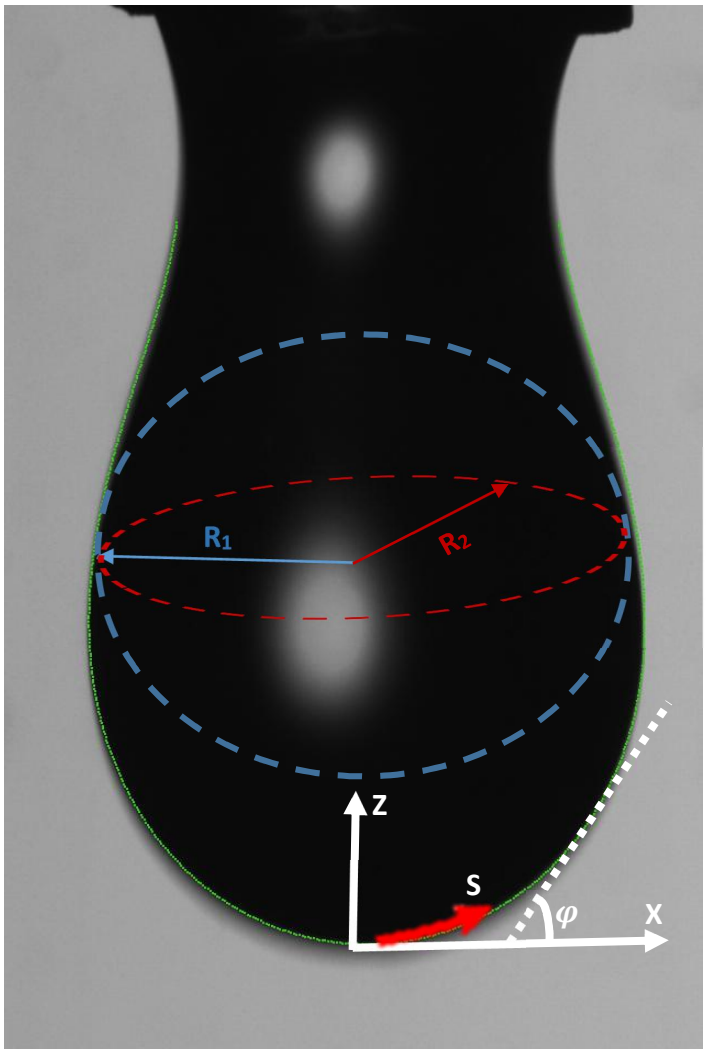

Figure 1-4 A pendant drop of 19.2% (w/v) DEX 500kDa aqueous drop in 15% (w/v) aqueous phase of PEG 35kDa is shown. A Laplacian curve fit generated with ADSA is also shown (green). Principal radii of curvature (R_1 and R_2), arc length (s) and coordinate system (Z-X) are used for explaining ADSA formulations in the text.

CHAPTER II

POLYMERIC AQUEOUS TWO-PHASE SYSTEMS

Aqueous two-phase systems (ATPS) consist of two aqueous phases made by dissolving two polymers or one polymer and one salt in an aqueous medium[65]. A polymeric ATPS forms when each of the two phase-constituting polymers exists above a certain concentration in the aqueous medium. A phase diagram is a fingerprint unique to an ATPS presenting the range of weight fractions for each polymer (Figure 2-1)[112]. A binodal curve in the phase diagram separates regions of one phase and two coexisting phases. All the solutions with polymer concentrations above the binodal curve give rise to two phase formation. A tie-line connects two points on the binodal curve, which represent compositions of the polymers in the top and bottom phases. ATPS are widely used in bioseparation processes where characterizing the phase diagram of an ATPS is critical to identify working concentrations of polymers. Binodal curve determination is the first step to characterize an ATPS. Several approaches exist to construct the binodal curve of an ATPS, theoretically and experimentally. The most common experimental method is turbidometric titration, which involves preparing a large number of two-phase solutions with varying concentrations of each of the two polymers, and gradually titrating them until the interface between the two phases disappears, resulting in a series of points that determine the binodal curve[65]. Several mathematical models based on thermodynamics of ATPS have been developed to find binodal curves[113], [114], [115]. These models are

often complex, oversimplify the working equations, and ignore effects of important parameters such as polymer molecular weight and dispersity[114].

In this chapter a theoretical method is presented to fully characterize ATPS. This method uses volume and density of a number of two-phase solutions from an ATPS along with the mass balance equation to minimize the error of estimated weight fractions of top and bottom equilibrated forming phases in each solution. This method is explained and compared with the turbidometric titration method. The theoretical approach has been explained and validated in the following sections, through constructing binodal curves of ATPS made with dextran (DEX) and polyethylene glycol (PEG) both in water and in cell culture media. To demonstrate the versatility of this approach, polyvinyl alcohol is used to form ATPS with PEG and reconstruct the binodal curve. In addition, critical points of ATPS and phase-forming polymer concentrations determined from this approach are validated against empirical data.

2.1. Materials and Methods

In this section the preparation of ATPS with PEG 35k – DEX 500k, PEG 8k – DEX 500k, and PEG 35k – DEX 40k pairs is explained. In addition, the experimental procedure of measuring the densities and volumes of stock solutions and forming phases of each ATPS is discussed

2.1.1. Preparation of Aqueous Two-Phase Systems

Polyethylene glycol (PEG) with molecular weights of 8kDa and 35kDa (Sigma-Aldrich) and dextran (DEX) with molecular weights of 40kDa and 500kDa

(Pharmacosmos) were used as phase-forming polymers to generate three sets of ATPS with PEG 35k – DEX 500k, PEG 8k – DEX 500k, and PEG 35k – DEX 40k pairs. Both PEG and DEX were in powder form and used directly to prepare stock solutions. Polymer mass for each stock solution was calculated, and the powder was weighed and carefully transferred into a conical tube containing the required volume of solvent, distilled ultrapure water or culture media (see section 2.4). To facilitate dissolution of polymers, solutions were vortexed for several minutes and kept in a 37ºC water bath for 2 hrs. Dilutions of polymer solutions were made in distilled water from stock solutions. To prepare a two-phase solution (e.g., those listed in Tables 2-1 and 2-2), 5 mL from each of PEG and DEX aqueous solutions of desired concentrations were thoroughly mixed in a conical tube and vortexed for several minutes to result in a turbid solution. After an interface formed, the solution was centrifuged for 1 hr at 5000 rpm and then kept for 24 hrs to complete the process of phase separation. In addition, polyvinyl alcohol (PVA) (Sigma-Aldrich) with a molecular weight of 23kDa was used for ATPS formation with PEG 35kDa in a validation study.

2.1.2. Density and Volume Measurements

Densities of stock solutions and both top and bottom phases of each equilibrated two-phase solution were measured using a density meter (Mettler Toledo, DA-100M), accurate to 0.001 g/cm^3. Prior to each measurement at 24 ± 1°C, the glass measuring cell of the density meter was washed three times with 20 mL of distilled water and three times with 10 mL of ethanol and dried using a built-in purge pump. The volume of the bottom phase from a two-phase solution in a graduated conical was determined by visually locating

the segregation line (interface) between equilibrated top and bottom phases with an error of 0.05 mL. The volume of the top phase was then determined by subtracting this value from the total volume of the solution.

2.1.3. An Experimental Approach to Construct Binodal Curves

A titration method was used to empirically generate binodal curves. Stock solutions of 20% (w/w) PEG and 20% (w/w) DEX of desired molecular weights were prepared in distilled water. Using these stock solutions, two-phase solutions from each of the three ATPS were made in 1.5 mL conical tubes. These solutions covered a wide range of compositions, from 0.56% (w/w) PEG and 19% (w/w) DEX to 16% (w/w) PEG and 0.94% (w/w) DEX. The weight of each conical tube with a two-phase solution was recorded. Each solution was titrated drop-wise with distilled water until a one-phase system formed. The conical tube was centrifuged at 5000 rpm for 3 min to ensure that a one-phase system had formed. The final weight of the conical with the one-phase system was recorded and used to calculate the weight of diluent added just prior to one-phase formation. The final composition of each system was included in a plot of weight fractions of phase-forming polymers to generate an experimental binodal curve.

2.1.4. Statistical Analysis

Statistical analysis is performed using Matlab. Results are presented as mean ± standard deviation. Differences between means are determined using one-way ANOVA. P-value smaller than 0.05 is considered as statistically significantly different.

2.2. Results and Discussion

In what follows, a theoretical approach to generate binodal curves is presented in detail. An established experimental approach to form binodal curves is explained. Finally, binodal curves generated using our new approach are compared to and validated against those determined experimentally for the three ATPS studied.

2.2.1. A Theoretical Approach to Construct Binodal Curves

To form the phase diagram of an aqueous two-phase system (ATPS) with a specific pair of phase-forming polymers, we used density and volume of equilibrated phases from a series of two-phase solutions and computationally optimized a general binodal equation. In this study, we used ATPS with three pairs of polymers, i.e., PEG 35k – DEX 500k, PEG 8k – DEX 500k, and PEG 35k – DEX 40k. With each pair, we prepared ten two-phase solutions using varying concentrations of polymers from respective stock solutions and measured the density and volume of resulting equilibrated (segregated) phases. Table 2-2 lists the resulting data for the PEG 35k – DEX 500k ATPS as an example. Data for the other two ATPS are included in Appendix A.

Equation 2-1 below relates weight fractions, in w/w, of PEG and DEX for any point on a binodal curve[83].

$$[PEG] = C_1 e^{(C_2[DEX]^{0.5} + C_3[DEX]^3)} \qquad (2\text{-}1)$$

This equation contains three coefficients (C_1, C_2, and C_3) that are specific for an ATPS with a specific pair of phase-forming polymers, such as the PEG 35k – DEX 500k ATPS. To determine these coefficients and hence the binodal curve, we implemented a computational scheme consisting of six main steps, as outlined below.

1- Initial values of the three coefficients (C_1, C_2, and C_3) are estimated from the literature for an ATPS of known binodal equation.

2- For each equilibrated phase (top and bottom) from a two-phase solution, there is a unique isopycnic line that relates the weight fractions of PEG and DEX in that phase through equation 2-2 below. There are two isopycnic lines for each two-phase solution (see Figure 2-1). Therefore, the following equation is written for both top (T) and bottom (B) phases. Each line intersects with a point on the binodal curve that represents the composition of the respective phase[116].

$$[PEG] = \frac{v_s - \rho^{-1}}{v_s - v_p} - \frac{v_s - v_d}{v_s - v_p}[DEX] \qquad (2\text{-}2)$$

Here v_s, v_p, and v_d denote specific volumes of water (solvent), PEG, and DEX, respectively, and ρ is the phase density. We consistently measure the specific volume of water as v_s=1.003±0.001 mL/g. However, specific volumes of PEG (v_p) and DEX (v_d) depend on physical properties of the polymers such as their molecular weights. Following is a simple method to estimate these values and use them as known quantities in equation 2-2.

The specific volume of each polymeric aqueous solution is due to its constituents as

$$\frac{1}{\rho} = (1 - [DEX] - [PEG])v_s + [DEX]v_d + [PEG]v_p \qquad (2\text{-}3)$$

Writing equation 2-3 for stock solutions of PEG and DEX gives

$$\frac{1}{\rho_{PEG}} = v_s - (v_s - v_p)[PEG] \qquad (2\text{-}4)$$

$$\frac{1}{\rho_{DEX}} = v_s - (v_s - v_d)[DEX] \qquad (2\text{-}5)$$

The density of each stock solution (ρ_{PEG} and ρ_{DEX}) is measured using a density meter. The weight fraction of each polymer in its respective stock solution is also a known

quantity. We prepared nine stock solutions of different concentrations from each polymer and plotted the specific volume of each stock solution ($\frac{1}{\rho_{PEG}}$ and $\frac{1}{\rho_{DEX}}$) versus polymer weight fraction (Figure 2-2). The slope of fitted line relates the specific volume of stock solutions and polymer weight fraction through equations 2-4 and 2-5. Therefore, the slope of each line is used to calculate the specific volume of PEG and DEX polymers as v_p=0.8321 mL/g and v_d=0.6374 mL/g, respectively (see caption of Figure 2-2). These values are then inserted into equation (2-2).

3- Next, weight fractions of PEG and DEX in top and bottom phases of an equilibrated two-phase solution are approximated.

3.1- Equations 2-1 and 2-2 are intersected to determine the weight fraction of PEG and DEX in the bottom, DEX-rich phase.

3.2- A tie-line equation is constructed using the bottom phase composition (e.g., point B in Figure 2-1) and the stock solution composition (e.g., I1 in Figure 2-1).

3.3- The tie-line equation and the equation of the isopycnic line of the top phase (equation 2-2) are intersected to determine the composition of PEG and DEX in the top, PEG-rich phase.

At this step, $[PEG]_T$, $[DEX]_T$, $[PEG]_B$, and $[DEX]_B$ will have approximate quantities because the coefficients of the binodal are only estimated values from step 1. This process is repeated for top and bottom phases of all two-phase solutions (e.g., those in Table 2-1).

4- We invoke the conservation of mass principle and form two independent equations for conservation of mass of PEG and DEX. The total mass of each polymer used to prepare

its stock solution is equal to the sum of mass of the polymer in top and bottom phases of an equilibrated two-phase solution.

$$M_{PEG}^{Total} = \rho_T V_T [PEG]_T + \rho_B V_B [PEG]_B \quad (2\text{-}6)$$

$$M_{DEX}^{Total} = \rho_T V_T [DEX]_T + \rho_B V_B [DEX]_B \quad (2\text{-}7)$$

Here, M_{PEG}^{Total} denotes the total mass of PEG, M_{DEX}^{Total} represents the total mass of DEX, and ρ and V are experimentally measured density and volume of each equilibrated phase, respectively.

From experimental measurements, exact quantities of M_{PEG}^{Total}, M_{DEX}^{Total}, ρ_T, V_T, ρ_B, and V_B are known. However, polymer weight fractions in equations 2-6 and 2-7 are only estimated quantities from steps 1 through 3 above. The difference between exact and estimated values of mass for each polymer is computed as an error:

$$\varepsilon_1 = (M_{PEG}^{Total}) - (\rho_T V_T [PEG]_T + \rho_B V_B [PEG]_B) \quad (2\text{-}8)$$

$$\varepsilon_2 = (M_{DEX}^{Total}) - (\rho_T V_T [DEX]_T + \rho_B V_B [DEX]_B) \quad (2\text{-}9)$$

ε_1 and ε_2 represent errors from mass balance for top and bottom phases of one equilibrated two-phase solution only. We define a total error (E) considering ε_1 and ε_2 values for all equilibrated two-phase solutions from an ATPS (e.g., all the solutions in Tables 2-1 and 2-2).

$$E = \sqrt{\left(\sum_{i=1}^{n} \varepsilon_{1,i}\right)^2 + \left(\sum_{i=1}^{n} w\varepsilon_{2,i}\right)^2} \quad (2\text{-}10)$$

$\varepsilon_{1,i}$ and $\varepsilon_{2,i}$ denote the errors calculated from equations 2-8 and 2-9 for the i^{th} equilibrated two-phase solution, n is the total number of solutions for an ATPS (e.g., n=10 in Table 2-1), and w is a weight factor. For the systems studied here, w=2 (see Appendix A).

5- Using a standard optimization technique in MATLAB (MathWorks) called Pattern Search, a new set of C_1, C_2, and C_3 is found that results in a value for E smaller than that calculated in step 4. These new coefficients are then used in equation 2-1, the above steps are repeated, and a new E value is generated again.

6- This process is repeated until the difference in E from two consecutive iterations becomes smaller than a pre-defined value of 10^{-7}, i.e., the total error is minimized. At this point, corresponding C_1, C_2, and C_3 values are optimum and equation 2-1 is resolved.

At the end of this process, the binodal curve is fully determined simply using measured volume and density of equilibrated phases for a number of two-phase solutions from an ATPS with specific phase-forming polymers. We implemented this strategy and constructed binodal curves for ATPS made with three different polymer pairs, PEG 8k – DEX 500k, PEG 35k – DEX 500k, and PEG 35k – DEX 40k. Figure 2-3 shows each binodal curve (solid lines) and compares it with empirical points obtained from turbidometric titration experiments. For all three ATPS, there is an excellent agreement between the results with empirical data. It is noted that the asymmetry of binodal curves for the PEG 8k – DEX 500k and PEG 35k – DEX 500k is due to large differences in the molecular weights of phase-forming polymers. Using polymers with fairly similar molecular weights (PEG 35k and DEX 40k) increases the symmetry of the binodal.

2.3. Validation Studies

In addition to comparing with the titration technique above (Figure 2-3), we used the following analyses to further examine the validity of our approach to determine binodal curves of ATPS.

2.3.1. Composition of Equilibrated Phases

A major advantage of this new approach for constructing binodals over other techniques such as titration is that it readily provides weight fractions of polymers in top and bottom phases of an equilibrated two-phase solution, i.e., $[PEG]_T$, $[DEX]_T$, $[PEG]_B$, and $[DEX]_B$. Table 2-3 shows weight fractions of PEG and DEX in top and bottom phases of the same two-phase solutions listed in Table 2-1. These quantities were generated at the end of the 6-step optimization process above. We performed fluorescent imaging of separated aqueous phases of a two-phase solution containing fluorescently conjugated polymers as an independent validation approach. The distribution of the FITC-conjugated polymer between the two phases could provide a measure of weight fraction of the particular polymer in equilibrated phases.

We selected the 5% (w/v) PEG 35k – 6.4% (w/v) DEX 500k system (system 1 from Table 2-1) and added 0.1% (v/v) of either FITC-PEG 35k or FITC-DEX 500k, both prepared in distilled water and at a similar concentration. The distribution of the FITC-conjugated polymer between the two phases provides a measure of weight fraction of that polymer in equilibrated phases. After phase separation for 24 hrs, 10 µL samples from top (PEG-rich) and bottom (DEX-rich) phases were separately placed between two coverslips and fluorescent images were captured under identical conditions. Figure 2-4 shows the

results and representative fluorescent images of samples. In the two-phase solution containing FITC-DEX (Figure 2-4a), the fluorescent intensity ratio of DEX-rich to PEG-rich phases is 79.3±7. This is in close agreement with the ratio of weight fraction of DEX in bottom and top phases, i.e., 81.3 (system 1 from Table 2-3). Similarly in the two-phase solution containing FITC-PEG (Figure 2-4b), the fluorescent intensity ratio of PEG-rich to DEX-rich phases is 3.9±0.8, in reasonable agreement with the ratio of weight fraction of PEG in top and bottom phases, i.e., 5.4 (system 1 from Table 2-3). Although this experiment was only done for one of the two-phase solutions of Table 2-1, the result validates the compositions of equilibrated phases generated during constructing the binodal curve from our new approach.

2.3.2. Determination of Critical Point

We identified the critical point of the PEG 35k – DEX 40k ATPS using composition of equilibrated phases, and compared it with results from an established approach. For a two-phase solution from an ATPS, there is a unique tie-line that connects compositions of equilibrated top and bottom phases on the binodal curve (see Figure 2-1). Tie-lines of an ATPS become shorter as the weight fractions of polymers reduce, and ultimately approach a point on the binodal curve. This point is called the critical point at which the compositions and volumes of the two phases become identical and the differences between them vanish. On each tie-line, there is a pair of weight fractions of phase-forming polymers (e.g., point I_1 in Figure 2-1) that results in equal volumes of equilibrated top and bottom phases. The ratio of distances between this point and those representing compositions of bottom (B)

and top (T) phases at two ends of a tie-line is proportional to the ratio of total mass of top and bottom phases:

$$\frac{\overline{I_1B}}{\overline{I_1T}} = \frac{\rho_T V_T}{\rho_B V_B} \quad (2\text{-}11)$$

Here, V and ρ denote volume and density of equilibrated phases, respectively. With $\frac{V_T}{V_B} = 1$, the point I_1 is located on the tie-line using measured densities of equilibrated phases from $\frac{\overline{I_1B}}{\overline{I_1T}} = \frac{\rho_T}{\rho_B}$.

We used this principle to determine the critical point of the PEG 35k – DEX 40k ATPS. We first determined the tie-lines for ten two-phase solutions with known compositions of equilibrated phases. On each tie-line, a composition that gave two equilibrated phases with an equal volume was identified (open triangles in Figure 2-5a). Next, a curve was fitted to these points and extrapolated to intersect with the binodal curve (solid triangle). This intersection returned a critical point composition of 2.0% (w/w) PEG and 6.2% (w/w) DEX for the PEG 35k – DEX 40k ATPS.

We compared this method with a previously-established experimental technique. Ten two-phase solutions of different compositions were made with the PEG 35k – DEX 40k ATPS, volumes of top and bottom phases were measured, and the ratios were plotted against polymer weight fraction ratios $[PEG]/[DEX]$ (Figure 2-5b). This experiment showed that the volume ratio of $\frac{V_T}{V_B} = 1$ corresponds to a polymer weight fraction ratio of $[PEG]/[DEX] = 0.375$ (Figure 2-5b inset). Then, six two-phase solutions with this weight fraction ratio and compositions close to the binodal curve were formed. Densities of top and bottom phases were measured and plotted versus the total polymer weight fraction (Figure 2-5c). The total polymer weight fraction that returned the same density for top and

bottom phases was extrapolated from this figure as 8.2% (w/w). With a known weight fraction ratio of 0.375, this gave a critical point composition of 2.2% (w/w) PEG and 6.0% (w/w) DEX. This point is shown with a solid square in Figure 2-5a. Close agreement between compositions of the critical point from this established technique and our approach verifies the validity of our strategy to determine binodals and phase compositions of ATPS.

2.4. Versatility of the Method

Finally, we demonstrated that this method allows constructing binodals of ATPS made with a solvent other than water and with polymer pairs other than PEG and DEX. First, we used a cell culture medium, Dulbecco's Modified Eagle Medium (DMEM), to dissolve PEG 35k and DEX 40k and formed two-phase solutions in a wide range of polymer concentrations. The binodal of this ATPS was generated using the approach outlined above as shown by the dashed line in Figure 2-3c. The result suggests that presence of salts and other additives in the culture medium shifts the binodal slightly, but significantly, and allows phase separation at lower polymer concentrations. Next, we used PEG 35k and PVA 23k as phase-forming polymers, prepared two-phase solutions with various concentrations of the polymers in water, and constructed the binodal curve of the ATPS. Figure 2-6 shows that the binodal resulting from the new approach is in good agreement with that generated from titration experiments with this ATPS. Therefore, our approach is broadly applicable to ATPS made with different polymers and solvents.

2.5. Summary

We describe a straightforward approach to determine binodal curves of polymeric aqueous two-phase systems (ATPS). This method only requires experimentally measured values of mass of polymers and volumes and densities of equilibrated phases of several two-phase solutions from an ATPS. Using a general form of the binodal curve equation with unknown coefficients, equations of isopycnic lines representing equilibrated aqueous phases, and mass balance of phase-forming polymers, an iterative computational approach is implemented to determine the binodal curve. This method simultaneously resolves compositions of equilibrated phases of two-phase solutions used to construct the binodal. The availability of phase compositions enables complete characterization of the phase diagram of each polymeric ATPS through determination of tie-lines and the critical point, in agreement with established techniques. This approach will broadly benefit studies involving separation and fractionation of biomolecules and particles using immiscible aqueous solutions prepared with various polymers, surfactants, and salts.

Table 2-1 Concentrations of PEG and DEX in stock solutions and density of stock solutions made with the PEG 35k – DEX 500k ATPS.

Two-phase solution	Concentration of stock solutions		Density of stock solutions	
	DEX solution %(w/v)	PEG solution %(w/v)	DEX solution (g/mL)	PEG solution (g/mL)
1	6.4	5.0	1.021	1.005
2	8.0	3.6	1.026	1.003
3	8.0	4.0	1.026	1.004
4	8.4	3.8	1.028	1.003
5	8.8	4.0	1.030	1.004
6	9.2	4.2	1.031	1.004
7	12.0	5.4	1.042	1.006
8	12.8	10.0	1.046	1.014
9	16.0	5.0	1.059	1.005
10	16.0	10.0	1.059	1.014

Table 2-2 Volume and density of equilibrated phases of two-phase solutions made with the PEG 35k – DEX 500k ATPS. Each solution was made using 5 mL of its constituting aqueous phases (i.e., the total volume is 10 mL).

Two-phase solution	Volume of equilibrated phases		Density of equilibrated phases	
	Bottom phase (mL)	Top phase (mL)	Bottom phase (mL)	Top phase (mL)
1	3.1	6.9	3.1	6.9
2	4.5	5.5	4.5	5.5
3	4.4	5.6	4.4	5.6
4	4.7	5.3	4.7	5.3
5	4.7	5.3	4.7	5.3
6	4.6	5.4	4.6	5.4
7	5.0	5.0	5.0	5.0
8	3.6	6.4	3.6	6.4
9	5.8	4.2	5.8	4.2
10	4.3	5.7	4.3	5.7

Table 2-3 Compositions of equilibrated top (PEG-rich) and bottom (DEX-rich) phases of the PEG 35k –DEX 500k ATPS calculated through construction of binodal curve.

Two-phase solution	Composition of equilibrated phases, %(w/w)			
	Top phase		Bottom phase	
	DEX	PEG	DEX	PEG
1	0.09	3.90	7.22	0.72
2	0.85	2.97	6.32	0.96
3	0.20	3.66	6.62	0.88
4	0.29	3.51	6.92	0.80
5	0.12	3.81	7.81	0.58
6	0.03	4.11	8.39	0.46
7	0.00	5.42	11.91	0.05
8	0.00	8.15	16.67	0.00
9	0.00	6.03	13.70	0.01
10	0.00	8.90	18.38	0.00

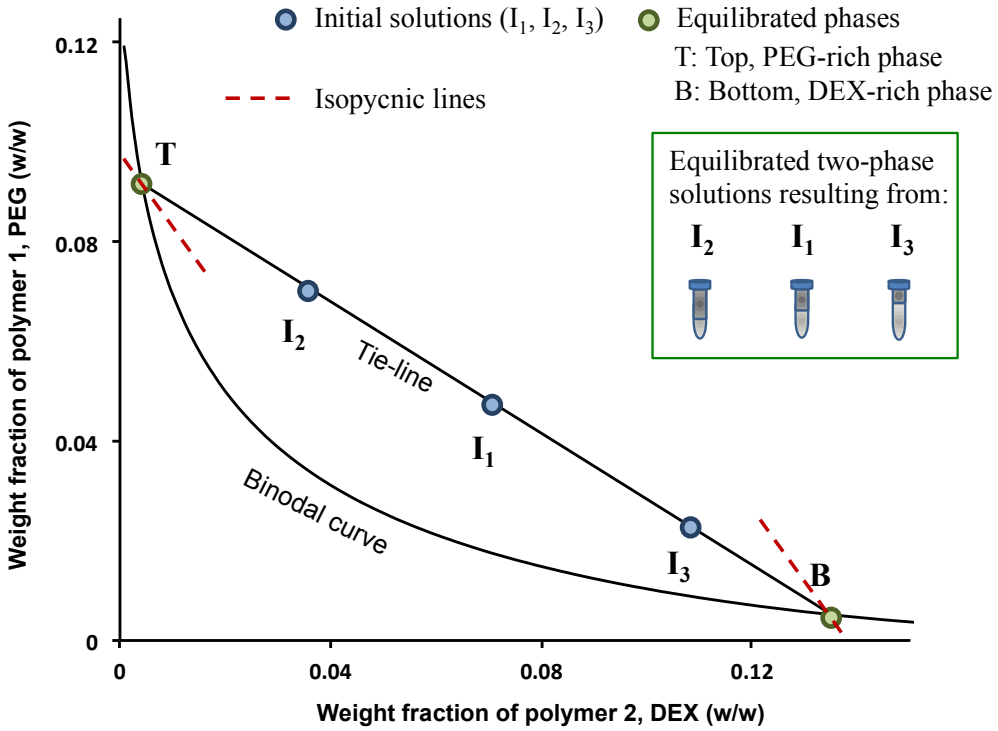

Figure 2-1 Phase diagram of an ATPS is shown schematically. Any composition of concentrations of two phase-forming polymers, such as polyethylene glycol (PEG) and dextran (DEX), above the binodal curve results in two separate phases. Point I1 represents an initial aqueous solution with defined weight fractions of the two polymers. A tie-line connects the points representing the compositions of equilibrated top phase (T), bottom phase (B), and the initial point (I1). Any pair of weight fractions of the two polymers on the same tie-line (e.g., I1, I2, and I3) results in equilibrated top and bottom phases of similar compositions but with different volume ratios (see the schematic within the box). A unique isopycnic line (dashed) relates the weight fraction of polymers in each equilibrated phase (T and B) to specific volumes of polymers and the phase density.

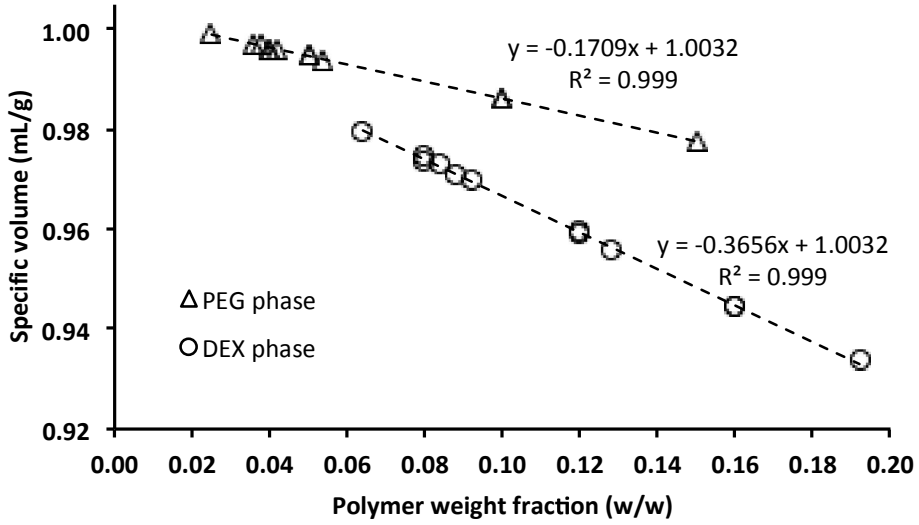

Figure 2-2 Specific volume versus polymer weight fraction for nine stock solutions of PEG 35k and DEX 500k is shown. The slopes of fitted lines are used to estimate specific volumes of PEG and DEX polymers using equations 2-4 and 2-5, i.e., v_s-v_p = 0.3656 and v_s-v_d = 0.1709. In equations of fitted lines, y denotes specific volume and x is polymer weight fraction.

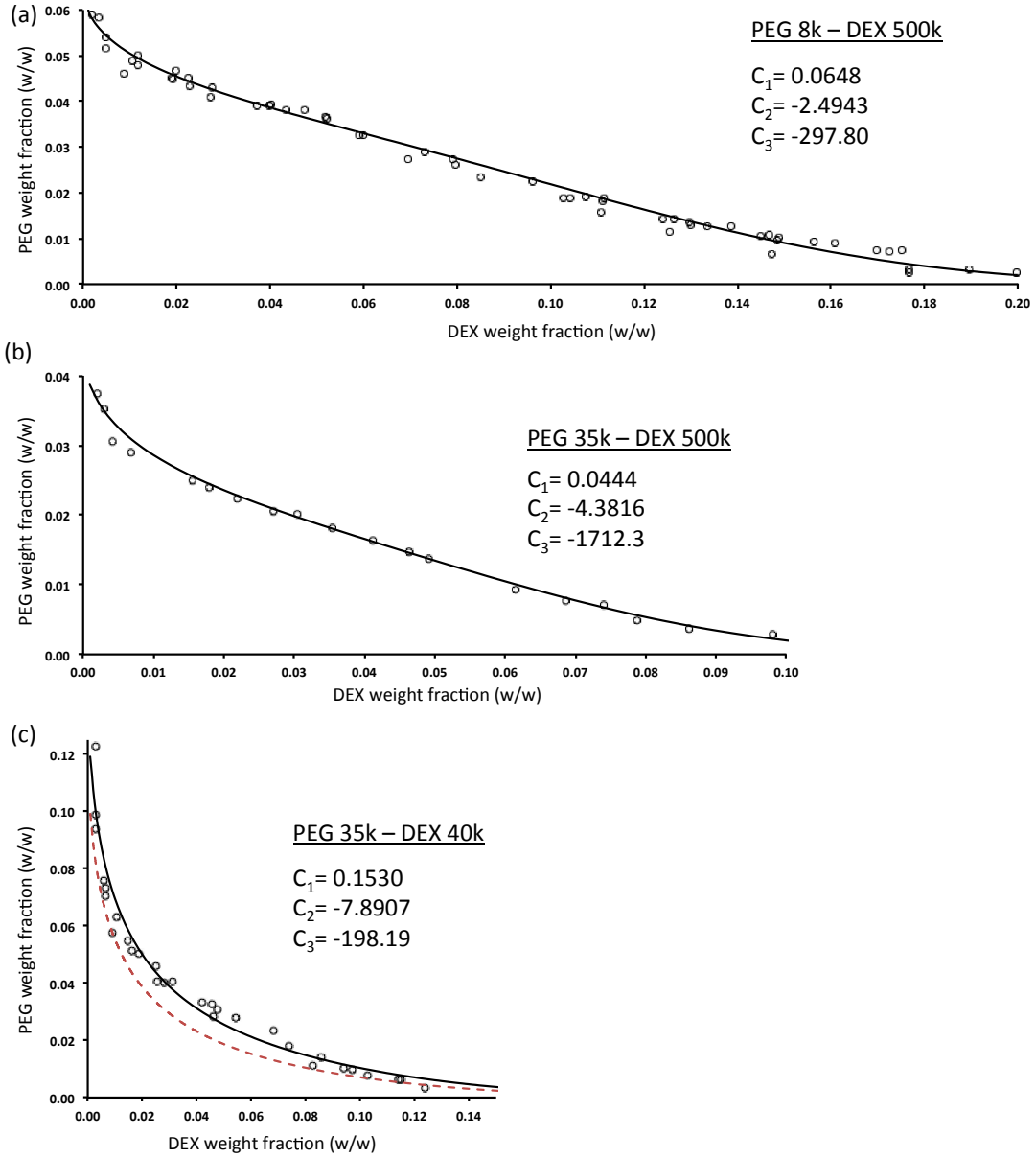

Figure 2-3 Binodal curves are shown for three ATPS made with phase-forming polymers (a) PEG 8k – DEX 500k, (b) PEG 35k – DEX 500k, and (c) PEG 35k – DEX 40k using water as solvent (solid lines). Coefficients C_1, C_2, and C_3 of the binodal equation for each ATPS are given. Experimental points determined using the titration technique (open circles) are included for comparison. The dashed line in panel (c) represents the binodal curve of PEG 35k – DEX 40k made using cell culture media as solvent.

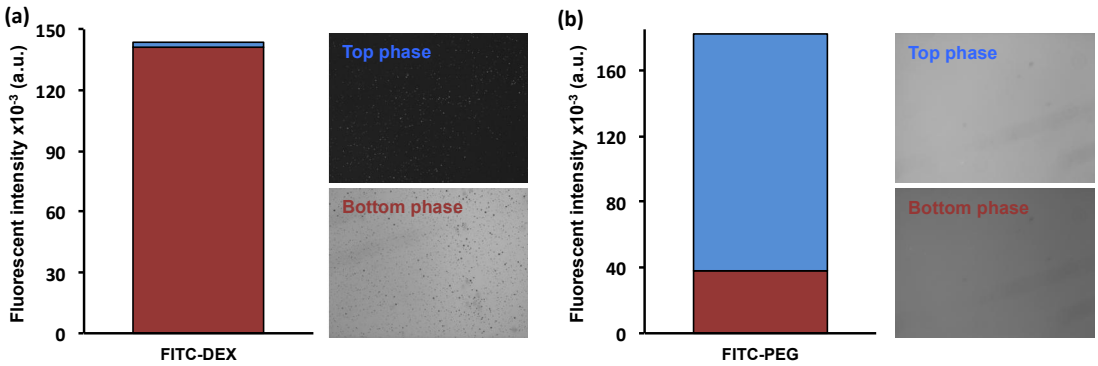

Figure 2-4 (a) Fluorescent intensity of samples from top (blue) and bottom (red) phases of a two-phase solution containing FITC-DEX. (b) Fluorescent intensity of samples from top (blue) and bottom (red) phases of a two-phase solution containing FITC-PEG. The two-phase solution was made using 5% (w/v) PEG 35k and 6.4% (w/v) DEX 500k.

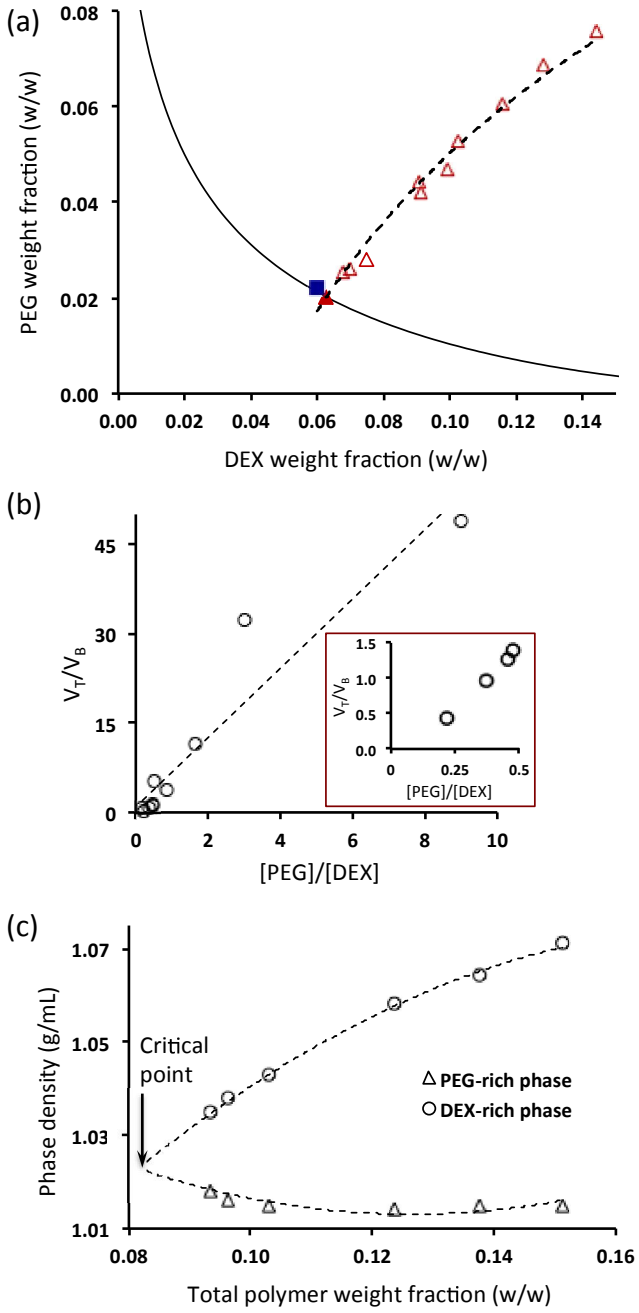

Figure 2-5 (a) Critical point (solid triangle) resulting from intersecting the fit ([PEG] = 0.07ln([DEX]) + 0.20, R^2=0.98) to points of equal volume of top and bottom phases on tie-lines lies very close to that obtained from a previous experimental method (solid square). (b) Volumes of equilibrated top and bottom phases become approximately equal at a ratio 0.375 of weight fractions of polymers. The inset represents data points close to $\frac{V_T}{V_B} = 1$. (c) Equilibrated top and bottom phases approach an identical density at the critical point.

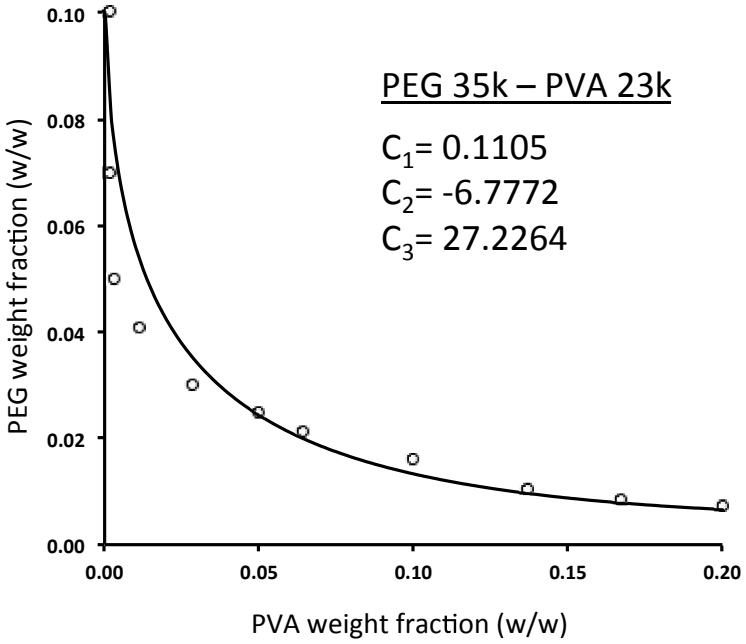

Figure 2-6 Binodal curve of an ATPS made with phase-forming polymers PEG 35k and PVA 23k and water as solvent. Open circles represent data points from titration experiments for comparison.

CHAPTER III

A POLYNOMIAL FITTING METHOD TO MEASURE CONTACT ANGLES

Wettability of solid surfaces is important for a wide range of industrial and biological applications[117], [118]. A common method to characterize surface wettability is contact angle measurement using a sessile drop of a probe liquid on the surface. Contact angle is defined as the angle between a tangent to the three-phase line, which forms at the air-liquid-solid interface, and the solid surface (Figure 3-1). Several methods have been developed to resolve contact angles from sessile drop profiles. Among all, a certain drop shape technique called axisymmetric drop shape analysis-profile (ADSA-P) often resolves contact angles with an accuracy of ±0.2°, using Laplacian curve fitting to the drop profile through numerical integration of Laplace equation to identify a "best" fit[119]. ADSA-P requires at least the liquid density to explicitly determine surface tension of the liquid by fitting a unique Laplacian curve to the drop profile. The contact angle is then computed as the slope of the fitted Laplacian profile at the three-phase contact point[120], [121]. This approach is considered the most accurate methodology for contact angle measurements.

The accuracy of ADSA-P inherently depends on the axisymmetry of drops and identification of the contact point of the drop with the solid. In many cases such as when a surface is rough, drops will deviate from an axisymmetric shape. In addition, many surfaces are not transparent making it difficult to locate the contact point. Biological surfaces such as a monolayer of cells are an example that present difficulties for contact angle

measurements with ADSA-P. An alternative method, theoretical image fitting analysis (TIFA), was developed to eliminate the need for an independent edge detector required with ADSA: A theoretical, black and white gradient image containing a Laplacian profile is constructed and fit to the experimental gradient image. The error between the theoretical and experimental gradient images is minimized to give the best fit, from which contact angle is obtained with a comparable accuracy to ADSA-P[122]. Although direct measuring of contact angles does not require a priori knowledge of physical properties of the probe liquid, drop shape techniques are based on Laplace equation that requires at least the liquid density to explicitly determine surface tension of the liquid by fitting a unique Laplacian curve to the drop profile[93], [92]. To avoid conducting laborious experiments of measuring densities of solutions and enabling contact angle measurements on rough and translucent surfaces, image processing-based polynomial fitting techniques have been developed to eliminate the need for physical properties of solutions. Polynomial fitting approaches extract the profile of a sessile drop similar to ADSA-P. Then, a polynomial is fitted to the profile of the sessile drop, and contact angle is calculated as the slope of the polynomial at three-phase contact point.

In this study, a modified polynomial fitting is presented to enable generating reproducible and accurate results for drops with a wide range of contact angles[123]. We will demonstrate the application of this method in Chapter V to measure contact angles of sessile drops made using an aqueous two-phase system on a monolayer of cells, i.e., a rough and translucent surface.

3.1. Materials and Methods

In this section preparation of surfaces for contact angle measurements is explained. In addition, the procedure of capturing sessile drop images is presented.

3.1.1. Surface Preparation and Test Liquids

A 6% solution of Teflon AF 1600 was diluted in FC-75 (Dupont Co.) at a 1:1 (v/v). EGC1700 (3M Co.) was used as received. Silicon wafers <100> (Silicon Sense) were cut into 1 cm^2 pieces and a 1 mm diameter hole was drilled at the center of each sample. To remove inorganic contaminants, the drilled surfaces were cleaned by sonication in alcohol for 30 min and then in distilled water for 15 min. The resulting surfaces were soaked in chromic acid for at least 24 h, rinsed with distilled water, and dried under a heat lamp. Polymer films were prepared using a dip-coating technique. Teflon AF 1600 films were annealed at 165ºC (above its glass transition temperature, Tg=160°C) overnight. The EGC-1700 films were not annealed because of the low Tg of 30°C. This surface preparation method gives very smooth films with a mean roughness of ~0.4 nm. As test liquids, we used decane, decamethylcyclopentasiloxane (DMCPS), hexadecane, methyl salicylate, dibenzylamine, and distilled water. All the liquids except water were purchased from Sigma-Aldrich Co. at the highest purity available. Sessile drop experiments were performed at a low rate of motion of the three-phase line (~0.5 mm/min).

3.1.2. Imaging

Sessile drops were imaged using a lens on a digital-camera system adjustable to various magnifications of 0.6x to 4.8x. The image resolution, i.e. image width × height in

pixel values, was adjusted by the camera (JAI) software. Our program converted the images to .tiff format before analyzing them. Images were stored as 8-bit grayscale pixels with 256 shades of gray (0:black to 255:white) to represent pixel intensity. The combination of resolution and magnification was adjusted to accommodate all drop sizes during dynamic contact angle experiments. This resulted in a pixel size of 1.330 μm in captured images.

3.1.3. Statistical Analysis

Statistical analysis is performed using Matlab. Results are presented as mean ± standard deviation. Differences between means are determined using one-way ANOVA. P-value smaller than 0.05 is considered as statistically significantly different.

3.2. Results and Discussion

In this section, the procedure of contact angle measurement is explained. This includes edge detection, contact point detection, and polynomial fitting. Then the reported contact angles are compared with those obtained from ADSA-P to validate our new approach.

3.2.1. Edge Detection

We first applied the median and average filters to raw images (.tiff format) of drops to smoothen them and remove noise (Figure 3-2a). Then, we selected the Canny edge operator to find the drop profile from each image (Figure 3-2b). Canny is robust and less sensitive to lighting conditions compared to other edge operators. By default, Canny

assumes two thresholds of T_1 and T_2 ($T_1>T_2$). T_1 determines the threshold to start edge selection and T_2 helps smoothen detected edges. We started with $T_1=0.3$ and $T_2=T_1/2$ to detect the drop profile. If a complete profile was not returned, new values of $T_{1new}=T_{1old}+0.1$ and $T_2=T_1/2$ were automatically set to repeat the process.

We often found that the detected edge is discontinuous around the contact point of the drop with the solid. In addition to the main drop profile, small, connected particles were also present in the processed image (Figure 3-2b). To resolve these issues, connected edges were considered in several groups. The number of pixels in each group was counted as the group population. Starting with the largest populated group, the arc of a circle was fitted to the pixels. Then, curvature was calculated as the inverse of the fitted arc radius. Extremely small curvatures, mostly less than 0.0001 of a pixel, represented a group of undesired edges. Therefore if the curvature was close to zero, the group of pixels was considered as noise and the procedure was repeated for the next populated group until all noises were rejected (Figure 3-2c). To generate connected edges around contact points, Unsharp mask and average filter were used to enhance and further smoothen images (Figure 3-2d). It is noted that detected contact points on both sides in Figure 3-2b are displaced. This is resolved below in sections 3.2.2 and 3.2.3 to precisely identify left and right contact points.

3.2.2. Refinement of Drop Profiles to a Sub-Pixel Resolution

Similar to most edge detectors, Canny uses the first or the second derivative functions to find the maximum variation in the intensity as the edge location. Figure 3-3a shows an experimental sessile drop image that specifies three intensity regions: a bright region (B), a transition region of several pixels wide (T), and a dark region (D). Figure 3-

3b shows pixel intensity values and changes in the intensity in these regions in the direction perpendicular to the drop profile.

The maximum intensity change happens in the transition region T where the drop edge, as determined by Canny, resides. Call this the C-edge. Nevertheless, due to optical effects, it is plausible to expect that the actual physical edge resides within the region D and in the vicinity of region T along the perpendicular line to the drop profile. We examined this question experimentally using a glass ball bearing of known and precise diameter 1562.530 ± 0.254 μm (McMaster-Carr Inc.). We imaged the ball bearing under a similar magnification and lighting condition used to acquire sessile drop images. Then, we used the Canny operator to find the C-edge of the ball bearing and determine its radius in pixel units (Figure 3-4a). We also imaged a calibration grid (Pyser-SGI Ltd.) to find the scale of pixel-to-millimeter ratio of the ball bearing image. The difference between the C-edge result and the ball bearing diameter reported by the manufacturer was calculated. The detected profile (C-edge vs. physical edge) was displaced by the calculated number of pixels (Figure 3-4b). We note that based on the camera resolution and imaging magnification, the size of each pixel is 1.330 μm. This is 5.24 times larger than manufacturer-reported tolerance of 0.254 μm for the ball bearing diameter, confirming that the calculated difference is real and not an artifact of the imaging system. Figure 3-4c shows the intensity changes in the direction perpendicular to the periphery of ball bearing from outside to inside, including the location of C-edge and that of exact ball bearing edge. Therefore, the C-edge is displaced inward to match the actual diameter of the ball bearing.

To generalize this new method of locating physical edges in drop-images captured under different experimental conditions, we imaged the ball bearing with different lighting

conditions and then calculated the grayscale ratio at the Canny edge (G_c) to the minimum grayscale of the image (G_m). Knowing the ball bearing diameter, we found the exact edge location (using calibration grid in Figure 3-5) and its intensity G_e. Plotting $r_e = \frac{G_e}{G_m}$ versus $r_c = \frac{G_c}{G_m}$ resulted in a linear correlation (Figure 3-6):

$$r_e = 0.19 \times r_c + 0.58 \quad (3\text{-}1)$$

Regression analysis returned a *p*-value of smaller than 0.001 (i.e., statistically significant). For a given image of a sessile drop with known G_c and G_m, equation 3-1 can be used to calculate r_e from a known r_c. Thus, the grayscale of the exact edge is calculated and the detected edge is moved toward the calculated G_e in the direction of perpendicular to the drop profile.

3.2.3. Contact Points of Drops with the Solid Surface

We developed a new method to identify the coordinates of contact points of the drop with the solid, using the symmetry of profiles of the drop and its reflection on the surface. The drop and reflection profiles were extracted around each contact point and smoothened using average and median filters. Figure 3-7a shows the original drop profile that contains vertically aligned pixels (i.e., with the same X-coordinate). The edge detection process often results in two or more vertically aligned pixels in the contact region. We substituted these pixels with the average Y-coordinate at each X-coordinate (Figure 3-7b). An Unsharp mask was used to avoid disconnected drop and reflection profiles in Figure 3-7b. For each X-coordinate value, the distance, L, between each point on the drop profile and its corresponding point from the reflection was calculated. This value should approach zero at the contact point where the drop profile meets its reflection on the solid

surface. The calculated values of L were plotted against the X-coordinates (Figure 3-7a) and a fourth order polynomial, L(x), was fitted to the resulting data points to obtain the X-coordinate of the contact point at L(x)=0 by extrapolation. Figure 3-8a shows a typical result for the right side of a sessile drop. This order of polynomial resulted in the highest correlation coefficient (R^2 defined in equation 3-2), which remained essentially constant for higher orders.

To find the Y-coordinate of the contact point, the middle points of vertical lines connecting each pixel on the drop profile and its corresponding pixel on the reflection (paired pixels in Figure 3-7b) were determined and averaged over the number of paired pixels. The calculated middle point remained essentially constant after certain number of paired pixels (Figure 3-8b). This approach identified the Y-coordinate of contact points accurately, within a tenth of a pixel.

3.2.4. Determination of Contact Angles

To determine the contact angle of a sessile drop, we first selected one half of the drop profile and fitted polynomials of different orders. The derivative of the fitted polynomial at the contact point was computed as the contact angle. The process was repeated for the second half of the drop and the average was taken as the contact angle of the drop on the solid surface. To avoid drop asymmetry that could result in different left and right contact angles, before each experiment we completely leveled the solid surface to ensure that the three-phase line of the drop is horizontal. In addition, drops with larger than 0.2° difference between their left and right contact angles were rejected by the program.

As expected, the calculated contact angles were sensitive to the polynomial order (O) and the number of pixels (P) selected from the three-phase contact point towards the drop apex for curve fitting. To determine optimum O and P, we plotted contact angles calculated for O=1 to 6 versus P (Figure 3-9a) and evaluated their significance using two statistical measures: correlation coefficient (R^2) in (Figure 3-9b) and the standard error (σ) in (Figure 3-9c):

$$R^2 = \frac{\sum_{i=1}^{n}(\tilde{y}_i - \bar{y})^2}{\sum_{i=1}^{n}(y_i - \bar{y})^2} \tag{3-2}$$

$$\sigma = \frac{[\sum_{i=1}^{n}(y_i - \tilde{y}_i)^2]^{\frac{1}{2}}}{\sqrt{n-(O+1)}}, \tag{3-3}$$

where y_i and $\tilde{y}_i$ are the observed value (experimental from edge detection) and predicted value by the polynomial, respectively, and $\bar{y}$ is the average of observed values. O represents the order and n is the total number of pixels used for curve fitting.

For a given sessile drop, contact angles reach a stable region beyond a certain number of pixels selected for curve fitting. At this region, contact angles vary only marginally (~0.4°). This region corresponds well with a low standard error and a correlation coefficient of close to unity (Figures 3-9b and 3-9c). Our detailed analysis of a large number of drops with a wide range of contact angles showed that the stable region of contact angles depends on selected O and P values. Therefore, we developed a differentiator mask to automatically identify this stable region for different O and P values, for a given sessile drop. For each polynomial order, this mask gave the length (in pixels) of the stable region in which variations in calculated contact angles were less than a pre-defined tolerance of ±0.2˚. The longest region resulting from a particular combination of O and P represented the contact angle of the drop on the surface.

We selected two drops with ADSA-P contact angles of 27.6º and 39.7º to evaluate this approach. Polynomials of orders 2 to 6 were fit to extracted edges of the drops. Table 3-1 shows the number of pixels in the stable region for each order. It is seen that the third order polynomial returns the longest stable region for the first drop, whereas the fourth order results in the longest stable region for the second drop. Therefore contact angles belonging to the longest stable regions were taken as representing the contact angles of these drops, i.e., 27.6º and 39.6º, respectively. This regime corresponds to a minimum standard error and $R^2 \approx 1$.

Unlike previous reports that suggest using a particular order of polynomial for sessile drops over a wide range of contact angles, we found that this strategy cannot determine contact angles, with accuracy close to that of ADSA-P. In fact, different orders of polynomials are required for curve fitting depending on the drop contact angle. To illustrate this point, we selected four sessile drops with contact angles in the range of 27.7˚ to 60.6˚, determined by ADSA-P (Figure 3-10). Drops with larger contact angles are discussed later. Following conclusions emerge from this figure:

(i) At small contact angles (e.g., a drop with a contact angle of 27.7˚), polynomials of smaller order require fewer pixels for curve fitting to reach a stable contact angle region. The stable region occurs for the second order polynomial around the 150th pixel and lasts until the 240th pixel with less than 0.5˚ degree difference from ADSA-P contact angle. For the third and fourth order polynomials, the stable contact angle region is observed at 400-650 pixels with 0.2˚-1˚ deviations from ADSA-P. Note that higher polynomial orders do not approach the ADSA-P result.

(ii) For drops with lager ADSA-P contact angles (e.g., 39.7˚, 54.6˚, and 60.6˚), there is a transition in the order of polynomials that best estimate true contact angles and result in a stable contact angle region that lasts over a large number of pixels. Smaller orders only cross the ADSA-P contact angle line and then significantly deviate from it.

(iii) With increase in the drop contact angle, higher polynomial orders require fewer pixels for curve fitting. For example, the onset of the stable contact angle regime with a fifth order polynomial fitting to the drop with a contact angle of 60.6˚ is around 200 pixels whereas for the case of contact angle of 39.7˚, this region starts at around 380 pixels. This suggests that higher polynomial orders are more suitable for drops with larger contact angles.

To find out the reason for either the lack of a stable region or the presence of stable contact angle regime over only a small number of pixels, we selected a sessile drop, fitted third and fifth order polynomials to the refined drop profile, and closely examined displacement of the Y-coordinate of the contact point. Figure 3-11a shows the fitted polynomials around the right contact point region. Examination of the profiles at the contact point region (inset) reveals deviation of the third order polynomial from experimental profile pixels. Unlike for the fifth order, the Y-coordinate of the contact point shifts continuously when specific number of pixels are eliminated from the entire selected pixels for fitting the third order polynomial (Figure 3-11b). This elimination starts from the apex region. With 35 discarded pixels, there is 0.4 pixels shift in the Y-coordinate of the contact point. Our curve fitting procedure uses several hundred pixels (e.g. 300-400), which will result in significant displacement of the contact point, and thus changes in

calculated contact angles. In the above example (Figure 3-11b), this would translate into 1.7° error in the calculated contact angle.

3.2.5 Dynamic Contact Angle Measurements Using Polynomial Fitting

Next we further tested the consistency of our procedure for dynamic contact angles measured with DMCPS on an EGC1700 fluoropolymer surface. A sessile drop was formed and the liquid was continuously supplied into the drop to advance the three-phase contact line, and subsequently withdrawn from it to recede the drop front. The rate of motion of the three-phase line was small enough (<1 mm/min) to ensure local equilibrium. Images were captured and analyzed using both ADSA-P and polynomials of fifth order. This order was selected based on a minimum standard error and $R^2 \approx 1$. The differentiator mask was applied to identify the stable region. Figure 3-12 shows both sets of contact angles and calculated averages. Overall the average results from Cartesian polynomial fitting match well with ADSA-P contact angles.

Next, we used this polynomial fitting strategy to determine dynamic advancing contact angles of various solid-liquid systems. Systems with an average advancing angle of ~40˚-70˚ were selected. The results from fitting different orders of polynomials are presented along with ADSA-P contact angles in Table 3-2. Results from fitting small order polynomials (second and third) show large errors for all cases. For drops with larger contact angles, higher orders (fifth and sixth) return better results and show smaller deviations from ADSA-P. Analysis of various systems suggests that fifth and sixth order polynomials can reproduce ADSA-P results for drops with a contact angle in the range of 40˚-50˚ and 50˚-60˚, respectively. Decreasing or increasing the order of polynomial by one can result in ~1-

2˚ difference with ADSA-P. For drops with contact angles larger than ~60˚, even these higher orders show significant deviations from ADSA-P results. This is evident from the ~3˚ difference for hexadecane contact angle on Teflon AF 1600 surfaces. A major problem is that as the drop curvature increases and contact angles shift more towards 90˚, the regions of the drop at its sides close to contact points tend towards a vertical line. Polynomials in Cartesian coordinates do not follow well enough the path of such profiles and result in an inaccurate fitting and error in contact angles. The problem becomes more evident for drops with contact angles around 90˚ and in the range of 90˚-180˚.

Overall these results suggest that determination of contact angles through polynomial fitting to drop profiles in the Cartesian system of pixel coordinates, $\{x_i,y_i\}\big|_{i=1}^{N}$, is sensitive both to the curvature of the drop and to the number of pixels selected for curve fitting. To determine contact angles within ±0.5˚ of ADSA-P results, one needs to identify the stable contact angle regime that corresponds with a minimum standard error and a high correlation coefficient. With the computational algorithm we have developed, the stable contact angle region is automatically detected using a differentiator mask for a given polynomial order to satisfy the statistical measures. The lengths of stable regions resulting from all polynomial orders are compared and the contact angle from polynomial fitting with the longest stable regime is selected. Unlike previous reports, if results accurate to ±0.5˚ of ADSA-P are desired for drops with a contact angle of <~65˚, this work suggest that there is no particular polynomial order that can accommodate drops with a wide range of curvatures nor can a fixed number of pixels be pre-selected. We note that this strategy works best for drops with a contact angle of smaller than ~65˚. With larger contact angles, >65˚, even high order polynomials show up to several degrees of error (see below) unless

the drop profile is rotated 90˚. We conclude that polynomial fitting in Cartesian coordinates does not produce consistent results for drops over a wide range of contact angles. We have developed a new approach that overcomes this limitation as discussed in the following section.

3.2.6. Transforming Drop Profile to Polar Coordinates

To better represent the close-to-vertical or vertical segments in the profile of sessile drops with contact angles approaching to or larger than 90˚, we transformed the pixel coordinates of the drop from Cartesian coordinates (x,y) to polar coordinates (r,φ) by placing the origin on the drop apex and transforming $\{x_i,y_i\}\big|_{i=1}^{N}$ to $\{r_i,\varphi_i\}\big|_{i=1}^{N}$ according to $x = r\cos\varphi$ and $y = r\sin\varphi$. We used equation 3-4 to fit a polynomial of order four to $\{r_i,\varphi_i\}\big|_{i=1}^{N}$:

$$r(\varphi) = \sum_{n=0}^{4} a_n \varphi^n \qquad (3\text{-}4)$$

Then, the contact angle (θ) was calculated as the slope of the tangent line at the contact point. We thoroughly examined this approach and found that a forth order polynomial fit yields comparable results to ADSA-P for a wide range of contact angles, with $R^2 \approx 1$ and a very small standard error.

In polar coordinates and along the drop profile from apex toward the right contact point, the slope of the tangent line varies smoothly from a positive value towards zero. On the other hand in Cartesian coordinates, the slope changes significantly from a negative value towards infinity, and again back to a positive value when the contact angle is larger than 90° (Figure 3-13). Smaller variations of the tangent-line in polar coordinates due to the transformation of close-to-vertical and vertical segments of the profile to more of

horizontal lines eliminate the need for large orders of polynomials for fitting. In addition, the rapid change in the tangent-line slope can be accompanied by changes in the sign of the drop profile curvature, which results in an undesired inflection point in fitted polynomials around the contact point.

To show the effect of this transformation on drop profiles, we selected three sessile drops with ADSA-P advancing contact angles of 44.4˚ (DMCPS-EGC1700 system), 88.2˚ (dibenzylamine-Teflon AF 1600 system), and 127.2˚ (water-Teflon AF 1600 system), and plotted their extracted profiles in a Cartesian coordinates system and the transformed edges in the polar system. This process converts vertically aligned pixels present in original drop profiles to approximately horizontal lines in the transformed profiles, which can be traced more accurately by polynomials (Figure 3-13).

We used this method to determine dynamic advancing and receding contact angles of dibenzylamine on Teflon AF 1600 films[124], [125]. The results are plotted in Figure 3-14 along with ADSA-P contact angles. The polar coordinate polynomial fitting (PPF) technique reproduced ADSA-P contact angles with an accuracy of ~0.6˚ for advancing and ~0.8˚ for receding angles. It is noted that due to a close-to-90° advancing angle, this solid-liquid system would be particularly challenging for polynomial fitting in a Cartesian system but the transformation enables accurate determination of contact angles with small standard deviations.

To demonstrate the broad utility of this approach, we applied the PPF method to sessile drops of solid-liquid systems with a wide range of contact angles, i.e. ~40˚ to ~170˚. For all systems, the PPF reproduces ADSA-P contact angles within <1˚. For example the contact angle of the hexadecane-Teflon AF 1600 system from polynomial fitting in

Cartesian coordinates that showed ~3˚ difference from ADSA-P result (Table 3-2) is now accurately reproduced using PPF within 0.3˚ of the ADSA-P contact angle. The performance of PPF is consistent for drops with different contact angles including the difficult-to-analyze range of 70˚-130˚. In addition for all systems, contact angles from images analyzed by PPF show much less variations and hence a smaller standard deviation compared to the same solid-liquid systems analyzed in Cartesian coordinates. Overall, PPF is more robust and much less sensitive to the order of polynomials. The fourth order can be used for all ranges of contact angle analyzed here.

We emphasize that the selection of the fourth order polynomial was because it consistently returned ADSA-P contact angles with a high accuracy. Although other orders may also work well, larger orders will increase computational time, and may induce the artifacts of too high a polynomial order, whereas smaller orders will reduce the specificity of fitting. The presented systems in Table 3-3 all have contact angles larger than 40°. Because the main purpose of transferring profiles to polar coordinates is to transform vertical or close-to-vertical lines to more of horizontal lines (Figure 3-13), for drops with small contact angles (e.g. θ<~40°) whose profiles lack a vertical segment, transformation of profiles to polar coordinates is not necessary and polynomial fitting in a Cartesian system still gives accurate contact angles.

3.3. Summary

The goal of this study was to critically evaluate polynomial fitting approach for contact angle determination from sessile drops and develop a new procedure to minimize calculation errors. We implemented a new subpixeling method to adjust the output of the

Canny edge detector and determine the physical profile of sessile drops. We determined contact points of a drop with the surface based on the symmetry of the drop profile and its reflection profile and elucidated the influence of displacing contact points on the accuracy of contact angles. Computed contact angles were sensitive to the order of the polynomial (O) in a Cartesian coordinates system and the number of pixels (P) selected for curve fitting. We implemented a differentiator mask to automatically find the longest stable contact angle regime for each polynomial order as a function of pixel numbers. The polynomial resulting in the longest stable regime and returning the lowest standard error and the highest correlation coefficient was always selected to determine contact angles. This approach returned contact angles with a high accuracy of <0.4° compared to ADSA-P results for solid-liquid systems with θ<~60º. We found that by increase in the contact angles of sessile drops up to this limit, higher orders of polynomial were needed to satisfy our statistical measures. Above this limit, even the sixth order polynomial returned significant deviations from ADSA-P results, necessitating drop rotation. Therefore unlike previous reports, we concluded that one single polynomial order could not address drops with a wide range of contact angles.

We resolved this problem by introducing polynomial fitting in the polar coordinates system. This tensor transformation does not change the physical nature of the images, only the representation of $\{x_i,y_i\}\big|_{i=1}^{N}$ is transformed to $\{r_i,\varphi_i\}\big|_{i=1}^{N}$. The contact angles are invariant to this transformation. Detected drop profiles were transformed to polar coordinates so as to eliminate close-to-vertical and vertical segments of the profile that pose a challenge to polynomial fitting in Cartesian coordinates. This transformation consistently reproduced ADSA-P contact angles in a wide range of 40˚-170˚ with an error

of <0.7º and small fluctuations around the mean. Overall, we found that this new method of polynomial fitting in polar coordinates is robust and can resolve contact angles from drops on hydrophilic to superhydrophobic surfaces.

Table 3-l The length of stable region for different polynomial orders obtained by applying the differentiator mask to two sessile drops with contact angles of 27.6° and 39.7°. Reprinted with permission from [123]. Copyright (2013) American Chemical Society.

	Polynomial order	Stable region length (n_{max})
Drop 1 (θ=27.6°)	2nd	87
	3rd	225
	4th	163
	5th	76
	6th	53
Drop 2 (θ=39.7°)	2nd	10
	3rd	75
	4th	253
	5th	131
	6th	97

Table 3-2 Contact angles (degrees) of several solid-liquid systems resulting from fitting different orders of polynomials in Cartesian coordinates, compared to ADSA-P. Reprinted with permission from [123]. Copyright (2013) American Chemical Society.

	Polynomial order in Cartesian coordinates					
Liquid-solid system	2	3	4	5	6	ADSA-P
Methyl salicylate-EGC1700	32.0 ±1.5	37.2 ±1.0	40.7 ±0.3	42.3 ±0.3	43.9 ±0.6	42.24 ±0.09
DMCPS-EGC1700	34.4 ±1.4	39.3 ±0.8	42.2 ±0.6	44.4 ±0.5	45.3 ±0.8	44.38 ±0.09
Decane-Teflon AF 1600	51.3 ±1.5	52.2 ±0.8	55.5 ±0.5	57.5 ±0.5	59.6 ±0.3	59.23 ±0.14
Hexadecane-Teflon AF 1600	54.0 ±2.2	60.3 ±2.0	60.2 ±1.5	64.9 ±1.2	66.5 ±1.5	69.50 ±0.18

Table 3-3 Contact angles (degrees) of several solid-liquid systems from PPF and ADSA-P[126]. Reprinted with permission from [123]. Copyright (2013) American Chemical Society.

Liquid-solid system	PPF	ADSA-P	Difference
Methyl salicylate-EGC1700	42.8±0.3	42.24±0.09	0.6
DMCPS-EGC1700	45.2±0.4	44.38±0.09	0.8
Decane-Teflon AF 1600	59.6±0.3	59.23±0.14	0.4
Hexadecane-Teflon AF 1600	69.2±0.2	69.50±0.18	0.3
Dibenzylamine-Teflon AF 1600	88.8±0.3	88.18±0.12	0.6
Water-Teflon AF1600	127.2±0.2	127.24±0.09	0.1
Water-Hexatriacontane	165.5±0.4	166.16±0.32	0.7

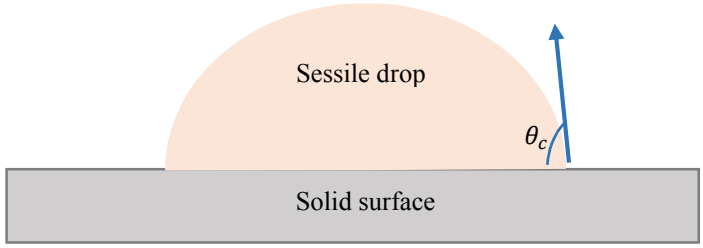

Figure 3-1 Schematic of a sessile drop on a solid surface. The contact angle, θ_c, forms at the contact point where the liquid drop meets the solid surface. Reprinted with permission from [123]. Copyright (2013) American Chemical Society.

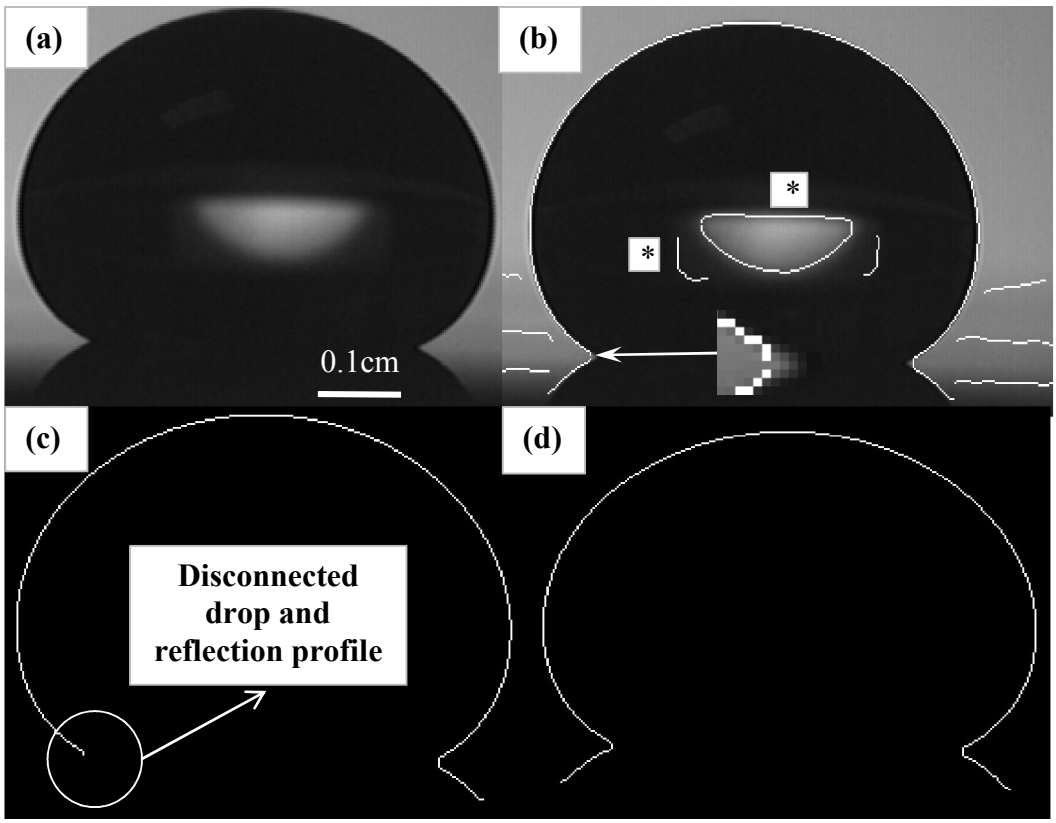

Figure 3-2 (a) The original sessile drop image of a water drop on Teflon, (b) the outcome of Canny edge detector (asterisks denote noise) and disconnected left side contact point, (c) the drop profile after eliminating noise, and (d) final drop profile after sharpening and smoothing. The origin of the coordinate system is set at the top left of the images and positive axes point to the right and bottom. Reprinted with permission from [123]. Copyright (2013) American Chemical Society.

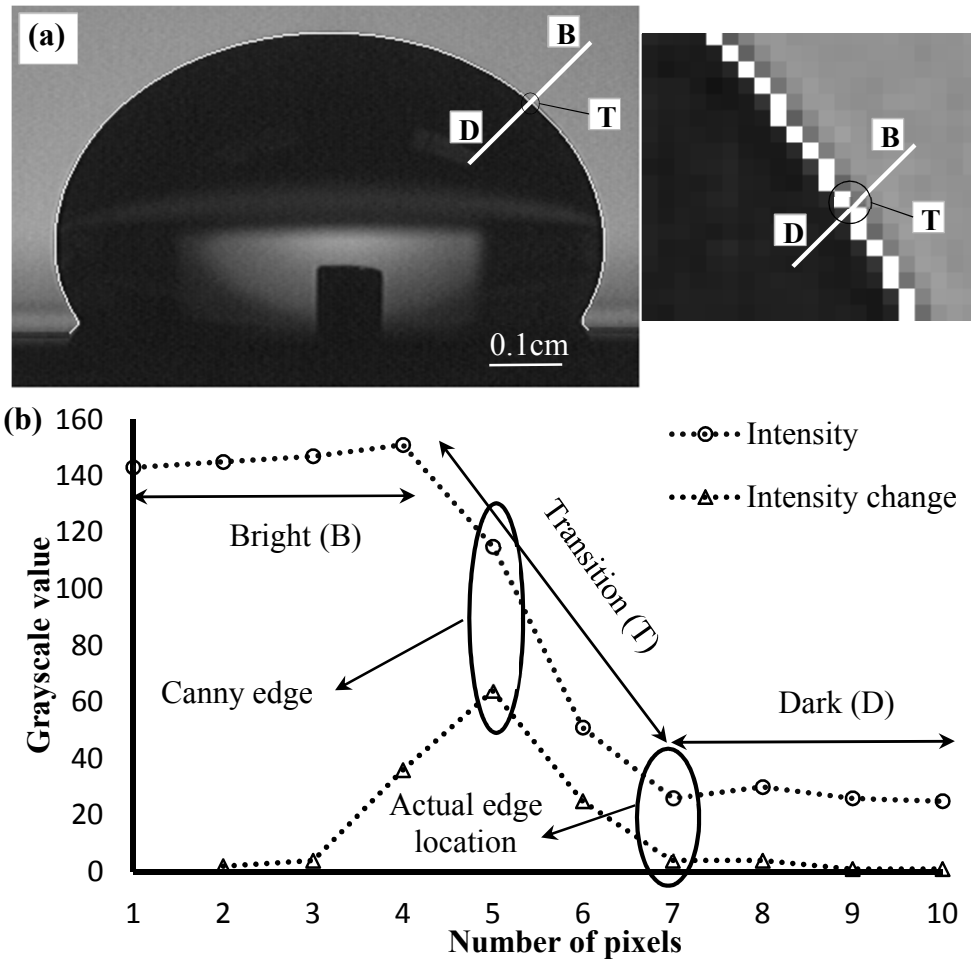

Figure 3-3 (a) Drop profile and three intensity regions of bright (B), transition (T) and dark (D) in a direction perpendicular to the drop profile, (b) intensity values and intensity variations along this line. Reprinted with permission from [123]. Copyright (2013) American Chemical Society.

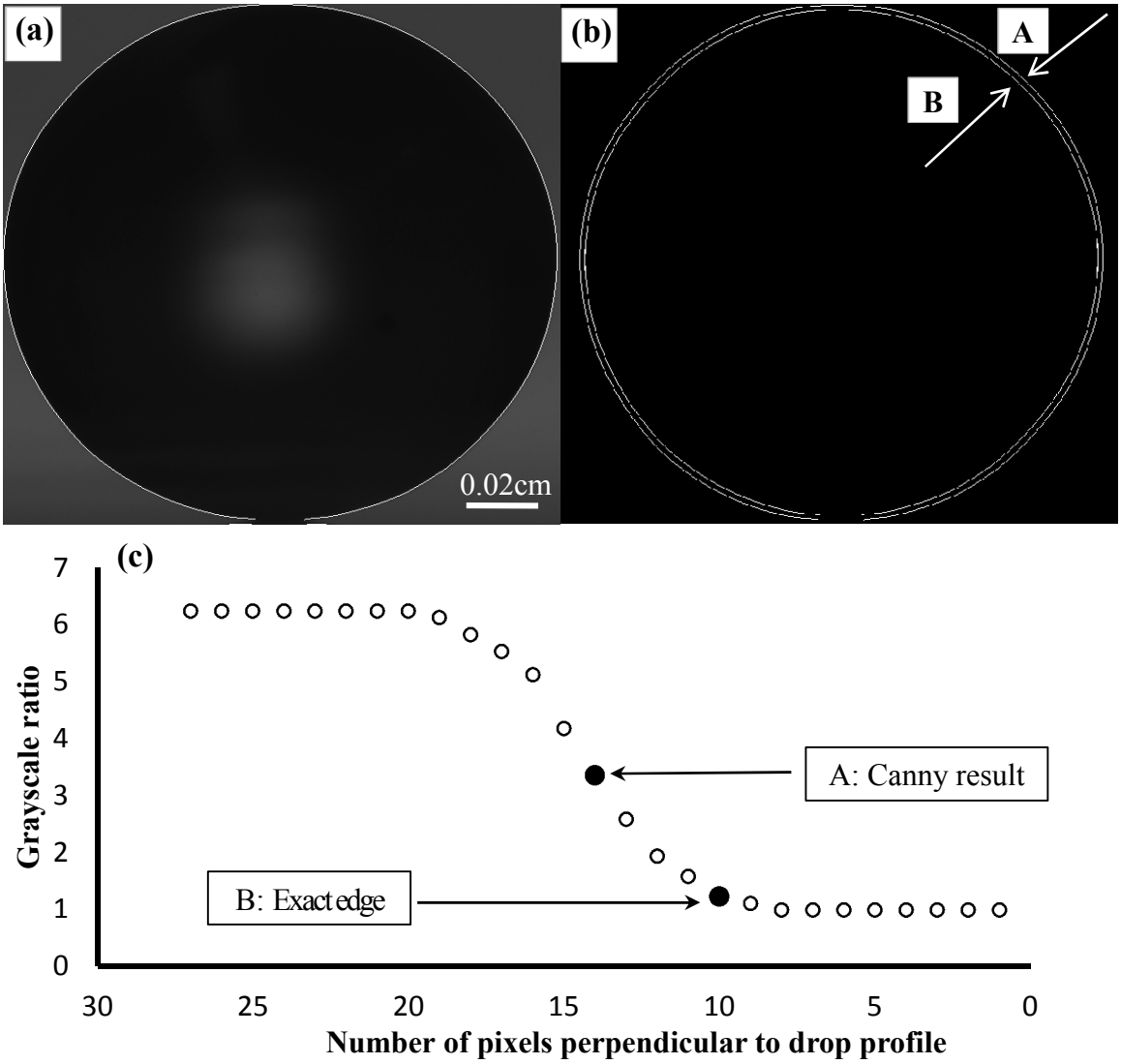

Figure 3-4 (a) Actual ball bearing image and the extracted edge using Canny, (b) displacement of the drop profile after applying subpixeling resolution, and (c) the ratio of grayscale of pixels to minimum grayscale in the image in the perpendicular direction to the drop profile. Reprinted with permission from [123]. Copyright (2013) American Chemical Society.

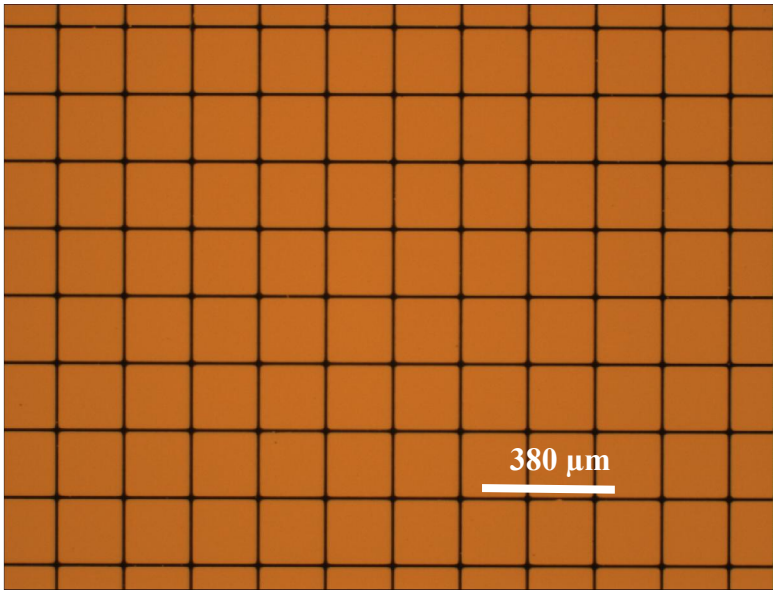

Figure 3-5 Calibration grid (Pyser-SGI Ltd.) imaged to calculate the pixel/µm ratio. Using the scale bar included in the figure, each pixel is 1.33 µm. Reprinted with permission from [123]. Copyright (2013) American Chemical Society.

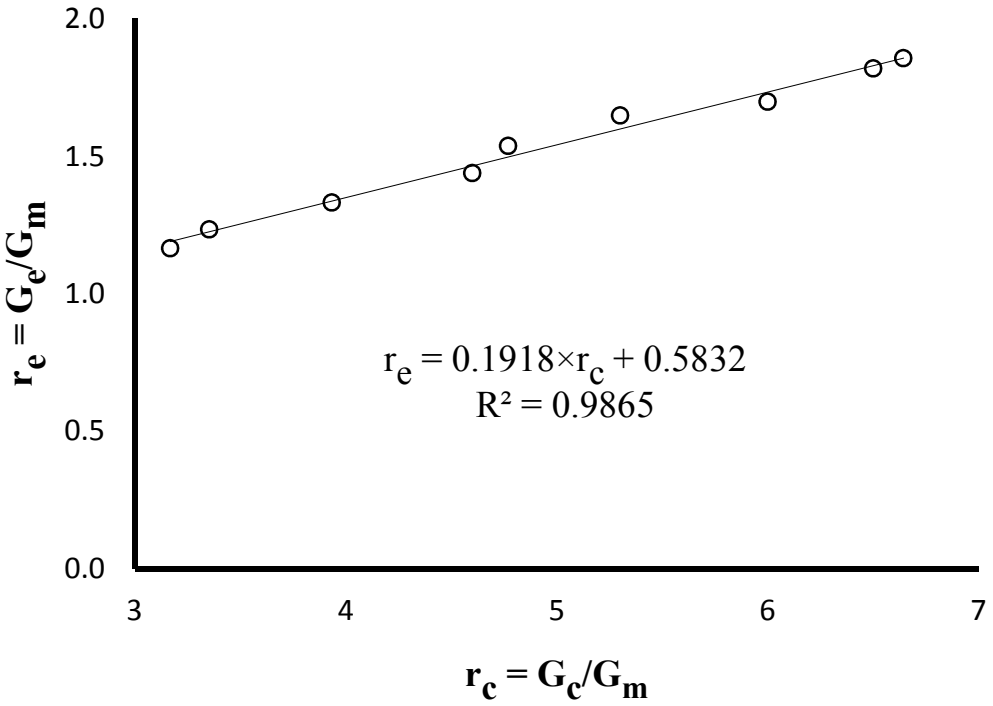

Figure 3-6 $r_e = \frac{G_e}{G_m}$ is the grayscale ratio at the exact edge location (Ge) to the minimum grayscale of the image (Gm) is shown versus $r_c = \frac{G_c}{G_m}$ from the edge detected by Canny (Gc). Reprinted with permission from [123]. Copyright (2013) American Chemical Society.

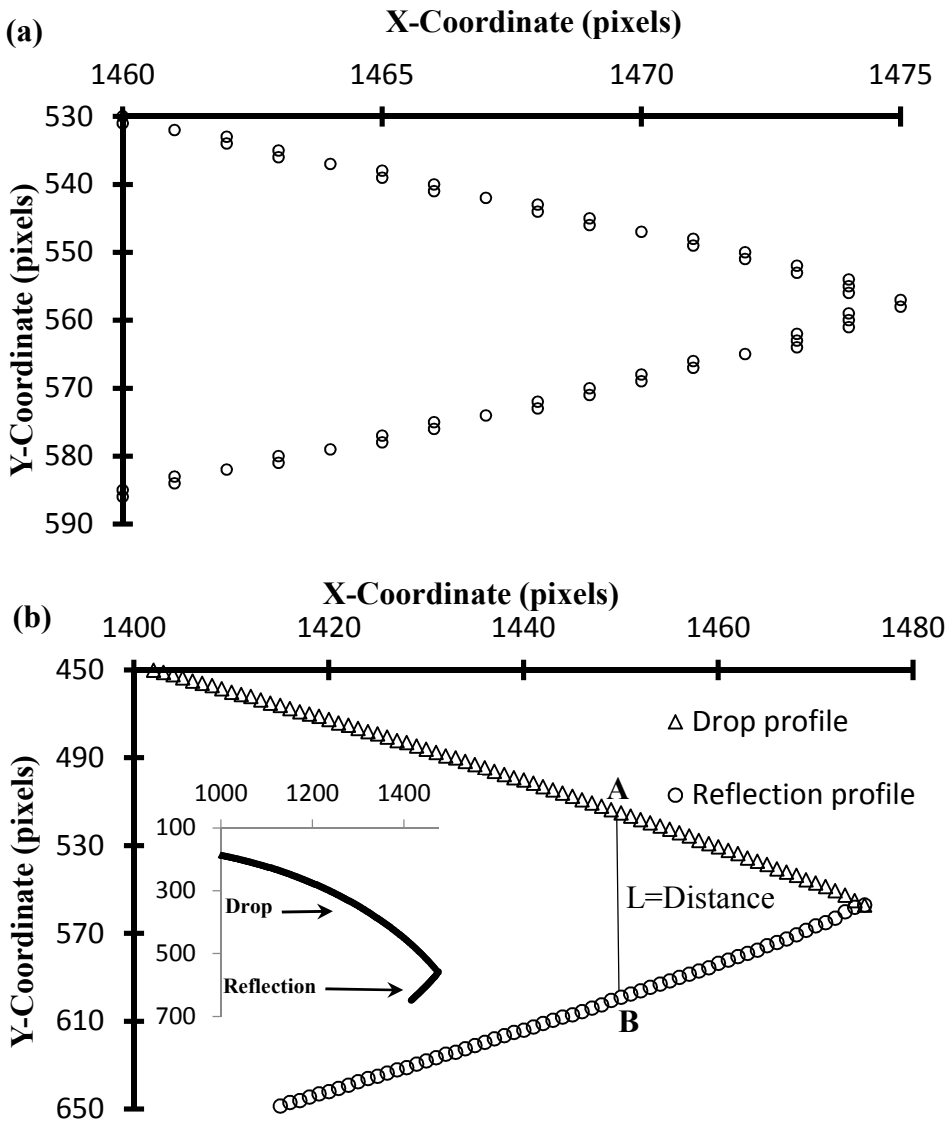

Figure 3-7 (a) The right side of the drop profile at the contact point region, (b) smoothened profile of the drop and its reflection on the surface and the defined distance, L. Reprinted with permission from [123]. Copyright (2013) American Chemical Society.

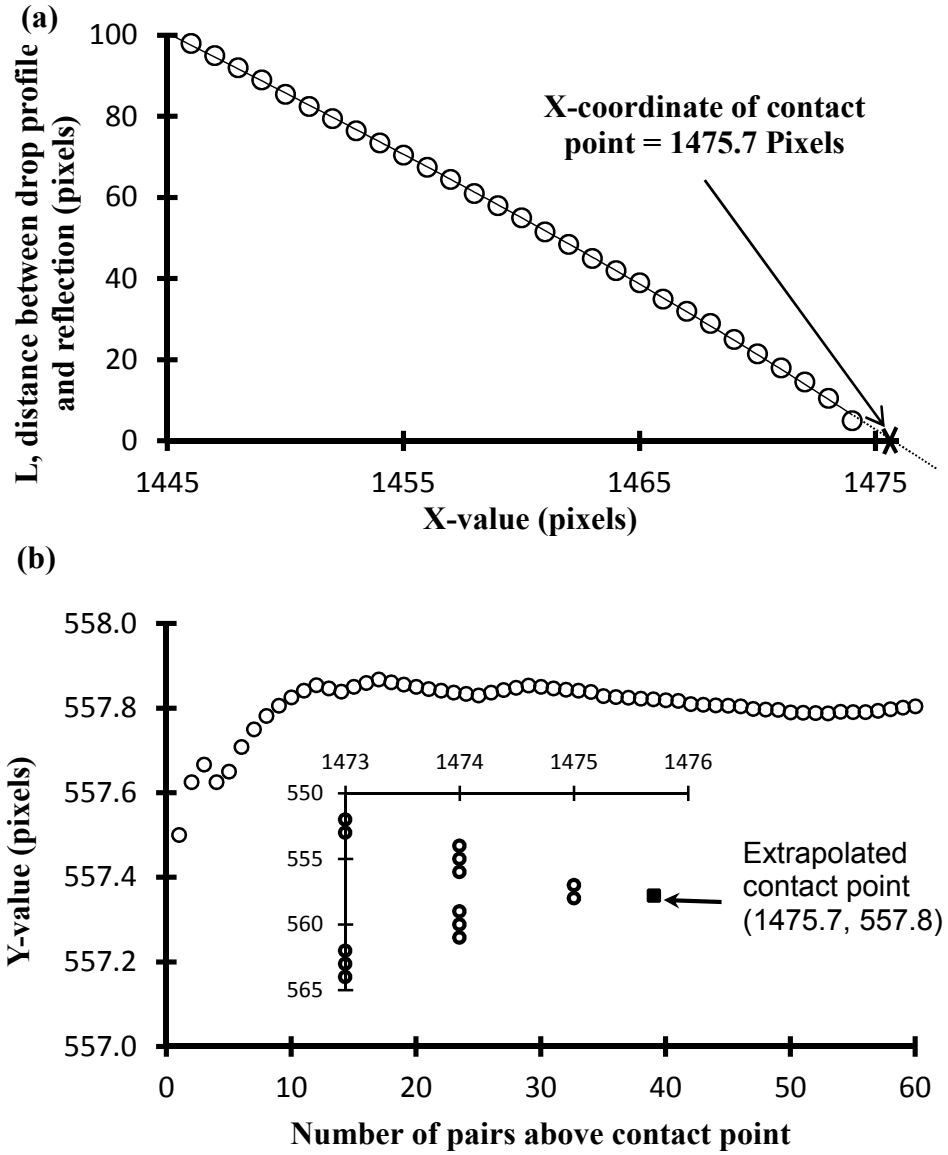

Figure 3-8 (a) Fitted curve to the distance, L, between each point on the drop profile and a corresponding point on its reflection profile to the extrapolated X-value of contact point, (b) Y-coordinate of the contact point versus number of paired pixels of the drop and reflection profiles. Reprinted with permission from [123]. Copyright (2013) American Chemical Society.

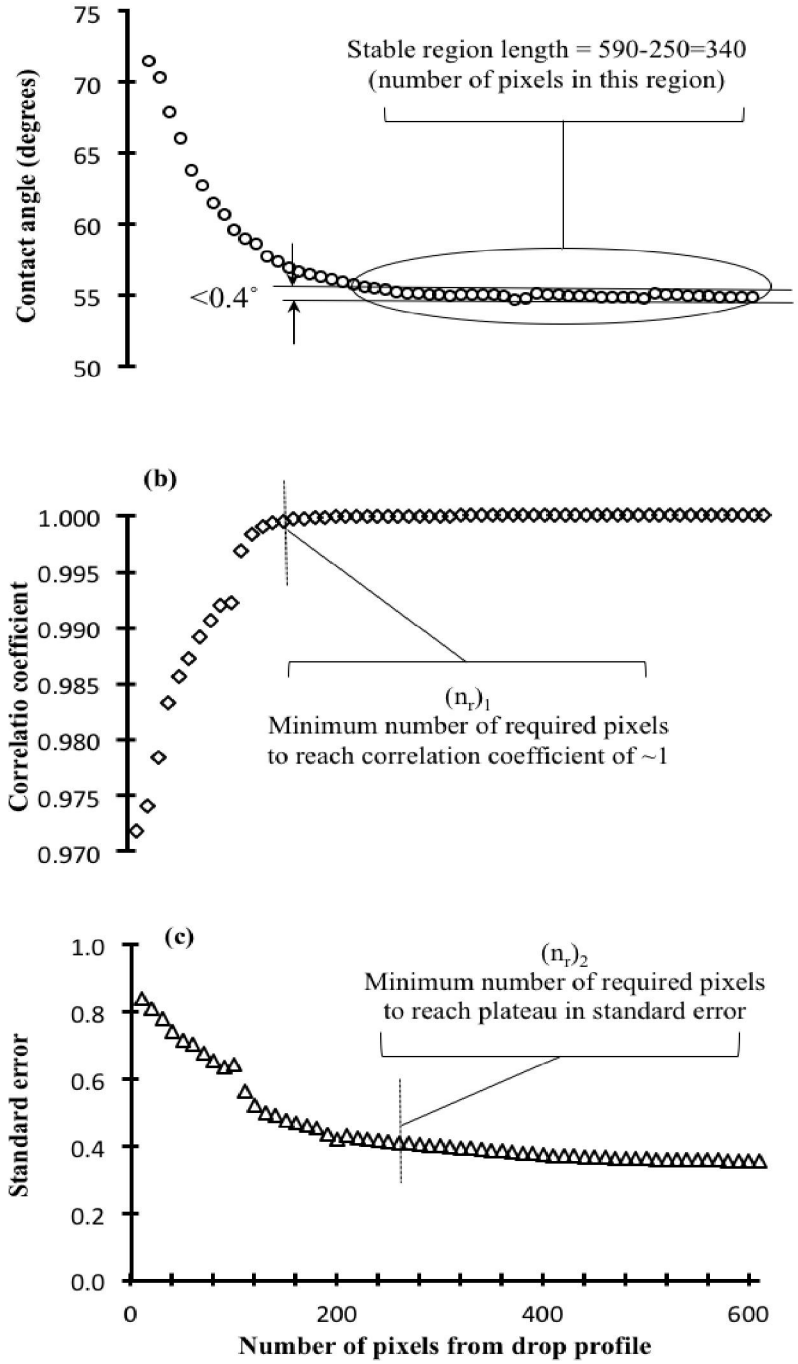

Figure 3-9 (a) Contact angle, (b) correlation coefficient, and (c) standard error resulted from fitting a fifth order polynomial to a sessile drop. The entire drop profile consists of 1220 pixels. Reprinted with permission from [123]. Copyright (2013) American Chemical Society.

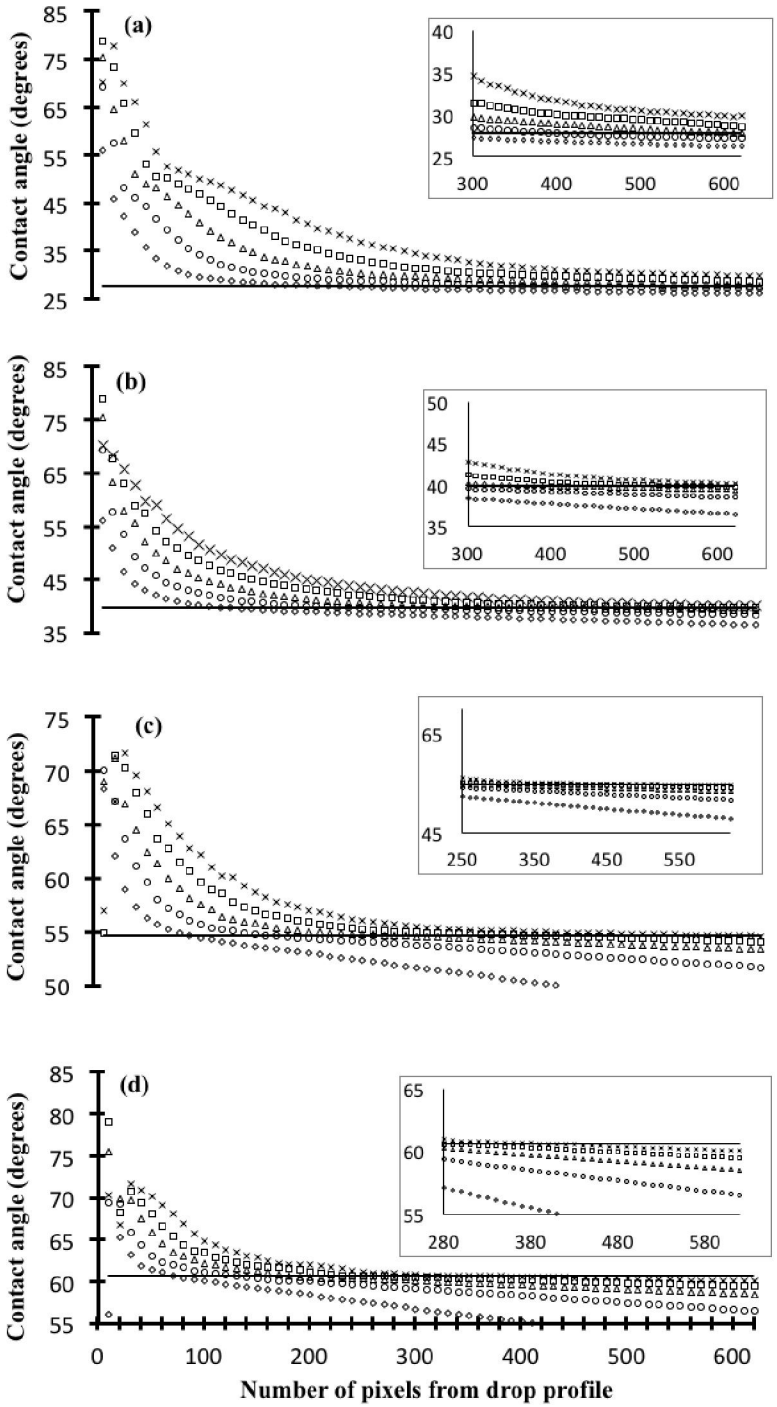

Figure 3-10 Contact angle versus number of selected pixels shown for different polynomial orders (2nd: diamond, 3rd: circle, 4th: triangle, 5th: square, 6th: cross) compared to ADSA-P results (solid lines) for droplets with contact angles of (a) 27.60˚, (b) 39.73˚, (c) 54.59˚, and (d) 60.63˚.

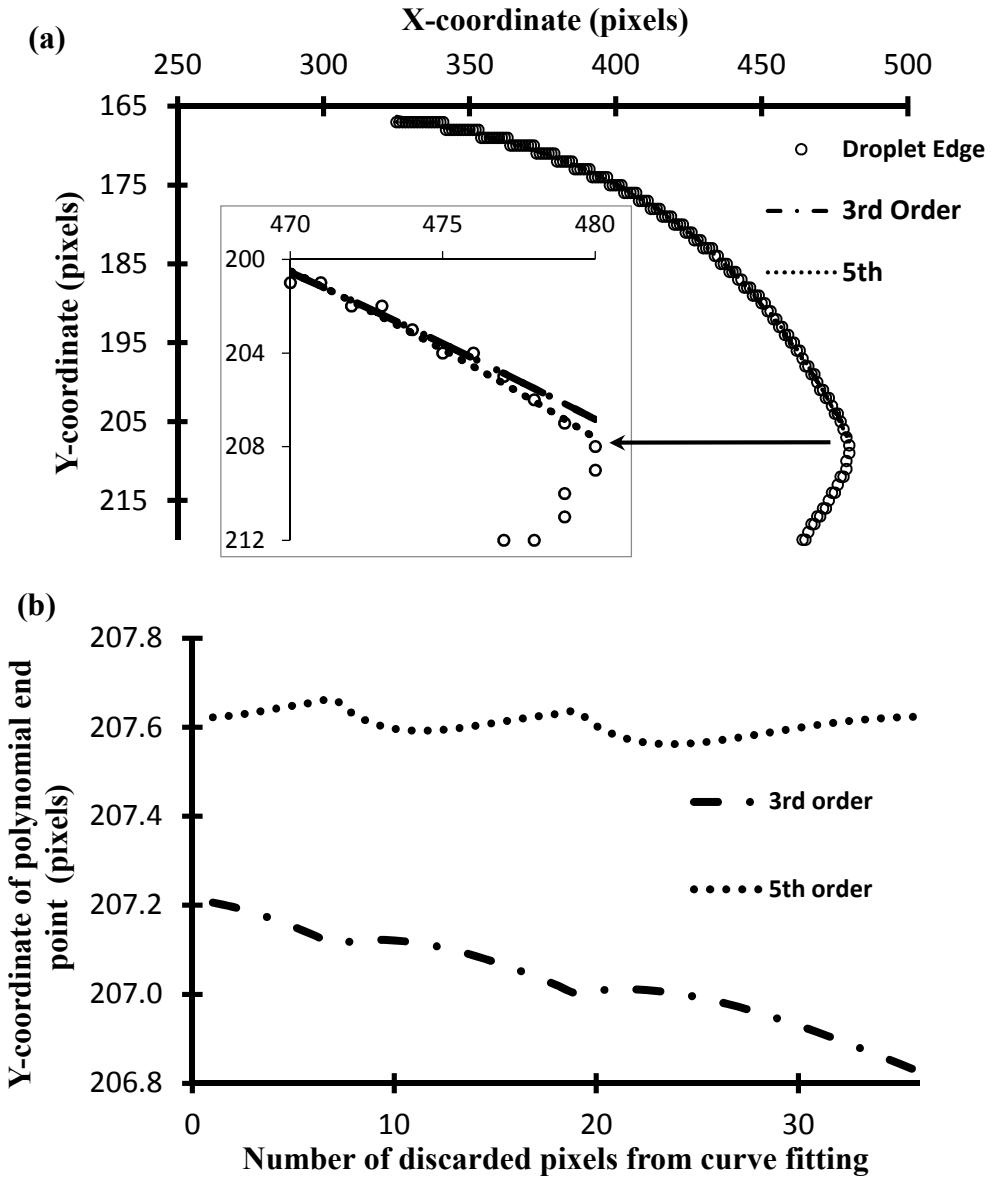

Figure 3-11 (a) Fifth and third order polynomials fitted to a drop profile around the right contact point, (b) a defined number of pixels are discarded from one half of the drop profile and third and fifth order polynomials are fitted to remaining pixels. Location of the contact point is stable with the fifth order polynomial but is displaced significantly for the third order. Reprinted with permission from [123]. Copyright (2013) American Chemical Society.

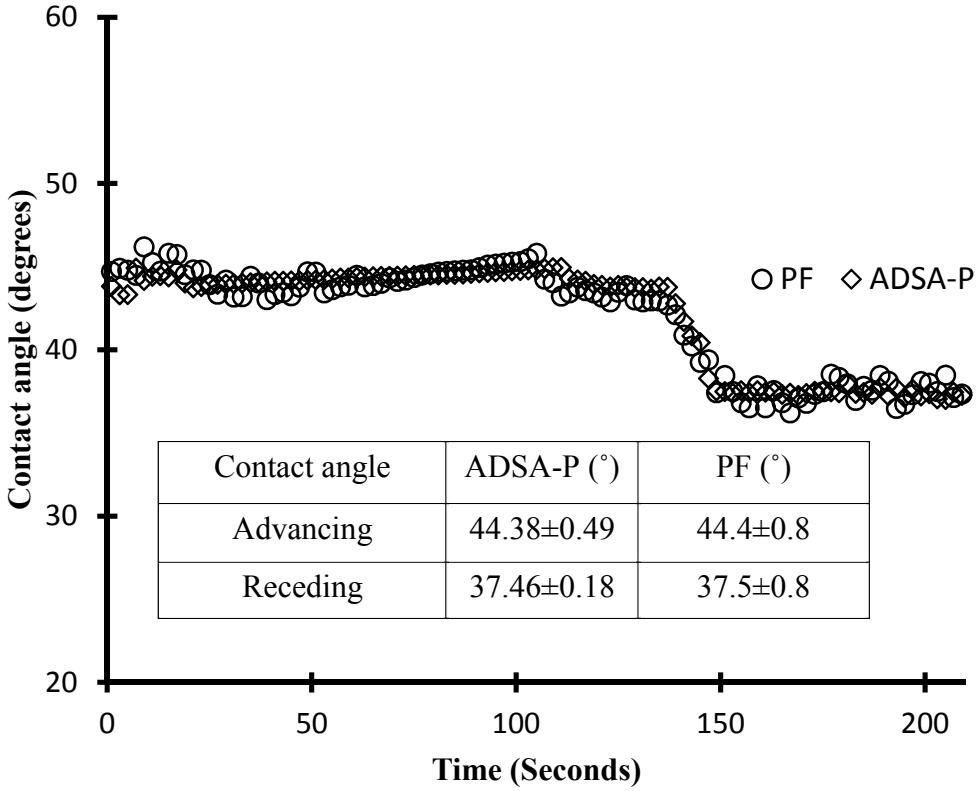

Contact angle	ADSA-P (˚)	PF (˚)
Advancing	44.38±0.49	44.4±0.8
Receding	37.46±0.18	37.5±0.8

Figure 3-12 Advancing and receding contact angles of DMCPS on an EGC1700 surface from fitting a polynomial of order 5 compared to ADSA-P. Reprinted with permission from [123]. Copyright (2013) American Chemical Society.

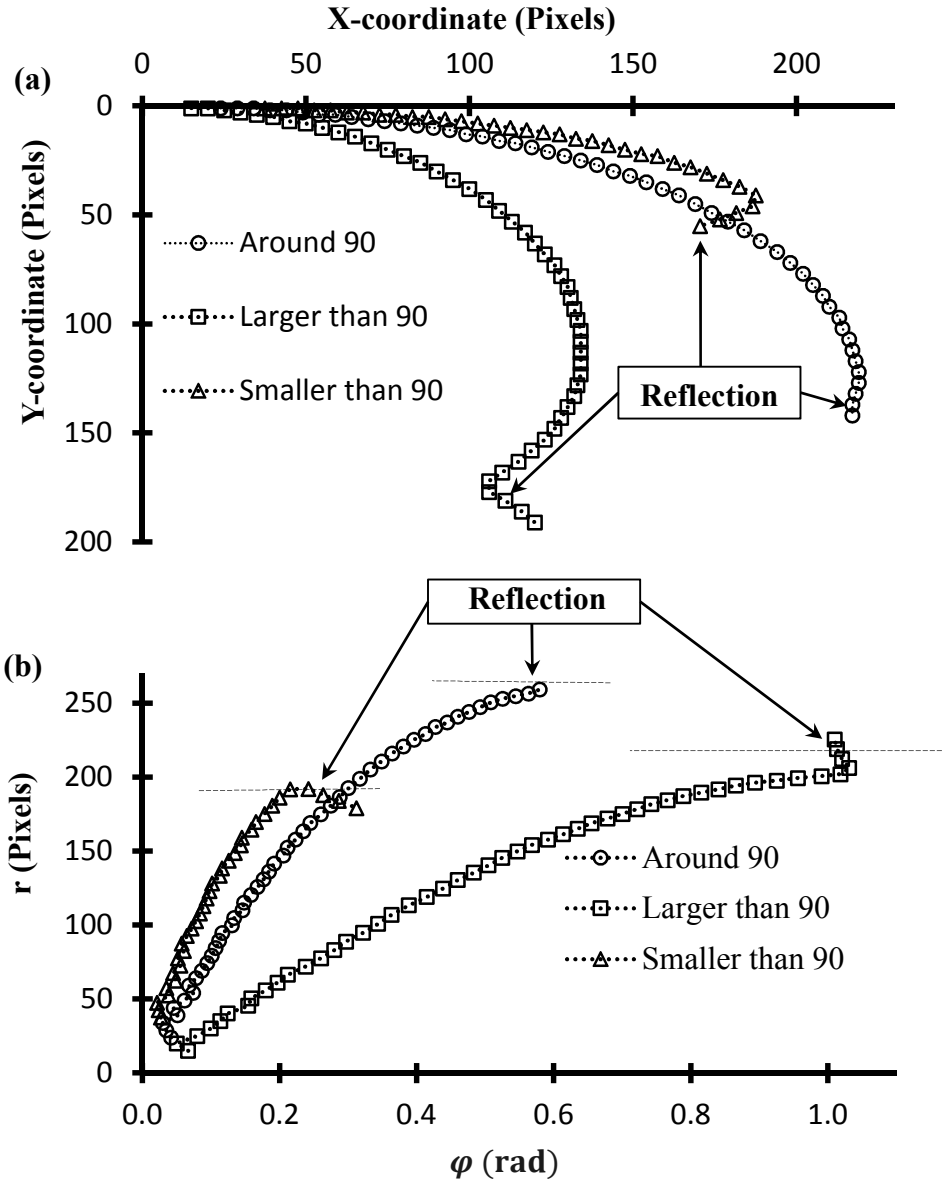

Figure 3-13 Transforming drop profiles from (a) Cartesian to (b) polar coordinates for three sample drops with contact angles of smaller than 90º, close to 90º, and larger than 90º. This transformation eliminates vertical segments of profiles in Cartesian coordinates and results in accurate contact angles from polynomial fitting as shown in Table 3-3. Reprinted with permission from [123]. Copyright (2013) American Chemical Society.

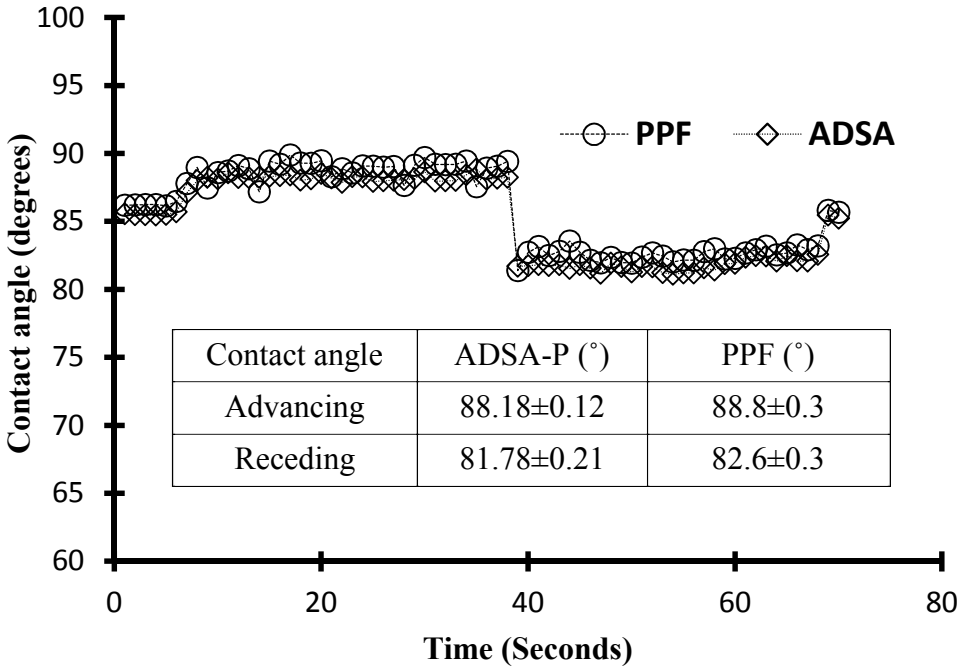

Figure 3-14 Advancing and receding contact angles of dibenzylamine on a Teflon AF 1600 surface computed from polynomial fitting in polar coordinates (PPF) and ADSA-P. Reprinted with permission from [123]. Copyright (2013) American Chemical Society.

CHAPTER IV

MEASUREMENT OF ULTRALOW INTERFACIAL TENSIONS OF ATPS

Aqueous solutions of different polymers can separate and form aqueous two-phase systems (ATPS). ATPS provide an aqueous, biocompatible, and mild environment for separation and fractionation of biomolecules. The interfacial tension between the two aqueous phases plays a major role in ATPS-mediated partition of biomolecules. Due to the two highly aqueous phases, the interfacial tensions between them is usually 3-4 orders of magnitude smaller than conventional fluid-liquid systems[116], i.e., ~1-100 $\mu J/m^2$ for ATPS compared to ~72 mJ/m^2 for a water–air interface. This poses a major challenge for the reproducible measurements of interfacial tensions of these systems. Interfacial tensions of ATPS have not been studied systematically due to the difficulty of handling these systems and reproducibly measuring such small magnitudes[97], [98], [127], [128].

We address the need for precise determination of ultralow interfacial tensions using an axisymmetric drop shape analysis (ADSA) approach. Despite being the most reliable technique for measuring surface and interfacial tensions of liquid-fluid systems based on drop shape, ADSA has not been used before for systematic studies with ATPS[129]–[132]. Therefore, our work presents the first study of this kind. We systematically study a series of polymeric ATPS comprising of polyethylene glycol (PEG) and dextran (DEX) as the phase-forming polymers with varying concentrations. Changing the concentrations of phase-forming polymers is expected to vary the interfacial tension. Sessile and pendant

drops of the denser DEX phase are formed within the immersion PEG phase to determine the interfacial tension. Specific criteria are used to reproducibly determine ultralow interfacial tensions of the ATPS from both drop configurations[133].

4.1. Materials and Methods

In this section preparation of two-phase solutions for interfacial tension measurements is explained. Formation of sessile and pendant drops of two-phase solutions, imaging of drops, and the ADSA methodology are discussed. The densities of two-phase solutions are measured using a density meter as explained in chapter II (2.1.2).

4.1.1. Preparation of Aqueous Two-Phase Systems (ATPS)

A total of eight two-phase solutions were generated using different concentrations of polyethylene glycol (PEG, Mw: 35k, Sigma-Aldrich) and dextran (DEX, Mw: 500k, Pharmacosmos) used as phase-forming polymers. Aqueous solutions were made by dissolving each polymer in distilled, ultrapure water, dH2O (Barnstead Nanopure system, Thermo Scientific). Stock aqueous solutions of each polymer with desired concentrations were prepared in dH2O, each with a nominal volume of 20 ml. To simplify sample preparation, concentration of each stock solution was calculated using the mass of each polymer per total volume of the stock solution of the polymer, i.e. in (w/v). For example, a 20 ml stock solution of 5%(w/v) PEG contained 1gr of polymer and 19 ml of water. The final volume slightly deviated from 20 ml and therefore we used nominal volume for stock solutions. Then, the entire volume of stock solutions of PEG and DEX phases of each two-phase solutions were thoroughly mixed in a conical tube by inverting and vortexing for 10

min to form a turbid solution called the initial two-phase solution. The weight fractions of PEG and DEX in each initial two-phase solutions were calculated by dividing the mass of each polymer in its respective stock solution to the total mass of the initial ATPS solution, i.e. $W^I_{PEG}\left[\frac{w}{w}\right] = \frac{M^P_{PEG}[gr]}{M_{total}[gr]}$ and $W^I_{DEX}\left[\frac{w}{w}\right] = \frac{M^D_{DEX}[gr]}{M_{total}[gr]}$.

The calculated weight fractions were used to present each initial two-phase solution in a phase diagram (section 4.1.2). After mixing the two stock solutions, the initial two-phase solution was transferred into a graduated glass funnel (Chemglass Life Sciences) and kept at 24±1ºC to form two clear segregated phases. The time required for complete separation varied from one day to several weeks depending on polymer concentrations; systems with higher concentrations required longer time to equilibrate. Finally, after the two phases were completely clear, the top PEG-rich phase was removed from the top of the funnel using a pipette. The bottom DEX-rich phase was discharged from bottom of the funnel by turning an adjustable bore metering plug open to allow dispensing at a slow flow rate. We avoided removing PEG and DEX phase solutions from the interfacial region to prevent mixing of segregated phases.

4.1.2. Determining Tie-Lines and Compositions of Equilibrated Phases

A tie-line in a phase diagram passes through a point specifying the concentration of each polymer in the initial two-phase solution and intersects with the binodal curve at two node points to yield concentrations of polymers in each of the final, equilibrated phases. An increase in the tie-line length shifts it diagonally farther away from the critical point. In this study, concentrations of polymers in the DEX-rich phase were determined by intersecting an isopycnic line with the binodal curve. The isopycnic line equation was

derived assuming that the total specific volume of each polymer solution is sum of contribution of its components. Equation 4-1 below relates the weight fraction of PEG ($[PEG]_D$) to the weight fraction of DEX ($[DEX]_D$) in the bottom, DEX-rich phase using densities of water (ρ_w) and the DEX-rich phase solution (ρ_D):

$$[PEG]_D = \frac{1}{C_1}\left(\frac{1}{\rho_w} - \frac{1}{\rho_D} - c_2[DEX]_D\right) \quad (4\text{-}1)$$

Here, $\rho_w = 0.997$ gr/cm^3 and c_1=0.1568 cm^3/gr and c_2=0.3811 cm^3/gr represent PEG-water and DEX-water specific volume differences, respectively, in agreement with previously reported values. After identifying the location of the DEX-rich phase on the binodal curve, this point was connected to the point of concentrations of PEG and DEX in the initial ATPS solution. The resulting line was extrapolated to intersect with the binodal curve and obtain the location of the PEG-rich phase to determine the concentration of PEG and DEX in the top, PEG-rich phase. For each ATPS in Table 4- 1 (numbered 1-8), polymer weight fractions are given in stock solutions of PEG and DEX phases, in the initial ATPS solution, and in equilibrated PEG-rich and DEX-rich phases.

4.1.3. Formation of Sessile and Pendant Drops

All drops were formed using equilibrated phases of ATPS. Sessile drops were formed by dispensing a small volume of the DEX phase into a rectangular quartz cuvette of 1 cm × 1cm cross sectional area (Helma) containing 700 µl of the PEG phase. Dispensing was controlled using a syringe pump (Chemyx) to inject the DEX phase through 19-gauge Teflon tubing. Connections were sealed using threaded Teflon stoppers. The Teflon tubing was fixed at a vertical position by passing through a hollow, stainless steel cylindrical tube; then it was manually lowered and inserted into the PEG phase solution. This resulted in the

formation of a continuously growing drop due to autonomous dispensing of the DEX phase solution within the PEG phase. The autonomous dispensing happens because the ultralow interfacial tension of ATPS cannot overcome the gravitational force to hold the drop at the tip of the tubing. Adjusting the flow rate using the syringe pump controlled the autonomous dispensing to generate sessile drops of 0.11–2.30 µl within the PEG phase. Experiments for each drop volume had 10 replicates.

Pendant drops were formed at the end of 19- or 24-gauge needles connected to a 2.5 µl glass syringe (Hamilton). The DEX phase was loaded into a syringe. The syringe assembly was held vertical on a micro-positioning stage equipped with an X-Y translational control knob. The stage itself was assembled on an adjustable stainless steel clamp, which was mounted on the top end of a vertical rod fixed on an optical table from the bottom end. The needle was lowered and gradually inserted into a rectangular glass cuvette of 1 cm × 1cm cross sectional area (Helma) containing 1 ml of the aqueous PEG phase. The aqueous DEX phase autonomously dispensed resulting in a growing pendant drop at the tip of the needle. Images of the growing drop were captured every 0.1 sec over a time interval of 10 sec and recorded for analysis. To minimize the effect of temperature on interfacial tensions of ATPS, all experiments were conducted at an ambient temperature of 24±1ºC.

4.1.4 Experimental Setup and Image Acquisition

The instrument setup is comprised of several components assembled on an optical, vibration-free table (Newport). A camera-lens unit was used to capture drop images at magnifications of 3.2X–9.2X by changing the focal length of a 112 mm-WD lens (LEICA,

Z16 APO). Images were taken using a digital camera (JAI Ltd., CB-200GE) with the capability of capturing 25 fps for time-lapse imaging. The camera software saved images with a maximum size of 1624×1236 pixels onto a PC. A combination of a light source (Thorlabs, OLS1) and glass diffusers provided a uniformly lit background in all images. The glass cell was positioned on a horizontal platform that was leveled prior to experiments using a bubble level. All units were mounted on a linear rail. The setup schematic is shown in Figure 4-1. Needles and syringes were cleaned by sonication in acetone, methanol, and dH2O separately, each for three times and each time for 20 min, suctioned through a vacuum line, and dried in a 65ºC oven (Binder) for 5 hrs.

4.1.5 Axisymmetric Drop Shape Analysis (ADSA)

The ADSA methodology was used to measure interfacial tensions of ATPS. ADSA estimates the interfacial tension of each system based on a best fit between an experimental drop profile and theoretical Laplacian curves. An image processing module in ADSA extracts the drop profile as a series of experimental pixel points. Then, using the following equation 4-2, ADSA searches for a best Laplacian curve to fit the drop profile through minimizing the error of fitting.

$$\gamma\left(\frac{1}{R_1}+\frac{1}{R_2}\right)=\Delta P_0+\Delta\rho g z \qquad (4\text{-}2)$$

In this equation, γ represents the interfacial tension, R_1 and R_2 are first and second radii of curvature (the sum is twice the mean curvature), respectively, and ΔP_0 is pressure difference at the apex of the drop. The apex point is on the reference plane, z is the vertical distance from the reference plane, and $\Delta\rho$ represents the density difference between the two immiscible aqueous phases. The radius of curvature at the apex, R_0, resulting from

curve fitting is used to estimate pressure difference at the apex from an initial estimated value of γ using equations 4-3 and 4-4. The resulting ΔP_0 is used to determine the interfacial tension from equation 4-2 and optimize the Laplacian curve fitting. The process terminates when the error of fitting becomes smaller than a pre-defined threshold value. Note that due to the axial symmetry of the interface, the curvature at the apex is constant in all directions and the two principal radii of curvature are equal, resulting in equation 4-3. Then equation 4-4 is obtained by combining equations 4-2 and 4-3.

$$\frac{1}{R_1} = \frac{1}{R_2} = \frac{1}{R_0} = b \tag{4-3}$$

$$b = \frac{\Delta P_0}{2\gamma} \tag{4-4}$$

4.1.6. Statistical Analysis

Statistical analysis is performed using Matlab. Results are presented as mean ± standard deviation. Differences between means are determined using one-way ANOVA. P-value smaller than 0.05 is considered as statistically significantly different.

4.2. RESULTS AND DISCUSSION

In this section the interfacial tension measurements of two-phase solutions using sessile drop and pendant drop configurations are presented. A criterion is used for evaluating pendant drops to ensure formation of well-deformed Laplacian drops and hence, reliable interfacial tension data. Finally, a simple criterion is introduced for evaluation of the well-deformity of sessile drops.

4.2.1. Reproducing Interfacial Tensions of Conventional Systems

Prior to interfacial measurements with two-phase solutions, we first conducted pendant drop experiments with three well documented air-liquid and liquid-liquid systems to ensure that we could reproduce literature values within appropriate uncertainties. The systems were selected to cover a wide range of interfacial tensions. We set 10 replicates for each system. Table 4-2 shows that our interfacial tension measurements reproduced the literature values for all these systems[131], [134].

4.2.2. Interfacial Tension Measurements with ATPS

Determination of interfacial tensions of conventional air-liquid and liquid-liquid systems using ADSA is sensitive to drop shape/volume. The accuracy of ADSA is significantly reduced for small, close-to-spherical drops. Previous work indicates that formation of well-deformed drops is necessary for reliable surface/interfacial tension measurements with ADSA. A quantitative criterion, the dimensionless "shape parameter", was defined to determine a range of volumes for pendant drops that generates consistent surface/interfacial tensions. We determined the shape parameter of pendant drops using the original formulation and developed a simple method to evaluate the "well-deformity" of sessile drops of ATPS, which assures accurate interfacial tension values from ADSA. We selected the system number 1 of Table 4-1 to conduct interfacial tension measurements with both pendant and sessile drops in a wide range of drop volumes to identify working volumes for well-deformed ATPS drops.

4.2.2.1. Sessile Drops

Aqueous DEX phase sessile drops were dispensed into the immersion PEG phase and allowed to equilibrate for 30 min before imaging. Eleven different drop volumes in the range of 0.11–2.30 µl, each with 10 replicates, were used. Interfacial tensions of the ATPS from sessile drop measurements are presented versus drop volume in Figure 4-2. The results are divided into three regimes. In regime I with drop volumes of <0.80 µl, measured interfacial tensions show large variations of up to 60% and result in large standard deviations. Then in regime II, the measured values show an increase with increase in the drop volume up to about 1.50 µl. The autonomous dispensing of the aqueous DEX phase made it difficult to generate more data points in this regime. Finally in regime III, interfacial tensions become independent of drop volume and show a plateau at 0.012±0.001 mJ/m^2. The critical volume of the DEX phase sessile drops required to consistently measure this interfacial tension value is >1.60 µl. We note that the difficulty of working with very small drop volumes and the autonomous dispensing of the DEX phase, once the Teflon tubing entered the immersion PEG phase, resulted in small variations of a pre-defined dispensed volume from one experiment to another. Horizontal error bars in Figure 4-2 indicate this point.

To explore the reason underlying these results, we selected a 0.42 µl sessile drop from regime I and a 2.04 µl sessile drop from regime III, computationally determined the error of fitting of Laplacian curves to the extracted profile of each drop, and plotted the error of fitting versus drop curvature at the apex, i.e., the b-value used during optimization of Laplacian curve fitting in ADSA. The b-value in equation 4-4 is computed based on an initial, user-defined estimate for the interfacial tension that corresponds to a unique

Laplacian profile. With the 0.42 µl drop of regime I, there are four local minima for the error of fitting (Figure 4-3a). Each minimum corresponds to a unique interfacial tension value shown. Therefore ADSA may converge at one of these local minima depending on the initial b-value used for the optimization process. This causes large variations in the interfacial tension values of small-volume drops of regime I. On the other hand with the 2.04 µl drop of regime III, although the minimum error is not unique, the corresponding b-values are very close, i.e. within ~5% error (Figure 4-3b; compare the range of b-value axis in panels a and b). Even if the initial user-defined estimate for the interfacial tension, and hence the corresponding b-value, may be far from this narrow window, ADSA converges at one of these b-values. This analysis substantiates that generating well-deformed sessile drops, such as those of regime III, is crucial for accurate measurements of ultralow interfacial tensions of ATPS, in agreement with previous findings for conventional fluid-liquid systems.

To define a criterion for the "well-deformity" of sessile drops, we compared sum of root mean square of normal distances (cumulative error) between pixels on the drop profile and corresponding points from segments of a circle or an ellipse fitted to the profile. We used this strategy for drops made with the system number 1 of Table 4- 1 and plotted the results against the volume of sessile drops (Figure 4-4). Each point in this figure corresponds to a specific drop volume and represents an average of five replicates. As expected, the cumulative error resulting from fitting a segment of a circle continuously increases with drop volume due to a larger deviation of drop shape from a circle segment. This increase becomes marginal for sessile drop of >~1.60 µl volume. On the other hand, fitting a segment of an ellipse to low volume drops gives large cumulative errors, which

then decreases by increase in drop volume and reaches a plateau for sufficiently large drops of >~1.60 µl. Based on this analysis, sessile drops with a volume of larger than 1.60 µl should result in measurement of consistent interfacial tensions for this ATPS. This is indeed the case and in agreement with interfacial tension results presented in Figure 4-2. It is noted that this critical volume will increase for two-phase solutions with larger concentrations of phase-forming polymers. That is, the larger interfacial tension, the larger drop volume to form a well-deformed sessile drop. For example for the system number 4 of Table 4-1, we found that the critical volume of sessile drops is 2.1 µl. Due to the difficulty with handling and imaging large sessile drops, we selected the pendant drop technique for interfacial tension measurements for all eight two-phase systems, as explained below.

4.2.2.2. Pendant Drops

Inserting the needle of a syringe containing the aqueous DEX phase into the PEG phase solution results in continuous dispensing of the DEX phase and a growing pendant drop. Figure 4-5 shows the evolution of drop volume and plots the interfacial tension for each drop from ADSA versus its shape parameter. For each drop, the shape parameter, $P(r_\theta, R_0)$, is computed by numerical integration using the following equation:

$$P = \frac{\left| \int_0^{2\pi} \int_0^{r_\theta} r\, dr\, d\theta - \pi R_0^2 \right|}{\int_0^{2\pi} \int_0^{r_\theta} r\, dr\, d\theta}, \qquad (4\text{-}5)$$

where, the numerator is the absolute value of the difference between the projected area of the image of the drop and the inscribed circle with radius R_0, and the denominator presents the projected area of the drop computed from the experimental profile obtained from a drop

image. As expected, the shape parameter increases with drop volume. Measured interfacial tensions at small shape parameters are inconsistent, increase for larger drops, and finally reach a plateau at 0.012±0.001 mJ/m^2 for shape parameters of 0.38-0.45. This plateau region represents the critical shape parameter range required to obtain interfacial tensions independent of pendant drops volume. Further increase in the volume of growing pendant drops of the DEX phase resulted in continuous elongation of drops. Unlike in conventional liquid-liquid systems, these elongated ATPS drops did not detach from the needle due to their ultralow interfacial tensions. The elongated drops that occurred beyond a shape parameter of 0.45 were non-Laplacian and excluded from analysis for interfacial tension measurements using ADSA. Therefore for all aqueous biphasic systems studied with a pendant drop configuration, drops with a shape parameter in the range of 0.38-0.45 were selected for interfacial tension measurements. Importantly, our data from pendant drops with a shape parameter in this range agrees well with those from sessile drop experiments conducted with this system (Figure 4-3).

4.2.3. Interfacial Tensions of ATPS with Different Phase Compositions

Next we evaluated the sensitivity and accuracy of our approach for measurement of ultralow interfacial tensions using pendant drop experiments with eight different ATPS consisting of varying concentrations of the phase-forming polymers PEG and DEX (Table 4-1 and Table 4-3). The total polymer weight fraction in these systems ranged from 5.621% to 21.404% and resulted in eight different tie-line lengths (Table 4-3), representing the composition of equilibrated aqueous phases (Table 4-1). We conducted ten independent pendant drop experiments with each system. Figure 4-6 presents the results on a

logarithmic scale. The interfacial tensions of these eight ATPS increase from 0.012 mJ/m^2 to 0.381 mJ/m^2. This is consistent with increase in the length of tie-lines resulting from increase in the concentration of one polymer (DEX in systems 1-3 and systems 4-6, and PEG in systems 2 and 5 and systems 3 and 6) while keeping the concentration of the second polymer constant, or by simultaneously increasing the concentrations of both polymers (systems 7 and 8). Systematic measurements of ultralow interfacial tensions of ATPS using ADSA with this accuracy are unprecedented. The slope of the fitted line in Figure 4-6 is 2.1, consistent with reported values in the literature for ATPS with similar phase-forming polymers.

Interestingly and counterintuitively, increasing the total polymer weight fraction does not necessarily result in a higher interfacial tension. For example the total polymer weight fraction of ATPS 3 is 1.028%(w/w) larger than that of ATPS 4; however, it gives a significantly smaller interfacial tension than system 4 (0.042±0.001 mJ/m^2 vs 0.082±0.001 mJ/m^2) because of a shorter tie-line in the phase diagram (Table 4-3). Close scrutiny of data in Table 4-3 shows that interfacial tensions of these eight ATPS are more sensitive to the variations of the PEG phase composition, rather than the total polymer weight fraction. This is due to the asymmetry of the phase diagram (Figure 4-2) where increasing the PEG phase concentration by a given percentage shifts the tie-line diagonally farther away from the critical point compared to a similar increase in the DEX phase concentration. The asymmetry of the binodal curve results from the difference in the molecular weight of phase-forming polymers. Therefore from a practical standpoint, the interfacial tensions of ATPS may be expressed as a function of initial concentrations of phase-forming polymers,

or the tie-line length, or concentrations of final equilibrated (separated) phases, but not the total polymer weight fraction.

Our measurements of ATPS interfacial tensions have been reproducible to an order of 0.001 mJ/m^2. This level of reproducibility is essential for measurements of ultralow interfacial tensions. Although this value is at least an order of magnitude better than those reported before for conventional fluid-liquid systems with drop shape techniques, it may result in a fairly large error for ATPS with very small interfacial tensions. For example for the system 1 with an interfacial tension of 0.012±0.001 mJ/m^2 (Table 4-3), this translates into an error of 8.3% in measurements. This error reduces for other systems with larger interfacial tensions. The smallest error was obtained with the system 4 with an interfacial tension of 0.082±0.001 mJ/m^2, i.e. 1.2% error. From our experience of working with ATPS, one potential source of error may be due to the autonomous dispensing of the DEX phase. The momentum associated with this process may slightly deform the DEX-PEG interface that is very elastic due to an ultralow interfacial tension. In addition, any minor vibrations can augment this effect. Further improving of the precision of measurements remains a question for future studies.

4.3. Summary

We performed systematic measurements of interfacial tensions of eight polymeric aqueous two-phase systems (ATPS) that consisted of different concentrations of phase-forming polymers polyethylene glycol and dextran. Measurements for all systems were conducted using an ADSA methodology. To ensure measuring reproducible interfacial tensions, well-deformity of sessile and pendant drops was evaluated. For pendant drops, a

previously defined formula for the shape parameter was used, whereas for sessile drops, a criterion based on comparing the mean squared error of fitting of a segment of a circle or an ellipse to profiles of drops with different volumes was developed. This resulted in threshold drop volumes to produce well-deformed drops and consistent interfacial tensions. To ensure the reliability of this analysis, both pendant drop and sessile drop techniques were used for measurements with the system containing the lowest concentration of polymers used in this study. The resulting interfacial tensions were less than 0.001mJ/m2 different, indicating the reliability of our data. For all eight two-phase systems, measurements using the pendant drop technique resulted in interfacial tensions ranging from 0.012±0.001 mJ/m^2 to 0.381±0.006 mJ/m^2. On a logarithmic scale, our measured interfacial tensions varied linearly versus the length of tie-lines of ATPS. Our approach will enable reliable and systematic measurements for systems with ultralow interfacial tensions using both sessile drop and pendant drop constellations.

Table 4-1 Polymer weight fractions in stock solutions of PEG and DEX phases, in initial ATPS solution formed with mixing the stock solutions of the two polymers, and in equilibrated PEG-rich and DEX-rich phases. Reprinted with permission from [133]. Copyright (2014) American Chemical Society.

ATPS Number	Phase stock solution		Initial ATPS solution	
	PEG %(w/v)	DEX %(w/v)	PEG %(w/w)	DEX %(w/w)
1	5.000	6.400	2.465	3.156
2	5.000	16.000	2.431	7.779
3	5.000	20.000	2.417	9.667
4	10.000	12.800	4.849	6.207
5	10.000	16.000	4.827	7.723
6	10.000	20.000	4.799	9.598
7	15.000	19.200	7.155	9.159
8	20.000	25.600	9.388	12.016
ATPS Number	DEX-rich phase (bottom phase)		PEG-rich phase (top phase)	
	PEG %(w/v)	DEX %(w/v)	PEG %(w/w)	DEX %(w/w)
1	0.724	7.139	3.158	1.570
2	0.031	12.553	6.012	0.654
3	0.005	14.465	7.030	0.493
4	0.001	16.106	7.489	0.817
5	0.001	17.264	8.375	0.709
6	0.001	19.094	9.369	0.555
7	0.001	23.114	11.494	0.698
8	0.001	29.943	14.857	1.573

Table 4-2 Measured and literature values of interfacial tensions of liquid-liquid and air-liquid systems. *Note: Literature values of interfacial tensions of air-hexadecane and air-water systems were obtained from [134] by interpolation at 24°C. The interfacial tension of water-hexadecane system was obtained from [131] that reports values at 25°C. The slight difference between our measured value and the value reported in this reference is likely due to the temperature difference. Reprinted with permission from [133]. Copyright (2014) American Chemical Society.

System	Measured interfacial tension (mJ/m^2)	Literature interfacial tension (mJ/m^2)*
Air-Hexadecane	27.24±0.01	27.22±0.10
Water-Hexadecane	52.36±0.03	52.24±0.11
Air-Water	72.26±0.13	72.39±0.20

Table 4-3 Eight different ATPS made with different initial weight fraction of PEG and DEX. The total polymer fraction of each ATPS, measured density difference between the two equilibrated (separated) phases, measured lengths of tie-lines, and measured interfacial tensions are given. The ATPS numbers correspond to those in Table 4-1. Reprinted with permission from [133]. Copyright (2014) American Chemical Society.

ATPS	Total polymer %(w/w)	Top phase density (g/cm^3)	Bottom phase density (g/cm^3)
1	5.621	1.008	1.026
2	10.210	1.009	1.047
3	12.084	1.010	1.055
4	11.056	1.012	1.062
5	12.590	1.013	1.067
6	14.397	1.014	1.075
7	16.314	1.018	1.093
8	21.404	1.027	1.125
ATPS	Density difference (g/cm^3)	Tie-line length %(w/w)	Interfacial tension (mJ/m^2)
1	0.018	6.077	0.012±0.001
2	0.038	13.318	0.037±0.002
3	0.045	15.639	0.042±0.001
4	0.050	17.024	0.082±0.001
5	0.054	18.553	0.103±0.006
6	0.061	20.772	0.150±0.006
7	0.075	25.191	0.209±0.006
8	0.098	32.025	0.381±0.006

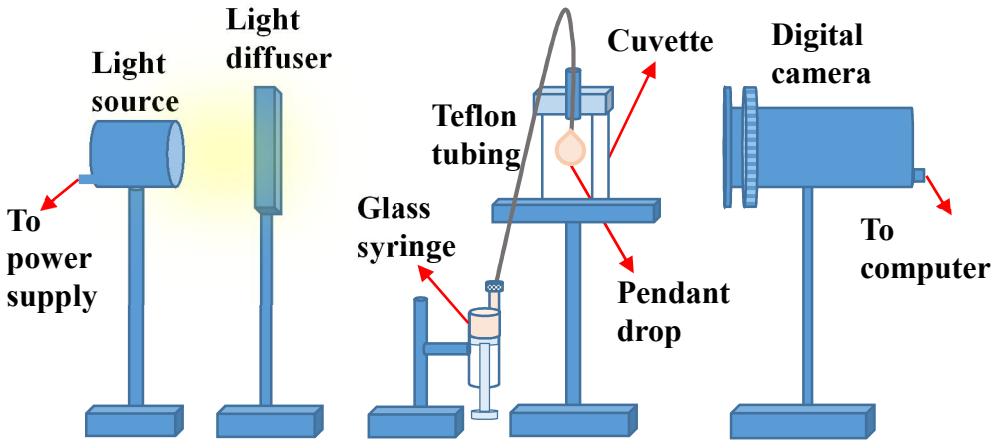

Figure 4-1 Schematic of experimental setup used for formation of sessile and pendant drops and image aquesition. The liquid is loaded into a glass syringe connected to a Teflon tubing. The Teflon tubing is fixed in place veritacally with a plastic stopper mounted in the opening of a cuvette. The liquid is injected through the tubing gently to form a pendant drop inside the cuvette. For interfacial tension measurements, the cuvette is filled with the immersion liquid phase. A light source is used to adjust the image intensity. A digital camera is used to capture drop images. Camera is connected to a computer to save the captured images. The setup is assembled on a vibration isolating table. To form a sessile drop, the Teflon tubing is lowered close to the cuvette bottom and a drop is dispensed on the cuvette bottom surface. Reprinted with permission from [133]. Copyright (2014) American Chemical Society.

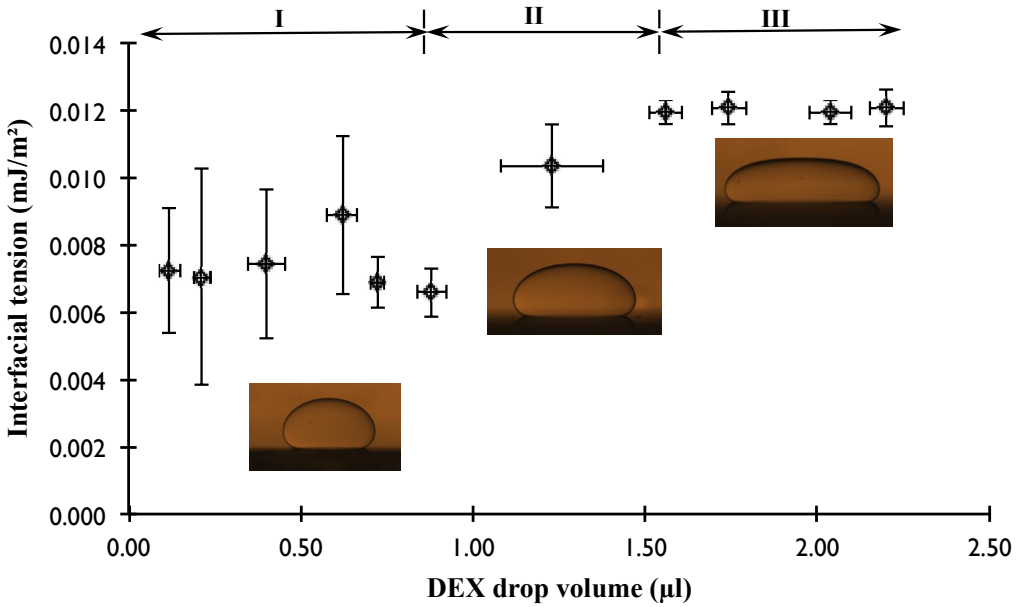

Figure 4-2 Interfacial tension of system number 1 of Table 4-1 is measured from sessile drop experiments and shown versus the volume of the DEX phase drop. For this system, sessile drops become well-deformed at volumes larger than 1.6 µl and result in consistent interfacial tensions. Error bars represent 95% confidence limits. Reprinted with permission from [133]. Copyright (2014) American Chemical Society.

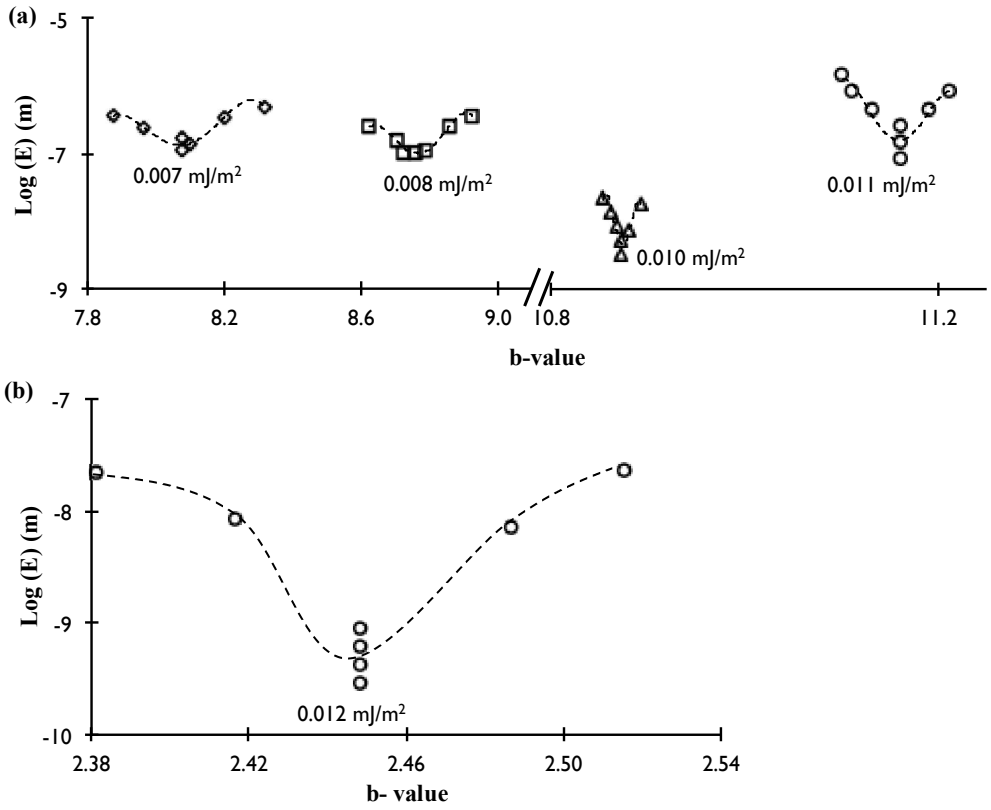

Figure 4-3 Logarithm of the error of Laplacian curve fitting is shown versus the b-value for (a) a non well-deformed sessile drop (0.42 µl) and (b) a well-deformed sessile drop (2.04 µl). For the non well-deformed drop, ADSA may return different interfacial tensions that correspond to local minima of the error function, if a local minimum is smaller than a user-defined threshold. With a 10^{-6} threshold error value, ADSA generates different interfacial tension values for the small, non-well deformed drop (a) but a unique interfacial tension for the well-deformed drop (b). Note that the scales of the b-value axis on the two graphs are different. Reprinted with permission from [133]. Copyright (2014) American Chemical Society.

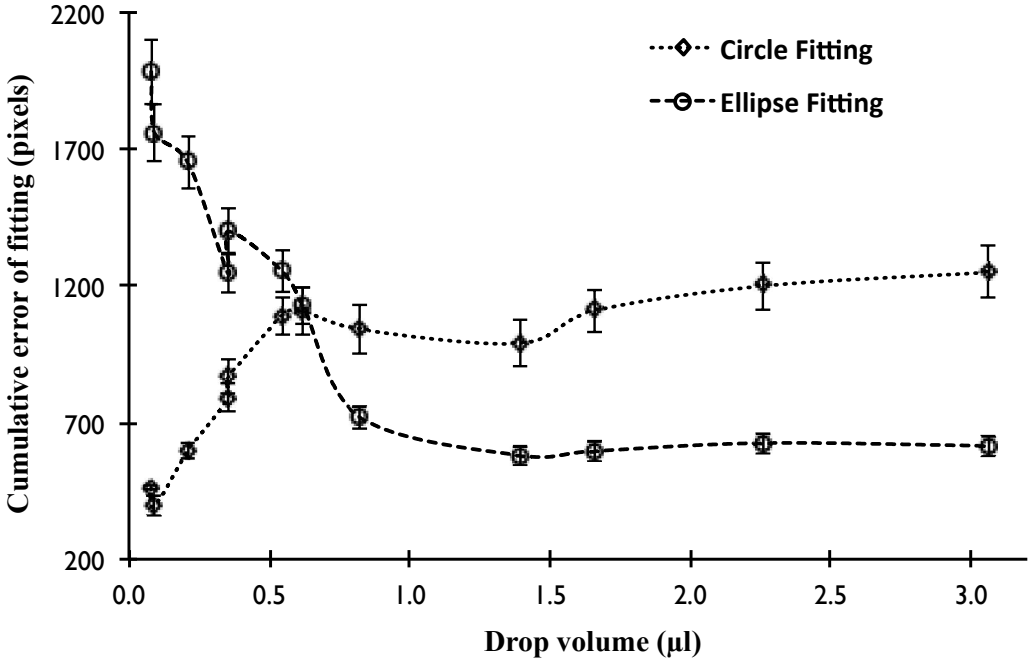

Figure 4-4 Cumulative error of fitting segment of a circle and an ellipse to sessile drops of ATPS 1 from Table 4-1 is shown versus drop volume. Cumulative error represents the sum of root mean square of normal distances between pixels on the drop profile and corresponding points from fitting a segment of a circle or an ellipse. Standard deviations represent 95% confidence limits. Reprinted with permission from [133]. Copyright (2014) American Chemical Society.

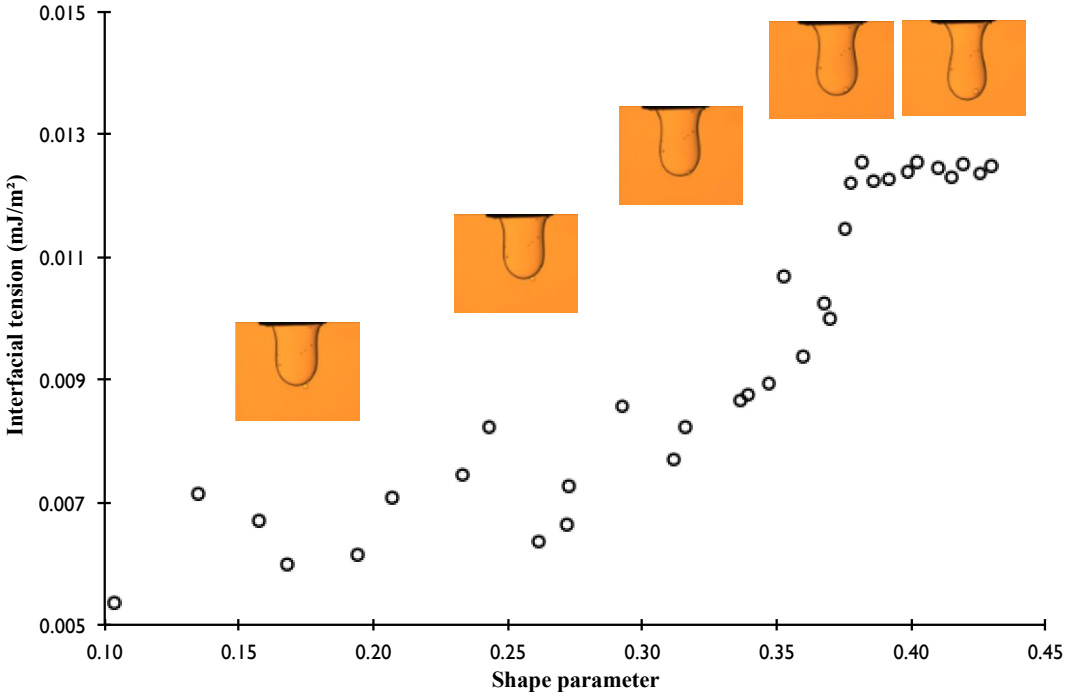

Figure 4-5 Variations of interfacial tension measured from a pendant drop experiment with the system 1 from Table 4-1 are shown versus shape parameter. Measured interfacial tensions show a plateau at 0.012±0.001 mJ/m^2 corresponding to a range of 0.38-0.45 for the shape parameter. Reprinted with permission from [133]. Copyright (2014) American Chemical Society.

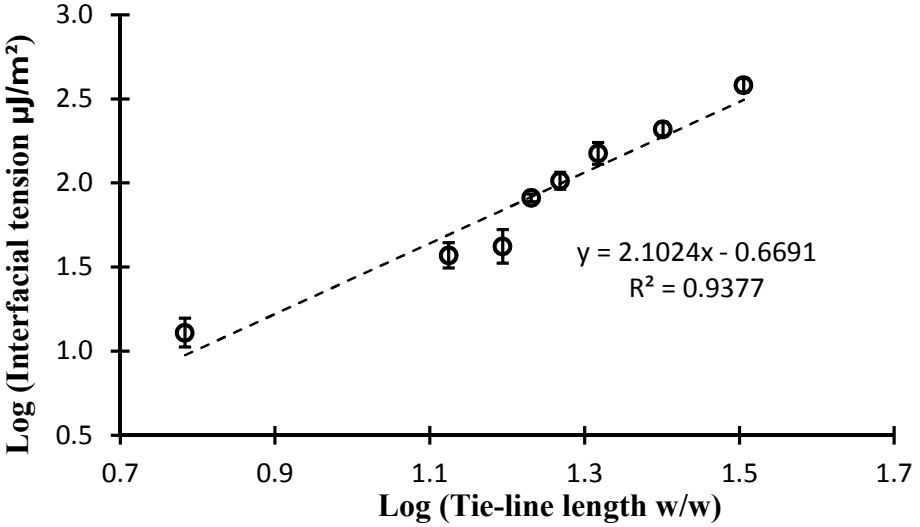

Figure 4-6 Measured interfacial tensions for eight different ATPS (listed in Table 4-3) vary linearly with the tie-line length on a logarithmic scale. R^2 is the goodness-of-fit parameter. Reprinted with permission from [133]. Copyright (2014) American Chemical Society.

CHAPTER V

PARTITION OF CELLS IN AQUEOUS TWO-PHASE SYSTEMS

Partition of cells in ATPS has recently enabled novel cell patterning and printing approaches for controlling cellular microenvironments and tissue engineering applications[135], [136], [137], [138]. These methods primarily use polyethylene glycol (PEG) and dextran (DEX) as phase-forming polymers and rely on selective partition of cells to one of the aqueous phases or the interface between them[139], [140]. Dispensing a drop of the aqueous DEX phase containing stem cells onto a layer of adhered stromal cells immersed in the aqueous PEG phase created co-cultures that led to differentiation of stem cells to neurons[135]. Complete exclusion of cancer cells from aqueous DEX phase drops printed on a culture plate, or in other words complete partition of cells to the immersion PEG phase, generated a monolayer of cells containing a circular cell-excluded gap that served as the migration niche for adhered cells[138], [137], [136]. Selective partition of cells to the interface of two aqueous phases allowed a straightforward method of creating skin-like constructs[82]. In all these applications, effective partition of cells to a desired phase of the ATPS or the interface was critical.

It is substantiated that partition of cells in polymeric ATPS is influenced by environmental factors including temperature and pH of media, polymer concentration, electrostatic potential of media, interfacial tension, and polymer molecular weight[86]. In this chapter, we present a combined experimental and theoretical study on the effect of

interfacial tension of polymeric ATPS on partition of the cancer cells to forming phases. Experimentally, we determine the number of cells partitioned to the top phase, the bottom phase, and their interface of four different biphasic systems and show variation of cell partition with measured interfacial tensions. Theoretically, we develop a thermodynamic model to predict the partition behavior of cells in an ATPS through free energy calculations. We show that the result from our modeling corroborates with the experimental results in predicting partition of cells in ATPS.

5.1. Materials and Methods

In this section the preparation of ATPS with PEG 35k – DEX 500k, PEG 8k – DEX 500k, and PEG 35k – DEX 40k and preparation of cell suspension for partition experiments are explained. In addition, the experimental procedure of calculating the number of cells partitioned to forming phases of ATPS is presented. Finally, measuring contact angles of ATPS on a monolayer of cells is explained.

5.1.1. Preparation of Aqueous Two-Phase Systems

Polyethylene glycol (PEG) with a molecular weight of 35 kDa (Sigma-Aldrich) and dextran (DEX) with a molecular weight of 500 kDa (Pharmacosmos) were used for ATPS formation. Four different sets of two-phase systems were formed using 5.0% PEG – 6.4% DEX, 10.0% PEG – 12.8% DEX, 15.0% PEG – 19.2% DEX, and 25.0% PEG – 25.6% DEX. Concentrations of aqueous PEG and DEX solutions were calculated in %(w/v). Both polymers were dissolved in complete growth medium with a composition shown below.

To facilitate dissolution of polymers, solutions were kept in a 37°C water bath for about 60 minutes while vortexing them for 2 min every 10 min.

5.1.2. Preparation of Cell Suspension

A431.H9 skin cancer cells were kindly provided by Dr. Mitchel Ho (NIH). Cells were cultured in a complete growth medium composed of 88% Dulbecco's Modified Eagle's Medium (DMEM, Sigma), 10% fetal bovine serum (FBS, Sigma), 1% glutamine (Life Technologies), and 1% antibiotic (Life Technologies). T75 culture flasks were kept in a humidified incubator with 5% CO_2 at 37°C to allow cells form a monolayer of 80-90% confluent. Cells were dislodged with 2 mL of trypsin for 2 minutes. After adding 4 mL of growth medium to neutralize trypsin, cells were harvested and the suspension was centrifuged down at 1000 rpm for 5 min. The supernatant was removed and the cell pellet was resuspended in 1 mL of the medium. The number of cells was counted using a hemocytometer.

5.1.3. Cell Partition in ATPS

Cell suspensions were made by mixing ~6×10^6 cells with two-phase solutions consisting of 500 μL from each of PEG and DEX phases. All four sets of two-phase systems with different PEG and DEX concentrations were separately used. The conical tube was maintained vertically in an incubator with 5% CO_2 in 37°C until two clear, separate phases were formed. Volumes of top (V_{Top}) and bottom (V_{Bot}) equilibrated phases were measured using graduations on the conical tube. Four samples from top and bottom phases and the interface were separately loaded onto a hemocytometer. The number of cells

in each sample was counted and an average was calculated. The total number of cells partitioned to each phase was calculated by multiplying the average number of counted cells in that phase, volume of the equilibrated phase, a constant number 10^4, and a dilution factor. The number of cells partitioned to the interface was also calculated by subtracting the number of cells partitioned to top and bottom phase from the total number of cells used for the experiment.

5.1.4. Interfacial Tension Measurements

The interfacial tension between equilibrated top and bottom phases of each of four two-phase systems was measured using an axisymmetric drop shape analysis (ADSA) explained in chapter IV. For each two-phase system, an average interfacial tension was determined from five measurements.

5.1.5. Contact Angle Measurements

An 18×18 mm^2 microscopic glass slide was UV sterilized for 30 min. Each glass slide was placed in 35 mm Petri dish containing 4 mL of 0.5% aqueous gelatin solution (Sigma-Aldrich). After 3 hrs of incubation at 37°C and 5% CO2, the gelatin solution was removed and 4 mL of cell suspension containing 3×10^4 cancer cells was added to the dish. To ensure formation of a uniform cell monolayer, each glass slide was incubated for 36 hrs to allow cells spread and grow. After removing the culture medium, the glass slide containing the cell monolayer was washed with PBS three times and transferred into a glass cell (White Bear Photonics) filled with pre-equilibrated top phase from the desired two-phase system. A 0.7 μL drop of pre-equilibrated bottom phase of the same two-phase

system was gently dispensed onto the slide using a pipette. The glass cell was incubated for 60 min at 37°C and 5% CO2. A camera (JAI Ltd., CB-200GE)-lens (LEICA, Z16 APO) unit assembled on an optical table was used to capture the image of the drop at a 9.2× magnification. Contact angles were measured using an automated polynomial fitting technique explained in chapter III. Each condition had five replicates.

5.1.6. Density Measurements

Densities of equilibrated phases from each two-phase system were measured using a density meter (Mettler Toledo, DA-100M) accurate to 0.001 g/cm^3 (also explained in chapter II).

5.1.7. Spheroid formation assay

Aqueous PEG phase solutions were prepared in the complete growth medium at 5.0%, 10.0%, 15.0%, and 20.0% (w/v) and loaded into wells of a round-bottom, non cell-adherent 96-well plate. Aqueous DEX phase solutions were prepared at 6.4%, 12.8%, 19.2% DEX, and 25.6% (w/v). A suspension of A431.H9 cells was prepared at a density of 33×10^5 cells/μL within the DEX phase solutions. A 0.3 μL drop of the resulting suspension was dispensed into each well. Plates were incubated for 24 hrs and spheroid formation was evaluated by phase contrast imaging of wells. Spheroid formation is presented comprehensively in chapter VI.

5.1.8. Statistical Analysis

Statistical analysis is performed using Matlab. Results are presented as mean ± standard deviation. Differences between means are determined using one-way ANOVA. P-value smaller than 0.05 is considered as statistically significantly different.

5.2. Results and Discussion

In this section, the number of cells partitioned in each phase of an ATPS is measured experimentally and presented versus interfacial tension. The effect of interfacial tension on cell distribution is discussed.

5.2.1. Interfacial Tensions of ATPS

After equilibration of each two-phase system, we separated top and bottom phases and used a Pendant drop method, as explained in chapter IV, to measure the interfacial tension between an aqueous DEX phase drop immersed in the aqueous PEG phase. Measurements were done with all four two-phase solutions made with increasing concentrations of PEG and DEX. In addition, concentrations of PEG and DEX in equilibrated phases of each two-phase solution were determined from the phase diagram of the ATPS shown in Chapter II. Then, a tie-line length (TLL) was calculated for each system as

$$TLL = \sqrt{\left(C_{PEG,T} - C_{PEG,B}\right)^2 + \left(C_{DEX,T} - C_{DEX,B}\right)^2} \qquad (5\text{-}1)$$

Here, $C_{PEG,T}$ and $C_{PEG,B}$ represent PEG concentration in top and bottom phases and $C_{DEX,T}$ and $C_{DEX,B}$ denote DEX concentrations in top and bottom phases, respectively. Figure 5-1 shows interfacial tensions of all four systems versus TLL. Consistent with previous reports, interfacial tension increases linearly on a logarithmic scale with TLL.

5.2.2. Partition of Cells in ATPS

We conducted systematic cell partition experiments in two-phase solutions of four different interfacial tensions. A defined number of A431.H9 cells (6×10^3 cells/μL) was included in each of the four systems (Figure 5-2a). After two immiscible phases formed, the number of cells in samples from each phase was counted using a hemocytometer (Figure 5-2b). A partition coefficient was defined as the number of cells in the bottom phase divided by the total number of cells included. The two-phase system with the smallest interfacial tension of 30 μJ/m^2 gave a large partition coefficient of 88±5% (Figure 5-2c). The remaining 12% of cells were primarily recovered from the top phase samples. Increase in the interfacial tension to 93 μJ/m^2 in the second system significantly diminished cell partition to the bottom phase, resulting in a decrease of the partition coefficient to 34±3%. This was accompanied by a large increase in the number of cells partitioned to the interface from 2±1% in the first system to 47±5% in the second system. The number of cells recovered from the top phase also showed a slight increase to 20±6% in this system. Further increase in the interfacial tension up to 440 μJ/m^2 reduced the partition coefficient to 24±4% and caused a moderate increase in cell partition to the top phase to 35±3%, whereas cell partition to the interface remained statistically unaltered.

We note that the selected cell density for partition experiments was based on preliminary experiments and ensured cells would not clump into large aggregates. At a single cell level, the effect of gravity is negligible and several orders of magnitude smaller than the interfacial forces, ruling out the role of gravity on distribution of cells in ATPS. Overall, this study establishes the influence of ultralow interfacial tensions of polymeric aqueous biphasic systems on partition of cells between the two phases and their interface when important parameters such as molecular weight of polymers, temperature, and pH of the separation medium are kept fixed. With the systems studied here, it appears that interfacial tension plays a major role on cell partition only at very small values and further increase does not affect the partition coefficient significantly. Other factors may have a more major role on the distribution of cells in ATPS at larger interfacial tension values.

5.2.3. Spheroid Formation in ATPS

To demonstrate the validity of the observations above, we performed a spheroid formation assay using all four systems made with the PEG 35k – DEX 500k ATPS. Spheroids are three-dimensional clusters of cancer cells that mimic avascular solid tumors and present a relevant cellular model for cancer research. A suspension of A431.H9 cells was generated and a drop of this suspension was dispensed into a microwell containing the PEG phase solution. Due to its higher density, the drop settled at the bottom of the microwell while remaining phase separated from the immersion PEG phase. We evaluated spheroid formation with all four two-phase solutions after 24 hrs. Figure 5-3a shows that the first system produced a compact spheroid within the DEX phase drop. By increase in the interfacial tension for other systems, cells only formed several small, loose aggregates

close to the interface of the drop (Figure 5-3b). This test validates that with the system of the smallest interfacial tension studied here, cells primarily remain in the DEX phase drop to form a spheroid. However, the propensity of cells to partition to the interface and top phase in the other three systems disrupts self-assembly of cells into a single spheroid. From a practical standpoint, these data suggest using ATPS with low interfacial tensions of ~30 μJ/m^2 to generate cancer cell spheroids of consistent size (Figure 5-3c).

5.2.4. Theoretical Model of Cell Partition in ATPS

To understand the effect of interfacial tension on partition of cells in ATPS, we developed a theoretical model to determine potential energy of displacement of cells between the two aqueous phases and their interface (Figure 5-4a). Each cell was considered as a spherical particle of 1 μm radius. Initially, the particle was assumed to locate in an arbitrary position Z_0 in the bottom phase (1). Displacement of the particle toward the interface (2) and the top phase (3) was traced using a vector Z perpendicular to the interface.

Changes in the potential energy associated with displacement (floatation) of the particle from the initial position (Z_0) in the bottom phase to a final arbitrary position (Z) is given by

$$\Delta U(Z) = \gamma_{l_1 l_2}\left(A_{l_1 l_2}(Z) - A_0\right) + \gamma_{sl_2} A_{sl_2}(Z) + \gamma_{sl1}\left(A_{sl_1}(Z) - A_p\right) \quad (5\text{-}2)$$

where $\gamma_{l_1 l_2}$ represents the interfacial tension between the two liquid phases, γ_{sl_1} is the cell-bottom phase interfacial tension, and γ_{sl_2} denotes the cell-top phase interfacial tension. $A_{l_1 l_2}(Z)$ represents the area of liquid – liquid interface when the particle is at a position $-R < Z < R$, A_0 is the total area of interface with a length L and width W, A_{sl_1} and

A_{sl_2} represent the areas of particle in contact with bottom and top phases, respectively, and A_p denotes surface area of the particle. Using these definitions, we can write

$$A_{sl_2}(Z) + A_{sl_1}(Z) = A_p = 4\pi R^2 \tag{5-3}$$

$$A_{l_1l_2}(Z) + A^p_{l_1l_2}(Z) = A_0 = LW \tag{5-4}$$

Here, $A^p_{l_1l_2}$ denotes the area of the interface between two liquid phases occupied by the particle. Assuming the validity of Young's equation

$$\gamma_{l_1l_2} Cos\theta_c = \gamma_{sl_2} - \gamma_{sl_1} \tag{5-5}$$

and considering equations 5-3 and 5-4, the potential energy equation 5-2 reduces to

$$\Delta U(Z) = \begin{cases} 0, & Z < -R \\ \gamma_{l_1l_2}\left[Cos\theta_c A_{sl_2}(Z) - A^p_{l_1l_2}\right], & -R < Z < R \\ \gamma_{l_1l_2} Cos\theta_c A_P, & Z > R \end{cases} \tag{5-6}$$

To evaluate the potential energy changes of particle displacement from Z_0 to Z, the interfacial tension between the two aqueous phases (Figure 5-1) and the contact angle formed on the surface of the particle at the interface of the two phases (Figure 5-4b) is required. We developed an alternative method to determination of contact angles at the interface of the two aqueous phases and a single cell shown in the Figure 5-4b schematics. A monolayer of A431.H9 cells was immersed in the aqueous PEG phase. Then a drop of the aqueous DEX phase was dispensed on cells. A typical sessile drop of the DEX phase on cells immersed in the PEG phase is shown in Figure 5-5a. To estimate contact angles of ATPS drops, we first captured side view images of ATPS drops (Figure 5-5b). Then we

used an automated polynomial fitting technique that applies a standard Canny edge detection method to extract the drop profile and fit a polynomial to each half of the drop profile (Figure 5-5c), as explain in detail in Chapter III. Contact angle was computed as the tangent to the polynomial at the surface. The contact angle of each drop was determined as the average of right and left contact angles. This process was repeated for five drops to determine an average contact angle with each two-phase system on cells (Figure 5-5d). Overall, contact angles increase correlates with the increase in the interfacial tension. Interestingly however, despite a significant difference in the interfacial tensions of the last three systems, measured contact angles only show a modest increase.

Next, changes in free energy for cell displacement in each of the two-phase solutions (ΔU) were calculated from equation 5-6 and the results were plotted versus the position vector Z in Figure 5-6. With the first system that has the smallest interfacial tension of 30 $\mu J/m^2$, the minimum energy is associated with the particle in the bottom phase. Displacing the particle from its initial position to the interface or the top phase will increase the energy. Therefore, the particle will tend to partition to the bottom phase that is energetically favored. Experimentally, cells primarily partitioned to the bottom phase of this two-phase solution and showed a large partition coefficient of 88±5% (Figure 5-2), consistent with the modeling prediction. For the system with an interfacial tension of 93 $\mu J/m^2$, the minimum potential energy corresponds to the interface and toward the bottom phase, increasing the propensity of particle entrapment at the interface. This agrees with the experimental results that show a significant increase in the partition of cells to the interface in this two-phase solution (Figure 5-2), and a decrease of the partition coefficient to 34±3%. With the two systems with larger interfacial tensions of 226 $\mu J/m^2$ and 440

$\mu J/m^2$, the minimum potential energy happened at the interface of the two phases. Experimentally, the partition coefficient in these systems dropped to only ~24%. However, the number of cells entrapped at the interface remains more or less constant but more cells partition to the top phase. This observation cannot be explained with our simple theoretical model and is likely due to effects not considered in this model. Nevertheless, this simple thermodynamic model provides a fundamental understanding of interfacial tension effect on cell partition in aqueous two-phase systems.

5.3. Summary

We presented an experimental study of partition of cells in polymeric aqueous two-phase systems (ATPS) and demonstrated that interfacial tension between the equilibrated phases plays a major role on distribution of cells between the two phases and their interface. With polyethylene glycol and dextran of specific properties used as phase-forming polymers, an interfacial tension of 30 $\mu J/m^2$ resulted in the partition of cells primarily to the bottom phase. Increasing the interfacial tension through systematic increase in the concentration of polymers shifted cells more toward the interface and the top phase. A validation study was conducted to demonstrate that a very small interfacial tension is crucial for successful formation of a compact cellular spheroid in the bottom phase drop immersed in the top phase solution. To fundamentally understand this phenomenon, we developed a thermodynamic model to predict free energy changes associated with displacement of particles in a two-phase system. This theoretical model suggested that in the system with the smallest interfacial tension of 30 $\mu J/m^2$, the free energy is minimum when the particle locates in the bottom phase. By increase in the interfacial tension, there

is a greater propensity for the particle to partition to the interface, corroborating with our experimental observations. Future developments of this experimental and theoretical study will enable drawing a more complete picture of cell partition in ATPS by considering the influence of other important factors.

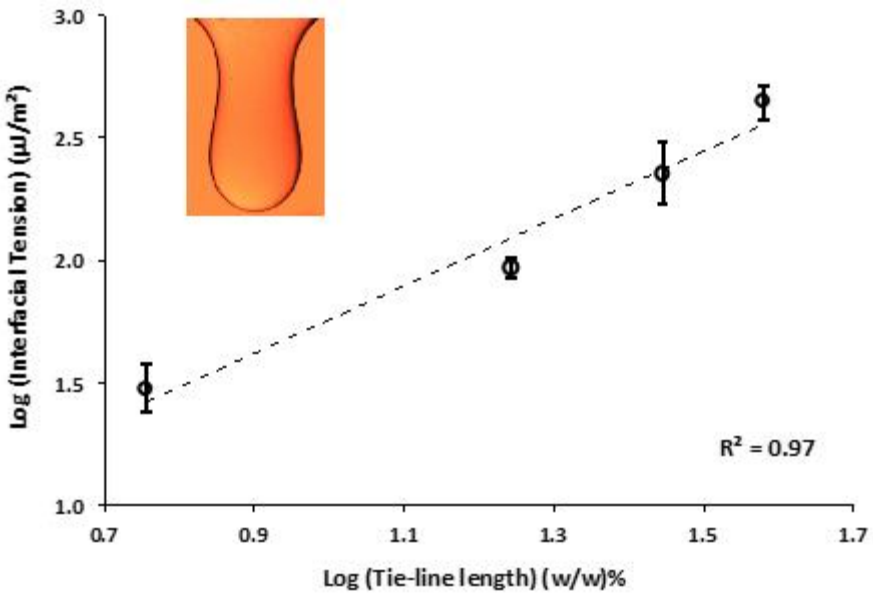

Figure 5-1 Interfacial tensions of four two-phase systems made with different concentrations of PEG and DEX is shown against tie-line length on a logarithmic (base 10) scale. Dashed line is a fitted line to data and R^2 shows the goodness of the fit. The inset image shows a Pendant drop experiment for interfacial measurement with the 10.0% PEG – 12.8% DEX system.

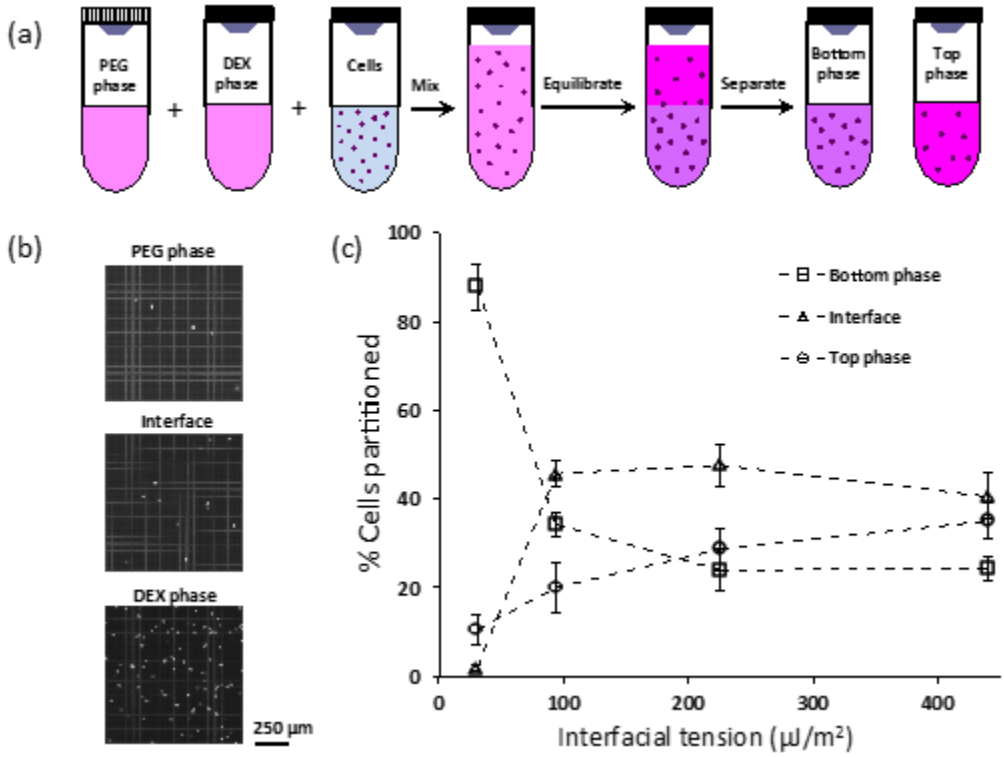

Figure 5-2 (a) Schematic of cell partition experiment with aqueous two-phase systems, (b) images of cells recovered from top phase, interface, and bottom phase of the 5.0% PEG – 6.4% DEX two-phase system and loaded on a hemocytometer for counting, and (c) percent of cells partitioned to each of the two bulk phases and their interface in four two-phase systems is shown versus interfacial tension. Dashed lines are only used to connect data points.

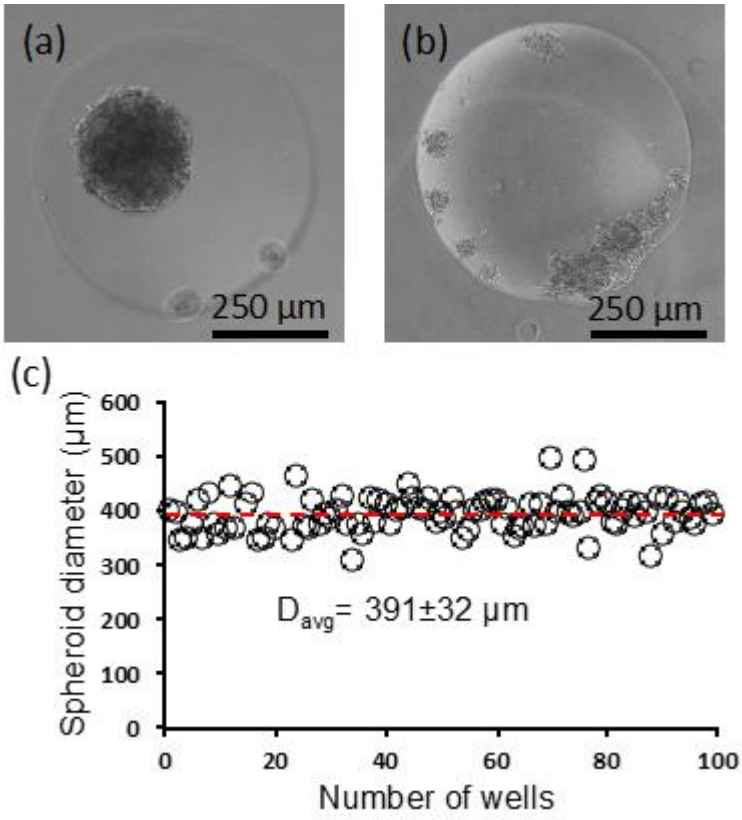

Figure 5-3 Spheroid formation assay performed with two-phase systems made with (a) 5.0% PEG – 6.4% DEX and (b) 10.0% PEG – 12.8% DEX. (c) Reproducibility of spheroid formation using the 5.0% PEG – 6.4% DEX system in a 96-well plate. The dashed line shows the average diameter of spheroids.

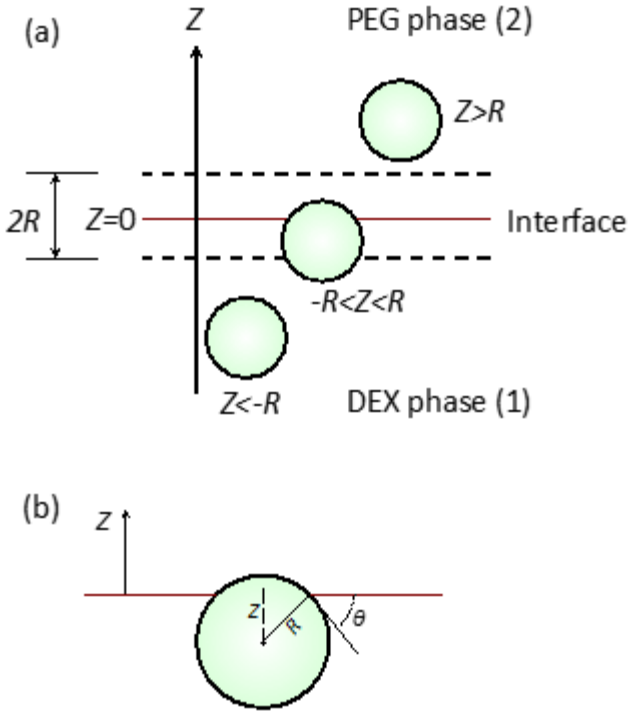

Figure 5-4 (a) Schematics of model for particle displacement in two-phase systems and (b) contact angle,θ, formed between the particle surface at the interface of two aqueous phases.

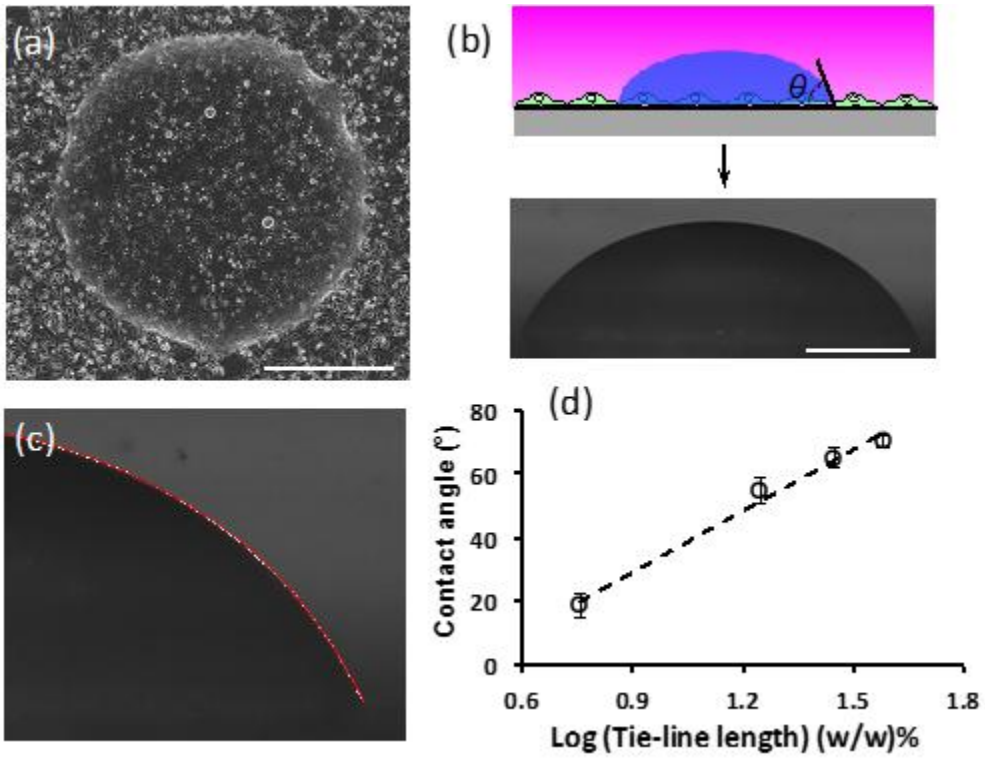

Figure 5-5 (a) Top view of a sessile drop image of ATPS formed on a confluent monolayer of cells, (b) schematic and side view image of a sessile drop of ATPS on a layer of cells, (c) a third order polynomial fitted to the right side of the drop in panel (b) shown by a red line, and (d) contact angles measured with two-phase systems on cells increase with the total weight fraction of polymers in two-phase systems. Scale bar is 500 μm.

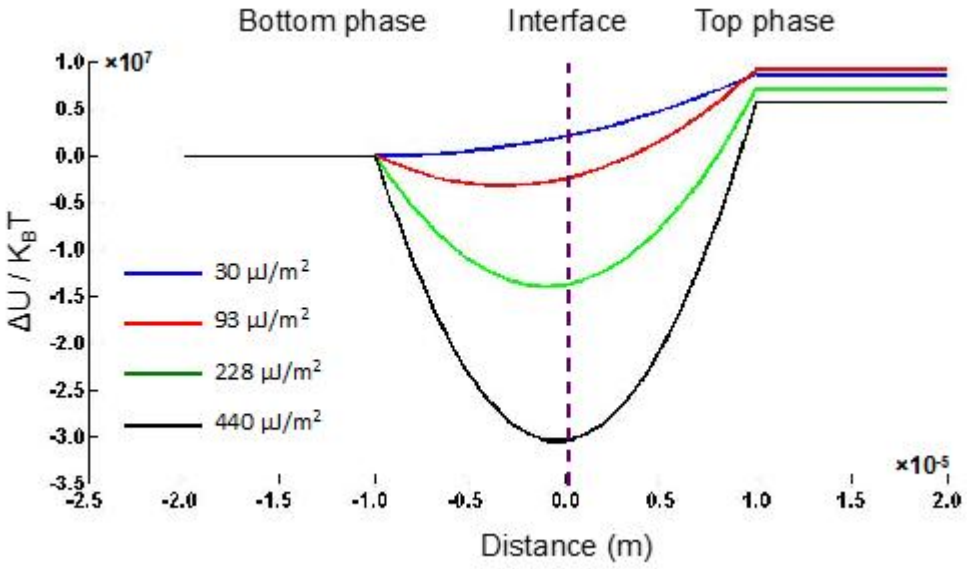

Figure 5-6 Variations in the free energy associated with displacing a particle of 1 μm radius in four two-phase systems. Colors represent these four systems of different interfacial tensions shown in the legend. Free energy is scaled to KBT= 4.142×10-21 J at T= 300 K. The dashed line shows the location of the interface.

CHAPTER VI

AQUEOUS TWO-PHASE SYSTEM 3D CELL CULTURE TECHNOLOGY

Three-dimensional (3D) cell cultures provide an important tool for tissue engineering and drug testing and delivery applications. In recent years, there has been a greater recognition of the need for 3D cultures of cancer cells in various areas of cancer research including oncology drug discovery[141]. This is motivated by a high failure rate of compounds that show efficacy against monolayer cultures but fail to reproduce the same response in animal models. Unlike monolayer of cells, 3D cultures of cancer cells known as cancer cell spheroids reproduce key properties of tumors in vivo and thus, offer a physiologically relevant in vitro tumor model[142], [143], [34]. Nonetheless, the use of traditional 3D cultures is hindered by difficulty of implementing, handling, maintaining, treating with biological reagents, and analyzing of cellular responses[144],[34]. The traditional liquid overlay method prevents cell adhesion to the surface and retains cells in suspension to form random-sized spheroids. Rotary vessel and spinner flask technologies continuously spin cells and maintain them in suspension to mass produce spheroids; however applied shear forces, non-uniform size, and the need for harvesting of resulting spheroids remain key limitations[145], [146]. Traditional and new techniques based on hanging drops approach utilize gravity to induce formation of spheroids of controlled size at the apex of drops hanging from the culture plate; however addition of media and reagents is challenging, media evaporation is a major problem, plates are difficult to handle during

culture as drops may merge or fall off the plate, and downstream analysis of cellular response to added reagents requires transfer of spheroids into a standard microwell plate[147], [17], [148]. Platforms based on microfabrication allow culturing uniform size spheroids, but the depth of micro-channels/wells/spheres (often < 100-200 μm) limits the size of spheroids, which also remain inaccessible for downstream analysis with commercially available screening instruments such as plate readers[149], [150], [151]. In addition, spheroids cannot be individually addressed with a compound of interest, making each device only useful for testing one condition, i.e., a single concentration of a compound. As such, existing techniques are limited for mass producing spheroids of uniform, pre-defined size that are easy to maintain, individually treat with biological reagents, and biochemically analyze with available robotic tools[147]. The new technique presented in this thesis addresses this need and enables high throughput generation of spheroids in standard microwell plates with commercial robotics and allows analysis of cellular response to biological reagents without a need to transfer or retrieve spheroids.

We have developed a novel approach for convenient 3D culture of cancer cells and high throughput production of consistent-size cellular spheroids in standard 96-well plates[143]. Our approach is based on the use of a polymeric aqueous two-phase system (ATPS) to confine cells within a nanoliter-volume aqueous drop immersed within a second, immersion aqueous phase to facilitate aggregation of cells into a spheroid. The resulting spheroids present a tool to evaluate the effectiveness of therapeutic compounds against cancer cells under conditions more physiologic than standard monolayer cultures. This microtechnology eliminates shortcomings of existing techniques by offering full

compatibility with robotic tools and screening instruments to allow straightforward culture, maintenance, drug treatment, and biochemical analysis of cellular spheroids in situ.

6.1. Materials and Methods

In this section, preparation of ATPS with pairs of six different polymers and spheroid formation with the resulting ATPS are presented.

6.1.1. Aqueous Two-Phase System (ATPS) Formation

We evaluated the formation of an aqueous two-phase system (ATPS) using pairs of the following polymers at a wide range of concentrations: polyethylene glycol, Mw: 35,000 (PEG35k, Sigma-Aldrich), polyethylene glycol, Mw: 8,000 (PEG8k, Sigma-Aldrich), dextran Mw: 500,000 (DEX500k, Pharmacosmos), polyvinylpyrrolidone, Mw: 40,000 (PVP40k, Sigma-Aldrich), polyvinyl alcohol, Mw: 23,000 (PVA23k, Sigma-Aldrich), and polyacrylamide, Mw: 10,000 (PAAM10k, Sigma-Aldrich). All polymers were in powder form except for PAAM10k that was received as a 50 wt.% aqueous solution. Each polymer was dissolved in ultrapure water at a solubility recommended by the manufacturer and subsequently diluted in water to smaller concentrations. To facilitate dissolving of polymers, solutions were vortexed and then kept in a 37°C water bath for 2 hrs. Stock polymer solutions were stored at 4°C until use.

Equal volumes of pairs of different concentrations from each two polymers were mixed in microcentrifuge tubes to a total volume of 1 ml. Tubes were kept vertical in a rack at room temperature to allow polymer solutions equilibrate overnight. Formation of

an ATPS was visually confirmed if an interface separating a lighter top phase and a denser bottom phase was present.

6.1.2. Cell Culture

A431.H9 skin cancer cells were kindly provided by Dr. Mitchel Ho (Center for Cancer Research, NIH, Bethesda, MD) and maintained in complete growth medium composed of Dulbecco's Modified Eagle Medium (DMEM, Sigma-Aldrich), 10% Fetal Bovine Serum (FBS, Sigma-Aldrich), 1% glutamine (Life Technologies), and 1% antibiotic (Life Technologies). Every 10 passage, cells were treated with 700 µg/ml of G418 (Sigma-Aldrich). Cells were cultured in T75 flasks at 37°C and 5% CO_2 until a monolayer of 80-90% confluent formed. Cells were harvested using 2-3 ml of trypsin (Life Technologies), which was neutralized with 6 ml of complete growth medium. The cell suspension was centrifuged at 1000 rpm for 5 min. Cells were resuspended in 1 ml of medium and counted with a hemocytometer.

6.1.3. Spheroid Formation with Different ATPS

Those pairs of concentrations from each two polymers that formed an ATPS were subsequently tested for spheroid formation. Polymer solutions were prepared with the growth medium. 80 µl of the lighter phase polymer solution (immersion phase) was loaded into wells of a 96 non-adherent round bottom well plate (Nunc). The polymer solution of the denser phase was thoroughly mixed with A431.H9 cells at a density of 25,000 cells/µl and 300 nl of this suspension was dispensed into each well using a robotic liquid handler (SRT Bravo, Agilent Technologies). The plate was incubated for 48 hrs. Then wells were

imaged with an inverted fluorescent microscope (AxioObserver A1, Zeiss) equipped with a high resolution camera to evaluate spheroid formation.

6.1.4. Spheroid Culture

Aqueous solutions of 5.0%(w/w) PEG and 12.8%(w/w) DEX were prepared in the growth medium. A pre-defined number of A431.H9 cells suspended in growth medium was mixed thoroughly with an equal volume of the 12.8% DEX solution and loaded into one column of 384-well plate, labeled as the source plate. Each well of a non-adherent, round-bottom 96-well plate, labeled as the destination plate, was loaded with 50 µl of 5.0% PEG phase. Both plates were placed on the working surface of the robotic liquid handler. The tip magazine of the liquid handler loaded 8 pipette tips of 0.1-10 µl volume (Fluotics) onto one column of the pipetting head, aspirated a defined volume of cell suspension in DEX phase (e.g., 300 nl) into each tip, and dispensed it into each well of the destination plate 0.1 mm away from the well surface. This was followed by dispensing 600 nl pre-aspirated air to completely empty the tip and form a drop at the bottom of the well. The destination plate was incubated at 37°C and 5% CO_2. Spheroids were imaged every other day and medium was refreshed.

6.1.5. Statistical Analysis

Statistical analysis is performed using Matlab. Results are presented as mean ± standard deviation. Differences between means are determined using one-way ANOVA. P-value smaller than 0.05 is considered as statistically significantly different.

6.2. Results and Discussion

In this section, spheroid formation with ATPS made with different pairs of polymers is presented. Control over the initial size of spheroids and adapting this approach to a high throughput format is explained. Conditions guaranteeing formation of a single spheroid within each drop and growth of spheroids over incubation time is presented next.

6.2.1. Spheroid Formation

We initially selected a polymeric ATPS comprising of DEX (Mw: 500k) and PEG (Mw: 35k) as the phase-forming polymers. Dispensing of nanoliter volumes of the denser aqueous DEX phase within the aqueous PEG phase used as immersion medium results in a round drop that remains completely stable (Figure 6-1a). Based on our study in Chapter V, we selected a system with phase concentrations of 5.0%(w/w) PEG and 6.4%(w/w) DEX for spheroid assay since the resulting two-phase solution has a very small interfacial tension of 30 $\mu J/m^2$, favoring partition of cells to the DEX phase. During incubation, cells remained confined within the drop and formed a spheroid, without any external stimuli (Figure 6-1b). The spheroid presents a normal morphology with a darker core, brighter periphery, and a clear boundary. Over 7 days of incubation, spheroids form a compact mass of cells resembling the morphology of solid tumors (Figure 6-1c). Importantly, we confirmed that this technique accommodates spheroids with as few as 1×10^3 cells and as many as 1×10^5 cells to produce A431.H9 spheroids with diameters of 125±20 μm to 900±72 μm, respectively. This also made it possible to pre-define the size of spheroids from a desired cell density within this range (Figure 6-2). We confirmed the utility of this

approach for spheroid formation by a different cancer cell line, MDA-MB-157 breast cancer cells.

6.2.2. Compatibility of the 3D Cell Culture Technology

We evaluated the feasibility of generating spheroids with different combinations of aqueous solutions of a panel of six polymers. The criteria for selecting these polymers were compatibility with cell culture and forming an ATPS, as reported previously. Aqueous solutions of each polymer were prepared at four concentrations of 5%, 10%, 15%, and 20%. Solutions of each two polymers were mixed to determine the feasibility of ATPS formation within this concentration range. This resulted in 16 combinations for each pair of polymers. This comprehensive analysis led to pairs of polymeric aqueous solutions that formed an ATPS, with at least one combination of concentrations (green cells in the upper right diagonal of Figure 6-3). Next these systems were tested for their ability to form a spheroid. From each pair of polymers, we selected only one ATPS containing the smallest concentrations of polymers to ensure minimal changes in the composition of the culture medium. Six biphasic systems resulted in successful formation of a spheroid within the drop phase (green cells in the lower left diagonal of Figure 6-3). This analysis demonstrated the broad utility of different ATPS formulations for 3D cell culture.

6.2.3. High Throughput Formation of Spheroids in Microwell Plates

Evaluation of cellular responses to therapeutic compounds in a 3D microenvironment requires integrating spheroid culture into robotic systems for high throughput compound screening. We adapted the ATPS technology to a standard 96-well

plate format to allow screening of several compounds or multiple concentrations of a compound within a plate. Using a commercial robotic liquid handler equipped with an air displacement pipetting head compatible with 96-well plates, the aqueous DEX phase containing cells is dispensed in each well of the plate to form an individual cell-containing drop. Incubation results in a single spheroid in each well. The size of spheroids within a plate is inherently sensitive to variations in the volume of dispensed drops. We examined this question choosing the ATPS formed with the 5.0%(w/w) PEG35k – 6.4%(w/w) DEX500k pair. DEX drops with a 300 nl volume containing 1×10^4 cells were dispensed into a 96-well plate, followed by 600 nl of pre-aspirated air. Evaluating the distribution of size of drops and resulting spheroids showed that this protocol generated DEX drops of 993±101 μm and spheroids of 349±28 μm in diameter, respectively, within a plate (Figure 6-4a). Incubating spheroids for an additional day led to an increased circularity, i.e., the ratio of largest and smallest diameters, indicating that spheroids become more compact (Figure 6-4a, inset). In addition, the average diameter of spheroids showed a slight increase due to the growth of cells (Figure 6-4a, inset). Following this protocol, we were able to consistently form spheroids in multiple 96-well plates with a standard deviation of ~8% (Figure 6-4b).

For the use of spheroids in drug screening applications, it is crucial that each well contains only a single spheroid. This ensures that all wells exhibit a similar baseline level of cellular metabolic activity, which is often used as an indicator of cellular viability in high throughput screening applications. We found that with the ATPS assay, this is sensitive to the cell density within a drop. Therefore we established an experimental phase diagram to determine a minimum cell density for a given drop volume required for

formation of a single spheroid. Drops of the DEX phase with six different volumes in the range of 50-500 nl containing different cell densities of 0.5-10×10^3/drop were dispensed into wells and formation of a single spheroid or multiple spheroids was evaluated at 24 hrs. Each condition was set with 8 replicates. For each drop volume, we found a minimum cell number to guarantee formation of a single spheroid. This resulted in the phase diagram of Figure 6-5a. The hatched area to the right of each volume indicates cell densities that generate one spheroid within the drop whereas the area to the left of each volume gives multiple spheroids. Within the range of drop volumes and cell densities studied, data follow a linear correlation that can be used to pre-determine a drop volume needed to generate a single spheroid of desired cell density for the cell type tested (Figure 6-5b). This approach should be followed for any cell type of interest if it is desired to form different sizes of spheroids in a particular application.

6.2.4. Long-Term Culture of Spheroids

Next we examined the compatibility of the assay with long-term culture. Spheroids of four different cell densities of 2.5×10^3, 3.5×10^3, 5×10^3 and 7.5×10^3 were generated within 200 nl DEX drops immersed in the aqueous PEG phase. Each condition was set with 48 replicates, i.e., one half of a well plate. After allowing 24 hrs for spheroid formation, we added 50 µl of growth medium to wells to dilute out the polymers and produce a single medium phase. Spheroids were imaged every other day, and 50 µl of medium of each well was robotically replenished to provide fresh nutrients to cells. The volume of each spheroid was calculated from its measured diameter assuming a spherical shape. Figure 6-6 shows that the volume of spheroids of all four densities increases

consistently, demonstrating that spheroids are viable, proliferative, and exhibit normal growth. As anticipated, larger density spheroids show greater growth indicated by the slope of growth curve (e.g. compare 0.025 mm^3/day for spheroids of largest cell density and 0.006 mm^3/day for the smallest density spheroids). The ease of generating and maintaining spheroids in standard 96-well plates and robotic exchange of media enables convenient long-term culture for at least seven days and study of growth dynamics of spheroids. Therefore, cancer cell spheroids produced by the ATPS approach mimic growth of solid tumors over time.

6.3. Summary

In summary, we presented a novel spheroid culture microtechnology that offers unprecedented benefits. This approach enables spontaneous formation of uniformly sized spheroids without external forces, immersion of cells in a bath of media throughout culture, ease of formation of spheroids of low and high cell density, convenient handling of plates during culture, compatibility with different polymeric ATPS formulations, and full compatibility with commercially available liquid handling robots and microplate readers. This approach to 3D culture of cells will benefit a broad range of applications in tissue engineering and drug library screening in cancer research and oncology drug discovery.

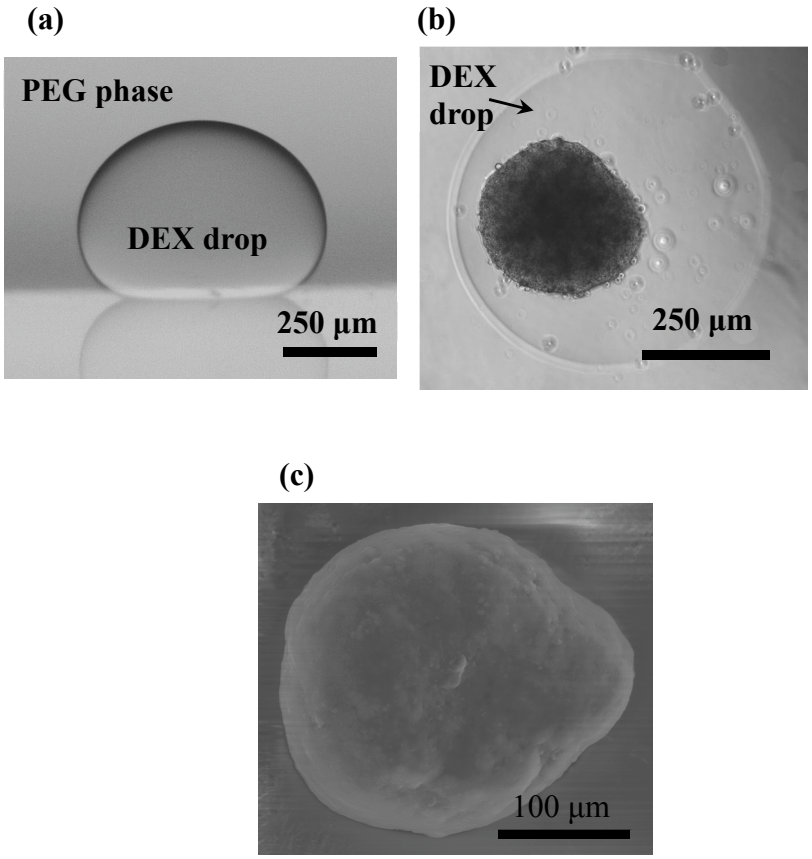

Figure 6-1 (a) Side view of a DEX phase drop in the immersion PEG phase formed on a glass surface using equilibrated phases from an ATPS with initial concentrations of 6.4% DEX and 5.0% PEG. (b) A top-view of A431.H9 skin cancer cell spheroid formed with a cell density of 1×10^4 cells at 24 hrs. (c) Scanning electron microscope (SEM) image of A431.H9 cells after one week of incubation. Reprinted with permission from [143]. Copyright (2014) John Wiley and Sons.

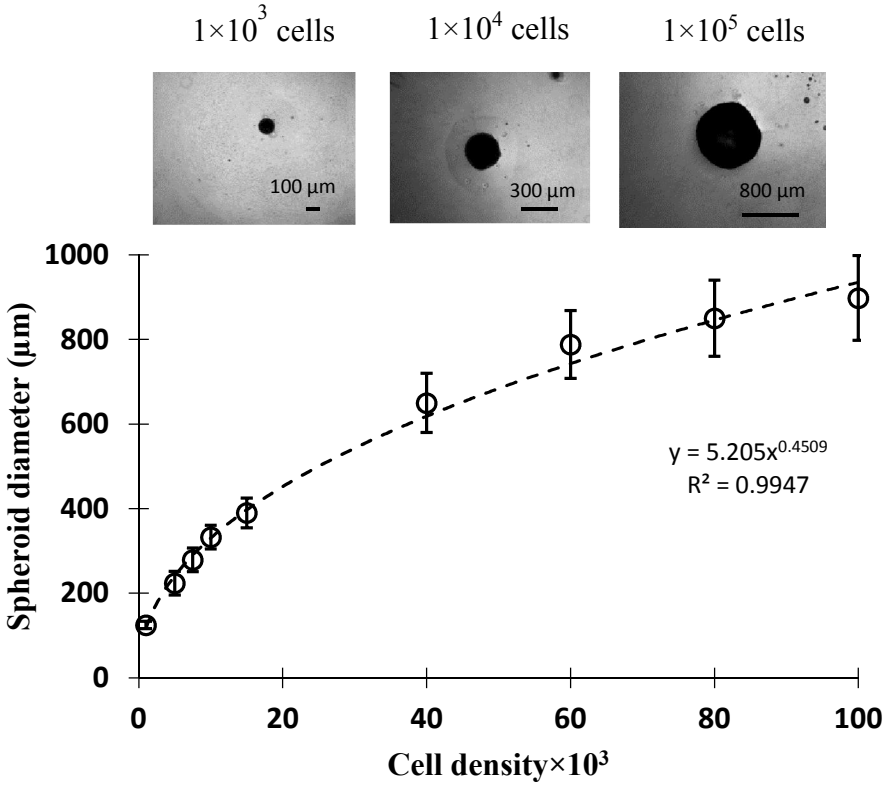

Figure 6-2 Spheroids were generated using a wide range of density of cells, i.e., 1×10^3 cells/spheroid to 1×10^5 cells/spheroid, to demonstrate the feasibility of forming different size tumor models. Reprinted with permission from [143]. Copyright (2014) John Wiley and Sons.

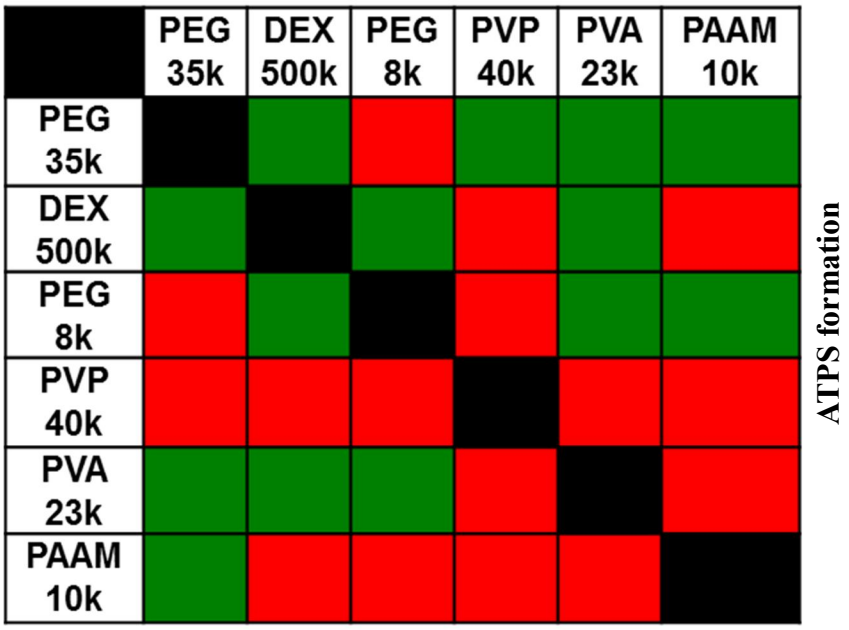

Figure 6-3 Aqueous solutions of a library of different polymers were tested in pairs for the formation of an ATPS (upper right diagonal of the table) and spheroid (lower left diagonal of the table). Green color indicates successful formation whereas red color means the lack of formation. Reprinted with permission from [143]. Copyright (2014) John Wiley and Sons.

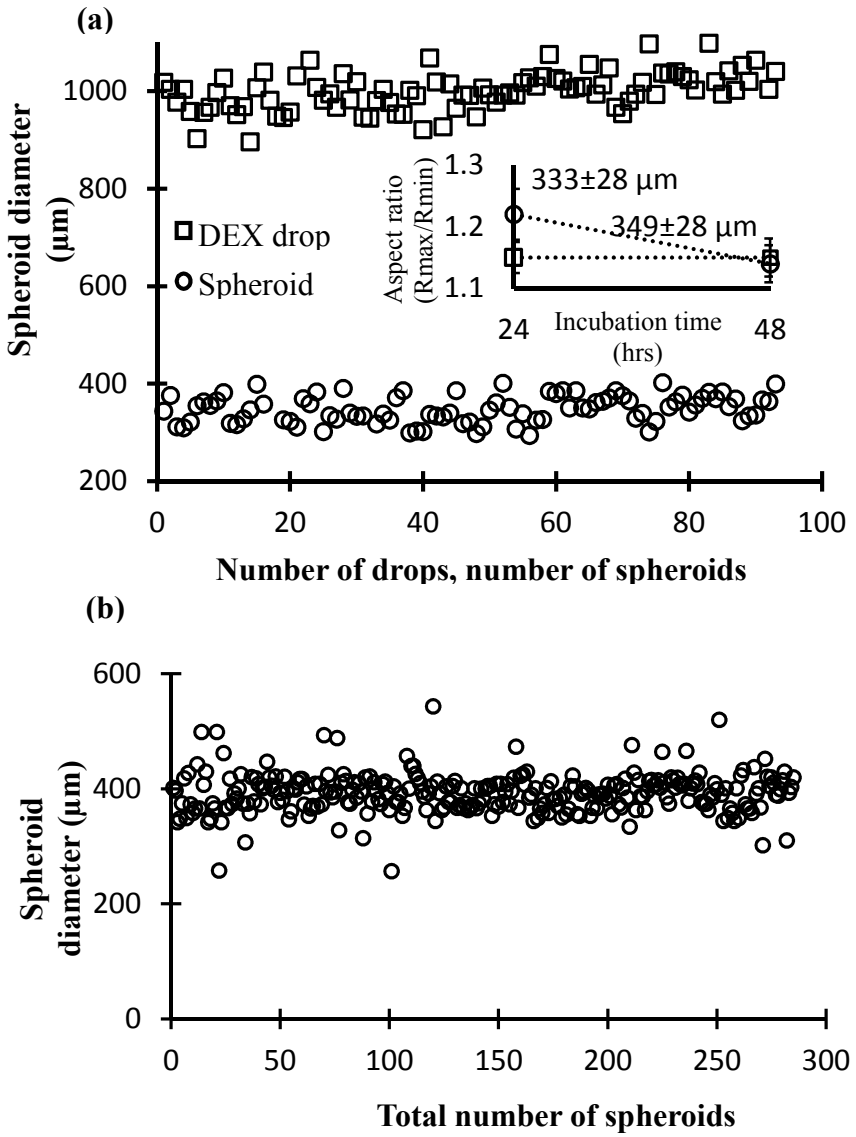

Figure 6-4 (a) Distribution of diameter of DEX drops (squares) and spheroids (circles) within a 96-well plate after 48 hrs of incubation. Spheroids formed from a cell density of 1×10^4 cells within 300 nl-volume DEX drops. Average diameters of drops and spheroids are 993±101 µm and 349±28 µm, respectively. The inset graph represents the change in the average circularity of spheroids within the incubation period of 24 hrs to 48 hrs. Spheroids become more compact and their average diameter increase by 1.1% (p<0.05). (b) Distribution of diameter of spheroids from three separate 96-well plates. Data show an average of 392±32 µm, i.e., a standard deviation of 8.2%. Reprinted with permission from [143]. Copyright (2014) John Wiley and Sons.

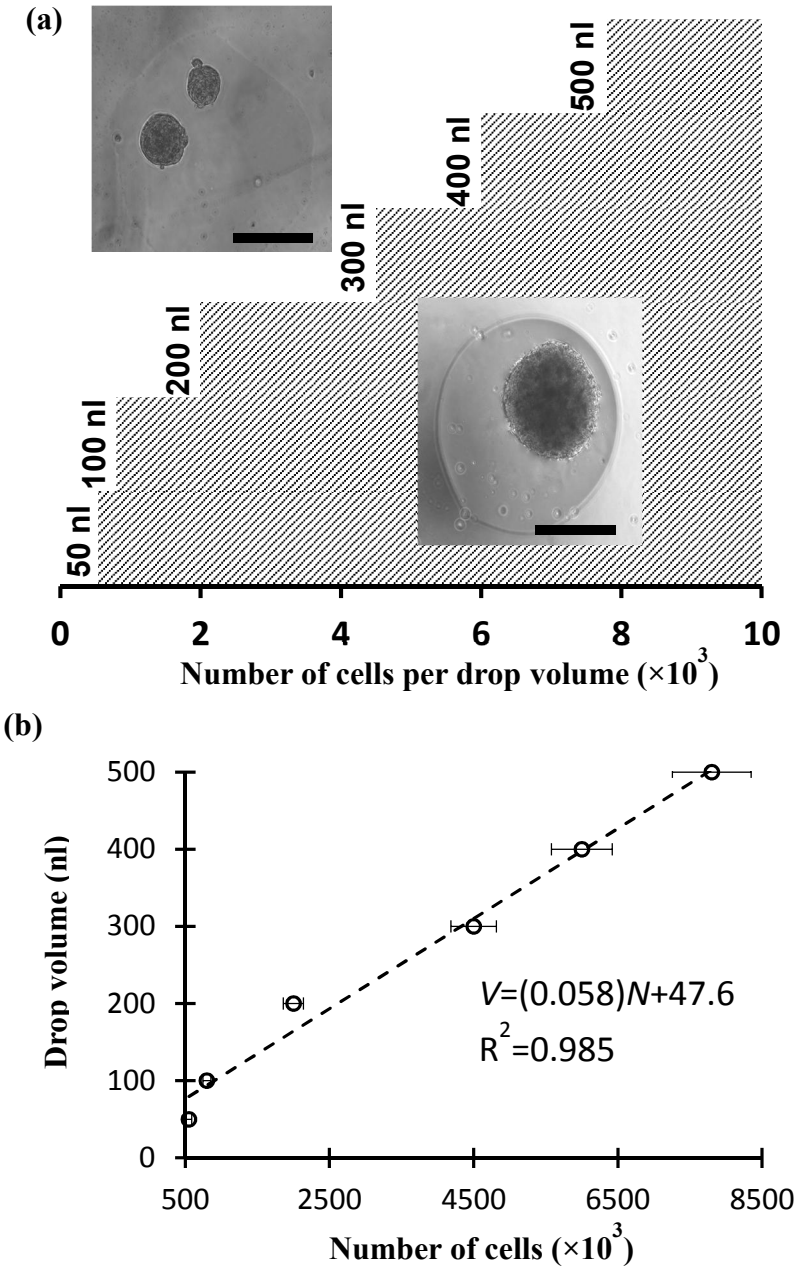

Figure 6-5 (a) An experimental phase diagram determines the correlation between the volume of a DEX drop and the minimum number of cells in the drop to result in formation of a single spheroid. The area of single spheroid formation for drop volumes of 50-500 nl is highlighted by the hatched pattern. A linear equation of $V=(0.058)N+47.6$ fits the data (V: drop volume in nanoliters, N: cell number). (b) The volume of DEX drops (V) to facilitate formation of a single spheroid from a desired number of cells (N) follows a linear relationship within the range of cell density studied. Scale bar is 250 μm. Reprinted with permission from [143]. Copyright (2014) John Wiley and Sons.

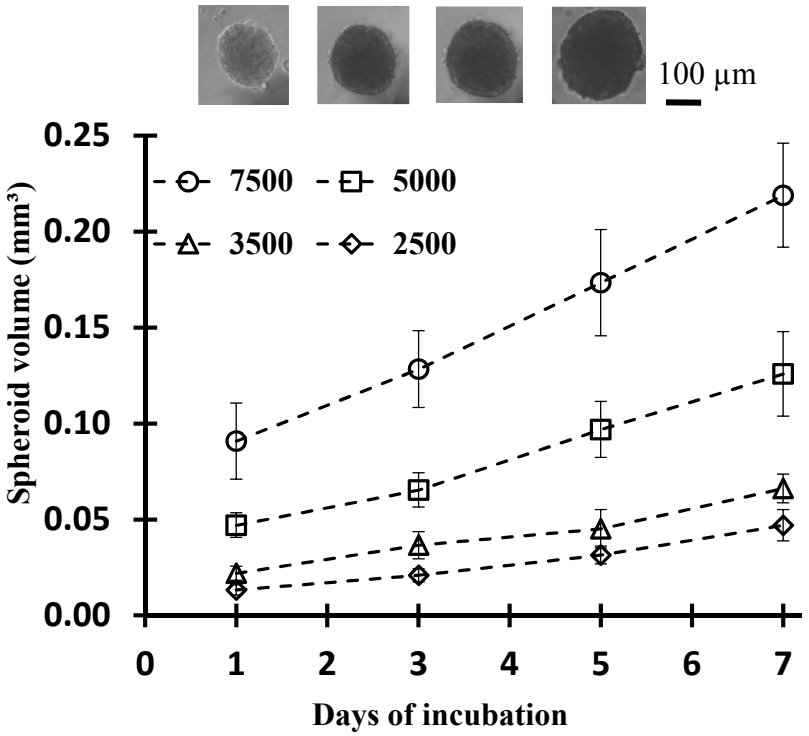

Figure 6-6 Spheroids were formed using four different cell densities, each with half of a 96-well plate, and incubated for 7 days. Images show the growth of spheroids formed with a cell density of 5×10^3 over the 7-day culture. Data from spheroids of different densities at each day are statistically different ($p<0.05$). Except for day 1-3 for 2.5×10^3 density and day 3-5 for 3.5×10^3 density, data for each density over the 7-day culture are statistically different ($p<0.05$). Reprinted with permission from [143]. Copyright (2014) John Wiley and Sons.

CHAPTER VII

ANTI-CANCER DRUG TESTING WITH 3D CELL CULTURES

Increasing evidence shows that conventionally used 2D cell cultures are an irrelevant model for anti-cancer drug screening[152], [153]. Traditionally, anti-cancer drugs showing high efficacy against cells grown in a monolayer have been selected for preclinical in vivo studies[154]. However, in preclinical tests, anti-cancer drugs are rejected with a rate as high as ~98%[19]–[21], [155]. The lack of close cell-cell interactions, and gradients of metabolic waste products, nutrients, and oxygen in monolayer of cells bring about significant changes in expression of genes and proteins and as a result, in phenotypic responses of cells to therapeutic compounds compared to tumor cells[156]. This disparity is believed to be a major reason for such a high rate of failure of drug candidates in the process of oncology drug discovery. On the other hand, 3D cancer cell culture techniques allow formation of tumor-like cellular structures that recapitulate some of key features of tumors including morphology, gradients of nutrients and oxygen and hence presence of a hypoxic core, and overexpression of certain genes and proteins that render cells drug resistant and give rise to stem-like cancer cells with the ability to re-populate a tumor even after treatment with potent drugs[13], [23], [24]. As such, 3D cultures of cancer cells provide a state-of-the-art tool for compound testing and drug discovery. In chapter VI, we presented a high throughput technology for 3D cell culture of cancer cells known as spheroids. In this chapter, we demonstrate the feasibility of using

this technology for high throughput testing of anti-cancer drugs. Spheroids of A431.H9 skin cancer cells and MDA-MB-157 triple negative breast cancer cells are generated in 96-well plates and treated with several clinically used anti-cancer drugs. Results are also compared to monolayer cultures of cells to show significant differences in cellular response to drugs. We optimize an add-on PrestoBlue assay for measuring metabolic activity of cells in spheroids. An easy-to-handle ATPS-based 3D cell culture technique used along with this modified add-on assay for cell viability measurements provides a unique tool for anti-cancer drug testing and discovery of novel chemical compounds.

7.1. Materials and Methods

In this section, preparation of cancer cell spheroids for anti-cancer drug testing is explained. In addition, the experimental procedures of preparing anti-cancer drugs at desired concentration and performing cell viability assays are presented.

7.1.1. Cell Culture

A431.H9 skin cancer cells and MDA-MB-157 triple negative breast cancer cells were maintained in DMEM supplemented with 10% FBS, 1% glutamine, and 1% antibiotic as explained in detail in chapter V. Cells were cultured at 37°C and 5% CO_2 and trypsinized using 3 ml of trypsin (Life Technologies) for 2 to 6 minutes. Trypsin was neutralized with 6 ml of growth medium. The cell suspension was centrifuged at 1000 rpm for 5 min, cells were resuspended in 1 ml of medium, and counted with a hemocytometer.

7.1.2. Cancer Cell Spheroid for Anti-Cancer Drug Testing

Cancer cell spheroids were formed using the ATPS technology as explained in chapter VI. ATPS was made with 5.0% (w/w) PEG 35k and 12.8% (w/w) DEX 500k in the growth medium. Each well of an ultralow attachment round bottom 96-well plate (Nunc) was loaded with 50 µl of 5.0% aqueous PEG phase. Then, a 300 nl drop of the DEX phase containing 15×10^3 cancer cells was robotically aspirated from a source plate and dispensed into each well of the 96-well plate. The plate was incubated at 37°C and 5% CO_2 for 24hrs to allow formation of spheroids. To ensure consistency in size of spheroids, spheroids were imaged (AxioObserver A1, Zeiss) and their diameter was measured. If spheroids with diameter of 10% larger or smaller than the plate average diameter were present, they were discarded from drug testing and analysis.

7.1.3. Drug Preparation

Cisplatin (Spectrum Chemicals), paclitaxel (Calbiochem), and doxorubicin (Sigma Aldrich) were dissolved in ultrapure sterile water at 2 mg/ml, dimethylsulfoxide (DMSO, ATCC) at 10 mg/ml, and in DMSO at 10 mg/ml, respectively. The stock solution of cisplatin was kept at room temperature whereas, those of doxorubicin and paclitaxel were stored at -20ºC. Working concentrations were prepared using serial dilutions of the stock solutions in the growth medium. Drug dilutions were prepared at twice the desired final concentration before adding to an equal volume of the culture medium in each well.

7.1.4. Drug Treatment of Monolayer of Cells

To prepare a uniform cell monolayer, 50 µl of growth medium containing 20×10^3 cells was added to each well of a flat-bottom tissue culture treated 96-well plate (Corning). Cells were incubated at 37°C and 5% CO_2 to adhere and spread for 24 hrs. Then, 50 µl of each drug concentration was added to each well. Each condition had 16 replicates, i.e., two columns from a plate. Drug solutions were at twice the desired final concentration to account for 50 µl of growth media already existing in each well. Cells were incubated with drugs for 24 hrs during and the plate was protected from light.

7.1.5. Drug Treatment of Cancer Cell Spheroids

Spheroids were grown in round-bottom 96-well plates containing 50 µl of the aqueous PEG phase, for 24 hrs at 37°C and 5% CO_2. Each well was imaged to ensure the presence of a single spheroid with a diameter within ±10% of the average diameter. Using a multichannel pipette, 50 µl of from each concentration of a drug was added to spheroids. The addition of the drug solution diluted out the polymer concentrations in ATPS and resulted in only a single media phase containing small amounts of PEG and DEX.

7.1.6. Viability Assay Based on Metabolic Activity of Cells

Viability of cells in 2D and 3D cultures was evaluated using a PrestoBlue reagent (Life Technologies). PrestoBlue is a resazurin-based assay and functions as a cell viability indicator. In presence of reducing environment of proliferative cells, resazurin is reduced to resorufin. Resazurin is a cell permeant compound and is blue in color and weakly fluorescent. On the other hand, resorufin is red in color and highly fluorescent. PrestoBlue

reagent was added to wells at 10% of total well volume of 100 µl. Monolayer and spheroid cultures were incubated with PrestoBlue for 15 min and 6 hrs, respectively. Cell viability was determined using a standard microplate reader (SpectraMax M2, Molecular Devices) that measures the fluorescent intensity from each well at excitation and emission wavelengths of 560 nm and 590 nm, respectively. The fluorescent intensities collected from treated samples (8 to 16 replicates) with a particular drug concentration were averaged and normalized against control spheroids (no drug treatment) to calculate the cell viability of treated samples.

7.1.7. Live-Dead Cell Staining Assay

After removing the ATPS media, spheroids were washed with PBS three times. Next, 100 µl of a dye solution containing 5 µM of Calcein AM, live cell indicator, and ethidium homodimer-1, dead cell indicator, (Life Technologies) was added. Spheroids were incubated for 3 hrs in the presence of the dyes, and the dye solution was gently replaced with PBS. Images were captured using an inverted fluorescent microscope (Axio Observer A1, Zeiss) equipped with a high resolution camera (Axiocam MRm, Zeiss).

7.1.8. Analyzing Dose-Dependent Drug Responses of Cells

After reading viability of drug-treated spheroids and averaging the signal for each concentration corresponding to a particular cell viability, percent viability data were normalized with respect to the control, non-treated samples' viability, and plotted versus drug concentrations. A code was developed in Matlab (MathWorks) to fit a sigmoidal curve

to dose-dependent drug responses[28]. This code implemented a nonlinear fitting to find the coefficients of equation 7-1 below.

$$V = C_1 + \frac{C_2}{1+e^{\frac{C_3-[D]}{C_4}}}, \quad (7\text{-}1)$$

where C_1, C_2, C_3 and C_4 are unknown coefficients. V denotes the percent viability and [D] represents the drug concentration in molar units.

Using this equation, the LD_{50} value was calculated. LD_{50}, read as 50% lethal dose, represents a drug concentration that produces half of the maximum effect observed with that drug. In general, a lower LD_{50} indicates that smaller concentrations of the drug is required to reach the half of maximum drug effect (drug effect=1-viability). In addition, to evaluate the robustness of the ATPS assay technology for drug testing assay, a Z' factor was calculated using equation 7-2 below[157].

$$Z' = 1 - \frac{3\sigma_{PC}+3\sigma_{NC}}{|\mu_{PC}-\mu_{NC}|}, \quad (7\text{-}2)$$

where σ and μ denote the standard deviation and mean values, respectively. PC and NC represent positive and negative controls, respectively. A Z'>0.5 represents an excellent high throughput assay[157].

7.1.9. Statistical Analysis

Statistical analysis is performed using Matlab. Results are presented as mean ± standard deviation. Differences between means are determined using one-way ANOVA. P-value smaller than 0.05 is considered as statistically significantly different.

7.2. Results and Discussion

In this section, optimization of the PresoBlue assay for measuring metabolic activity of cells in spheroids is presented. Drug testing with cisplatin and paclitaxel against monolayer and spheroids of A431.H9 skin cancer cells is discussed. Finally, dose dependent response of MDA-MB-157 breast cancer cell spheroids treated with doxorubicin is presented.

7.2.1. Optimization of PrestoBlue Viability Assay

Identifying an appropriate viability assay that is compatible with 3D cell cultures and sufficiently sensitive to detect changes in viability of cancer cell spheroids due to drug treatment is extremely important. Among viability assays, we selected the PrestoBlue assay because (i) it is an add-on assay, which allows reading cell viabilities in the same plate that spheroids are formed in, (ii) it does not require any wash step, and (iii) it resolves cell viability of 2D cultures very quickly, in 20 min, compared to other assays such as AlamarBlue that require several hours of incubation. To evaluate the sensitivity of PrestoBlue assay, we optimized the time of incubation and the number of cells required. Four different A431.H9 skin cancer cell densities of 1×10^3, 1×10^4, 6×10^4, and 1×10^5 were used, each density with 16 replicates. Then, the PrestoBlue reagent was added to each well and incubated with cells. The fluorescent signal was measured using a plate reader at four different time points of 5, 60, 120, and 360 minutes. Figure 7-1 presents average values of fluorescent intensities measured from spheroids with each cell density. It is clear that the fluorescent intensity increases linearly within 360 min of incubation. The difference between metabolic activities of spheroids of different densities becomes statistically

significantly different at 60 min of incubation (Figure 7-1). Longer incubation times result in a greater difference. Moreover, the fluorescent signal is significantly different after 120 minutes of incubation for spheroids generated with the same cell density, when all densities are considered (Figure 7-2). This optimization indicates that the PrestoBlue assay requires at least 120 min of incubation with spheroids before reading the fluorescent signal with a plate reader for calculating cell viability. To ensure generating highly reliable data, we chose an incubation time of 360 min that returns considerably different fluorescent intensity values that change linearly over time. Figure 7-3 presents the distribution of fluorescent intensity generated with 32 spheroids for two densities of 1×10^3 and 1×10^4 cells after 360 minutes of incubation with PrestoBlue, showing the reproducibility of this assay for measuring cell viability. Based on this optimization study, all the drug-treated spheroids were incubated for 360 min with PrestoBlue before reading the fluorescent intensities.

7.2.2. Anti-Cancer Drug Testing with Spheroids

To demonstrate the feasibility of compound screening with ATPS 3D cell culture technology, we selected two clinically used epithelial cancer drugs and evaluated their efficacy against spheroids of A431.H9 skin cancer cells. Cisplatin was used in a range of 0 - 3 mM with 16 concentrations and paclitaxel was used in the 0 - 10 μM range with 10 different concentrations[4], [5], [28]. Parallel experiments were set with monolayer culture of these cells to examine differential response of cells to drugs. Both spheroid and monolayer cultures showed a dose-dependent response to the drugs. With cisplatin-treated monolayer culture (Figure 7-4a, circles), the drug showed efficacy in a window of 6-130 μM with LD50 of 29.2 μM and a lowest viability of ~10% at the highest concentrations

used. For spheroid cultures treated with cisplatin (Figure 7-4a, triangles), the effective range significantly widened and increased to 20-600 μM, resulting in LD50 of 131.7 μM and a lowest viability of ~30% at the highest concentrations. Paclitaxel was a more potent compound and reduced the viability of monolayer cultures within the 1-100 nM range, resulting in LD50 of 22.1 nM and a minimum viability of ~35% at concentrations greater than 100 nM (Figure 7-4b, circles). The use of spheroid cultures shifted the effective range of paclitaxel to 50 nM-1 μM, increased the LD50 value to 178.5 nM, and reduced cellular viability to ~40% at concentrations larger than 1 μM (Figure 7-4b, triangles). These data indicate that cellular spheroids are more resistant to these drugs compared to their 2D counterparts. Most likely, the 3D compact configuration of spheroids limits diffusion of drugs into the core of spheroids that may contain quiescent but viable cells. In addition, close intercellular contact in spheroids can induce changes in gene expression to confer drug resistance in cells. These tests highlight major differences in the response of 2D and 3D cell cultures to drugs and the need for testing the efficacy of drugs with spheroid models.

We also evaluated the robustness of this technology for drug screening with 3D culture of cells by calculating the Z′ factor using the viability data from each drug as positive control and no drug treatment as negative control. The Z′ factor is a measure of robustness of high-throughput screening assays where any value in the range of 0.5-1.0 indicates an excellent assay. This test consistently returned Z′ factor values of >0.6, demonstrating that the ATPS spheroid technology can robustly and reliably determine effects of drugs on cancer cells in a 3D configuration.

7.2.3. Anti-Cancer Drug Testing with Breast Cancer Cells

To show the versatility of the ATPS 3D cell culture technology, we selected a second cell line from a different tissue. MDA-MB-157 cells, a triple negative breast cancer (TNBC) line, are not a candidate for targeted and hormonal therapies due to the lack of hormone receptors on the surface of cells[158]. This makes chemotherapy the main treatment option for TNBC. Unfortunately, TNBC tumors often do not respond well to standard chemotherapy drugs. Therefore the ability to evaluate the efficacy of chemotherapeutics in vitro with relevant TNBC tumor models can make a significant impact on expediting the availability of newer and more effective compounds for treating patients. TNBC cell spheroids were formed using 15×10^3 cells in each well and grown for 24 hrs in a 96-well plate. First, we confirmed that the optimization of PrestoBlue performed with A431.H9 cells is applicable to MDA-MB-157 spheroids too. PrestoBlue reagent was added to 20 wells of the plate containing spheroids. Figure 7-5 shows that the average fluorescent signal from these samples increases linearly over 360 min of incubation, in agreement with results in Figure 7-1.

Figure 7-6 presents cell viability measurements with MDA-MB-157 spheroids treated with doxorubicin, which is clinically used for TNBC, in a concentration range of 0-2 μM. Treatment conditions and duration followed the description above. Doxorubicin shows high efficacy against MDA-MB-157 breast cancer cell spheroids with an effective range of 50 - 1000 nM. This test gave an LD_{50} value of 241 nM and a minimum cell viability of 14±1.6%. Figure 7-6 inset represents sample images of doxorubicin-treated and non-treated (control) spheroids of MDA-MB-157 breast cancer cells. Clear morphological changes and dissociation of drug-treated spheroids can be observed.

To demonstrate limited drug diffusion into spheroids, MDA-MB-157 spheroids of 15×10^3 cells were treated with 200 nM doxorubicin for 24 hrs and subsequently with fluorescent dyes. Live cells were colored green and dead cell were stained red. Figure 7-7 shows that doxorubicin affects cells at the periphery of the spheroid compared to cells located in the core of the spheroid where cells remain metabolically active. At this concentration, longer incubation of spheroids for 5 days with a drug renewal at day 3 reduced cell viability only to ~50% and could not completely eliminate cancer cells. Achieving higher cell death at such clinically achievable drug concentrations remains a major challenge. The availability of the ATPS spheroid technology can significantly benefit such oncology drug discovery efforts.

7.3. Summary

In summary, dose-dependent responses of cancer cell spheroids treated with conventional chemotherapy drugs showed a significant shift from data generated using monolayer of cancer cells. The efficacy of anti-cancer drugs dropped considerably when cells were in a spheroid. For systematic studies of anti-cancer drugs, a commercially available PrestoBlue assay was optimized for measuring cell viability in spheroid cultures. It was concluded that 360 min incubation of spheroids returns reliable viability data for drug treated spheroids. Our new 3D cancer cell culture technology used along with the PrestoBlue assay provides a user-friendly and easy-to-adapt approach for high throughput screening of anti-cancer drugs with physiologically relevant tumor models. The adaptability of this technology with robotic tools and automated screening equipment will expedite compound screening efforts to identify novel anti-cancer drugs.

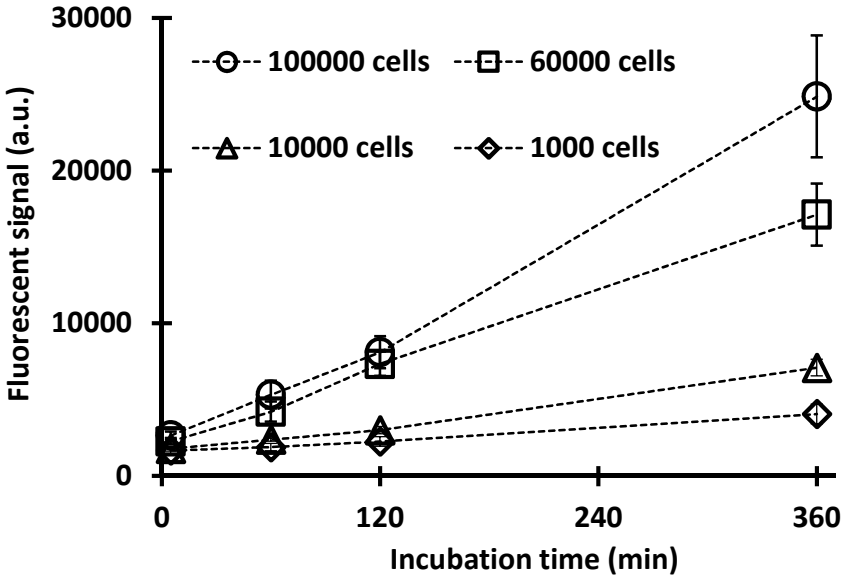

Figure 7-1 Time-dependent increase in the fluorescent signal (metabolic activity) of spheroids of four different cell densities is linear over a 6-hr time period. Data for each cell density were generated using spheroids from two columns of a 96-well plate (n=16).

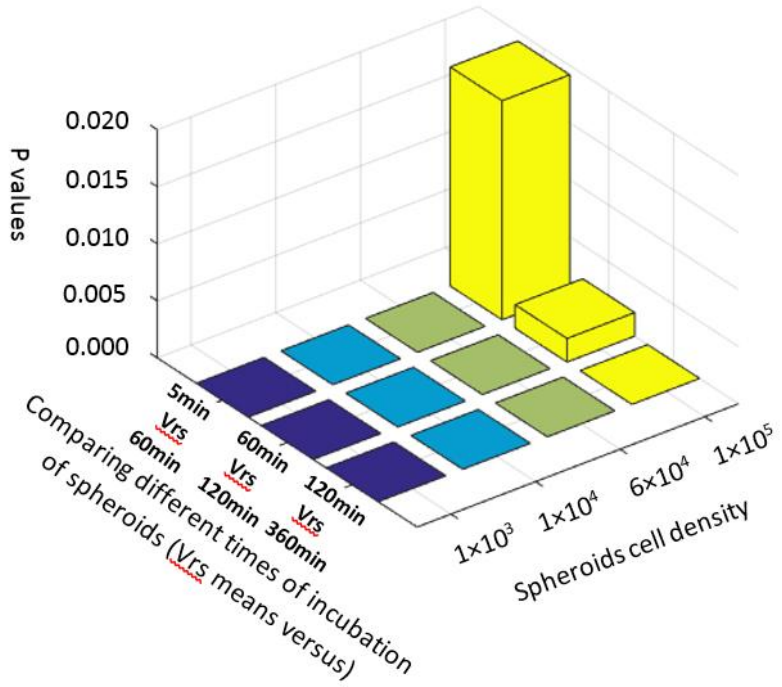

Figure 7-2 P values comparing fluorescent signals measured from spheroids over time of incubation. This figure shows at least 120 min of incubation is needed to generate statistically different fluorescent signals. P values smaller than 0.01 were considered statistically different.

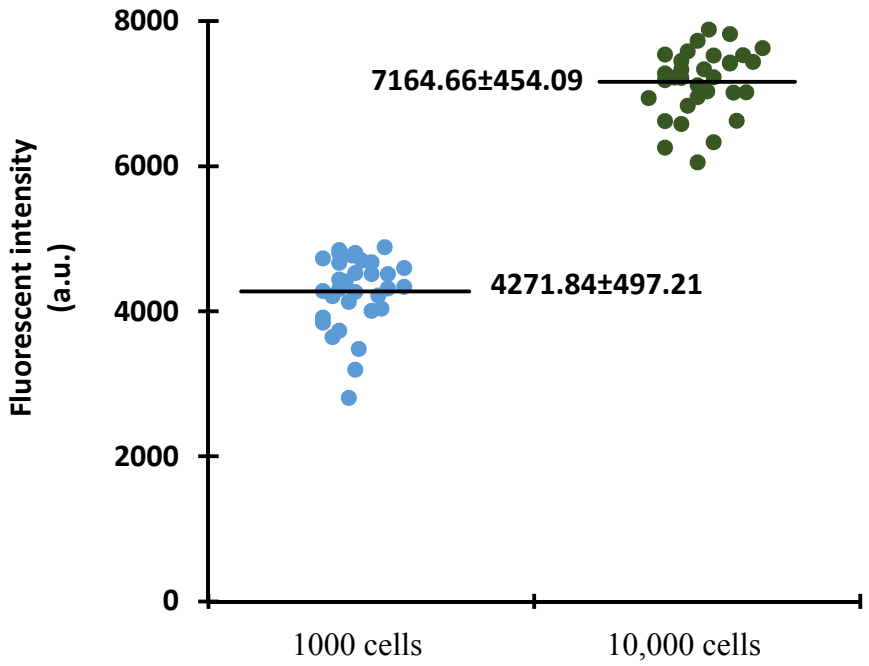

Figure 7-3 Distribution of fluorescent signals collected from 32 replicates of PrestoBlue-added wells containing spheroids of 1×10^3 cell density (blue circles) and 1×10^4 cell density (green circles).

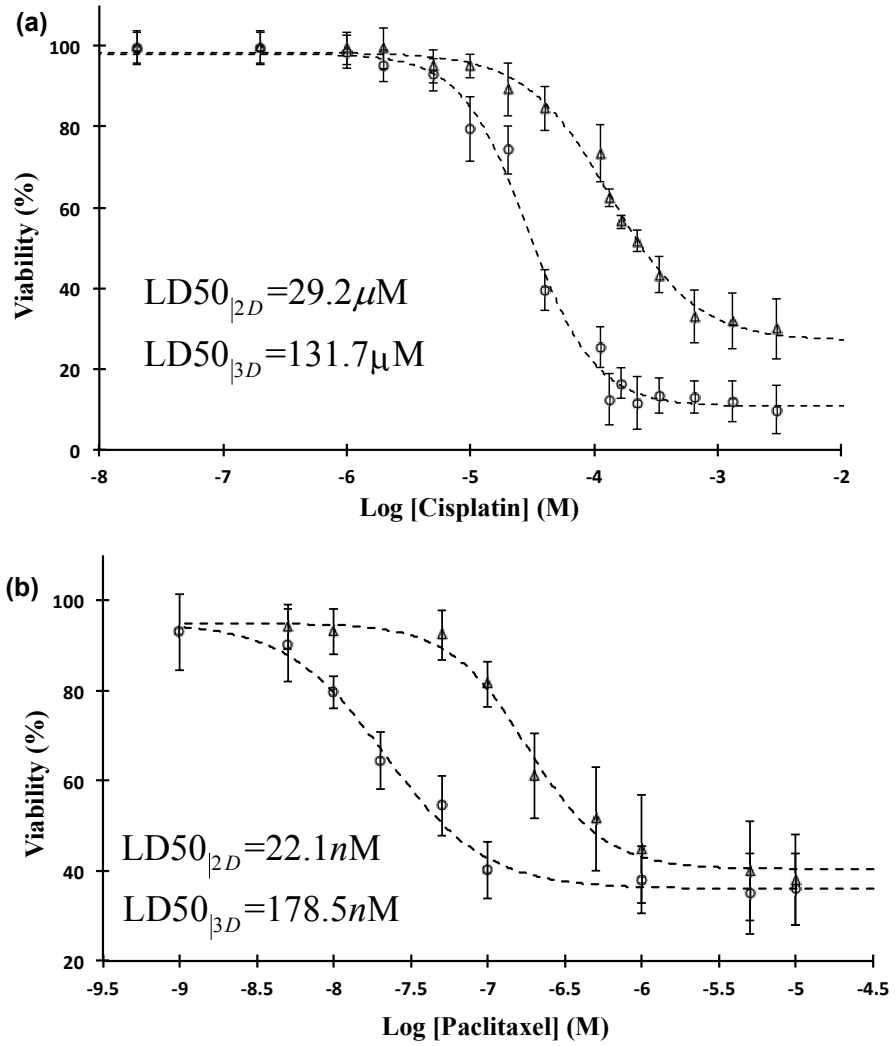

Figure 7-4 Drug response of ATPS-generated spheroids. Percent viability of A431.H9 cells in 2D culture (circles) and 3D culture (triangles) treated with (a) cisplatin and (b) paclitaxel is shown. Each drug concentration and control condition (no treatment) had 16 replicates. Monolayer cultures were treated with similar drug concentrations and number of replicates. Cellular viability was evaluated at 48 hrs using PrestoBlue. At each drug concentration, cell viability was calculated as the ratio of average fluorescent intensities from wells representing the particular concentration and control wells. Dashed lines are a sigmoidal fit to the experimental data. Error bars represent 95% confidence limits.

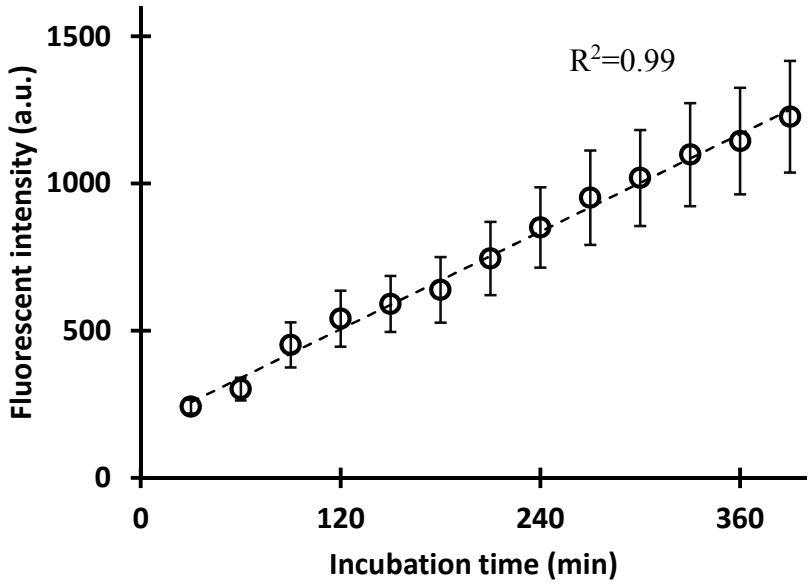

Figure 7-5 Fluorescent intensity values measured with spheroids of 15×10^3 MDA-MB-157 cells incubated with PrestoBlue. Each data point represents an average fluorescent intensity of 20 replicates. The fluorescent intensity changes linearly with the time of incubation.

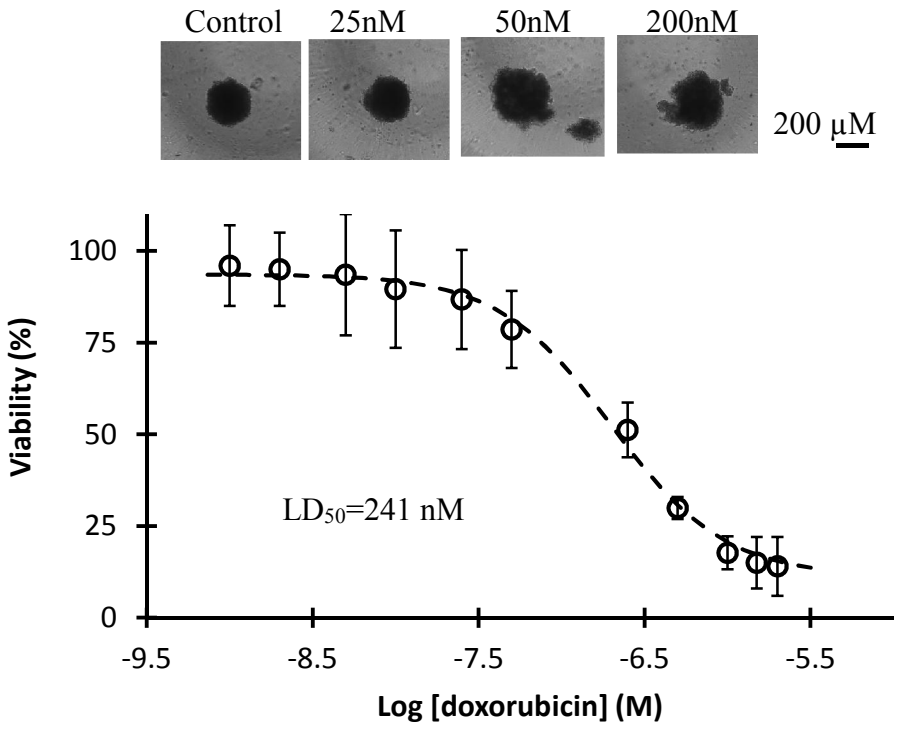

Figure 7-6 Presents viability of spheroids made with MDA-MB-157 breast cancer cells. Spheroids were formed using ATPS technology for 3D cell culture, and grown for 24hrs. Doxorubicin was added to spheroids After 24 hrs. The Spheroids viability was measured on day 5 of treatment.

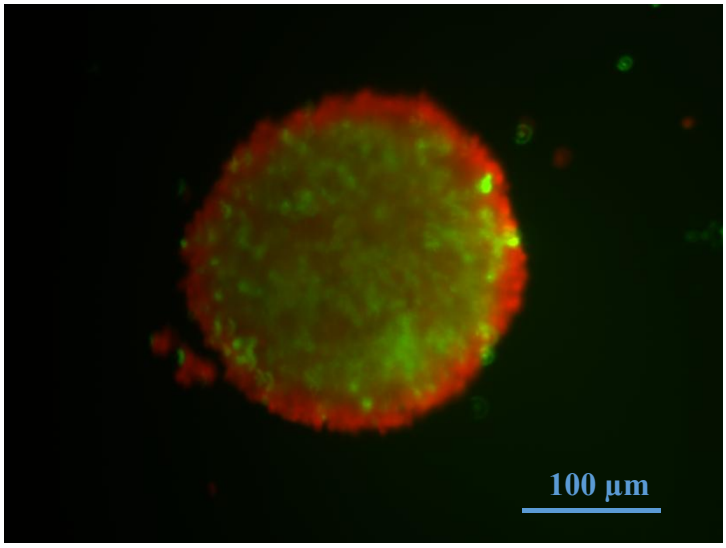

Figure 7-7 A fluorescent image of a spheroid of MDA-MB-157 breast cancer cells treated with 200 nM doxorubicin is shown. Red color represents dead cells and green color represents live cells.

CHAPTER VIII

CONCLUSIONS

A technology was developed for high throughput, 3D culture of cancer cells. This approach is based on a polymeric aqueous two-phase system (ATPS) where cancer cells confined within a drop of the denser aqueous phase, and immersed in the immersion aqueous phase, aggregate to form a spheroid. The compatibility of this technology with standard microwell plates allowed adapting it to a commercial robotic liquid handler for high throughput production of spheroids in 96-well plates. Experimental optimization of the protocol enabled forming a single spheroid of well-defined size with a desired cell density in each well and uniformly-sized spheroids throughout each plate. Resulting spheroids were viable and showed normal morphology and growth during incubation. Formation of spheroids of different cells and the possibility of using different phase-forming polymers demonstrated the versatility of this technology.

A major benefit of the ATPS spheroid technology is the ease of use for screening of chemical compounds due to robotic spheroid formation and reagent addition, and in situ analysis of cellular responses to compounds with plate readers. Considering that only one spheroid formed in each well, this approach allowed testing multiple concentrations of a compound in each plate. Prior to feasibility studies of anti-cancer drug testing, incubation time with a PrestoBlue viability assay was optimized to determine the efficacy of chemical compounds tested with cancer cell spheroids. Clinically-used chemotherapy drugs

cisplatin, paclitaxel, and doxorubicin dose-dependently reduced the viability of spheroids of a skin cancer cell line A431.H9, but at substantially higher drug concentrations compared to monolayer culture of cells, demonstrating drug resistance of cells in a 3D environment. Unlike existing techniques, this add-on spheroid culture technology significantly simplified spheroid formation and drug testing and analysis to facilitate incorporation of 3D cancer cell cultures in drug screening applications.

The feasibility of spheroid formation with ATPS critically depended on confinement of cancer cells within the drop phase. We conducted an experimental-theoretical study to determine the role of interfacial tension of ATPS on the partition of cells between the two aqueous phases and their interface. A very small interfacial tension of ~30 $\mu J/m^2$ resulted in the partition of majority of cells to the drop phase, allowing aggregation of cells to a spheroid. Increasing the interfacial tension using larger concentrations of phase-forming polymers significantly reduced the number of cells partitioned to drop phase and interfered with spheroid formation. A thermodynamic model was developed to estimate the free energy changes of displacement of a particle in ATPS. This model used measured values of interfacial tension and contact angle of the particle (cell) at the interface of ATPS and showed that a very small interfacial tension was associated with a minimum free energy, favoring cell partition to the bottom (drop) phase. Increase in the interfacial tension shifted the minimum energy state toward the interface.

The above study of cell partition required interfacial tensions of ATPS. An axisymmetric drop shape analysis (ADSA) methodology was adapted and its image processing module was modified to precisely extract profiles of sessile and pendant drops of ATPS for subsequent Laplacian curve fitting through numerical integration. Due to

sensitivity of ADSA to drop shape, a criterion was developed to evaluate well-deformity of sessile drops. Ultralow interfacial tensions of ATPS measured using both pendant drop and sessile drop configurations showed an excellent agreement. Our systematic measurements with eight different two-phase systems showed that interfacial tensions of ATPS vary linearly with the length of tie-lines on a logarithmic scale.

In addition to interfacial tensions, our thermodynamic model of cell partition used contact angle of a particle (cell) at the interface of ATPS. Due to the difficulty of measuring contact angle involving a single cell, alternatively, contact angles were determined with ATPS on a monolayer of cells. ADSA could not resolve these contact angles due to the asymmetry of drop profiles resulting from corrugations of the three-phase contact line. Therefore, a polynomial fitting technique was developed to estimate the contact angles based on a local fit to left and right halves of each drop profile. This approach was initially validated using axisymmetric drops against ADSA to show that it returns contact angles within ±1° of ADSA. With ATPS solutions, larger contact angles were obtained by increase in the concentration of phase-forming polymers, and hence increase of interfacial tensions.

Altogether, this thesis presented a multidisciplinary approach to develop a new 3D cell culture technology with the potential to streamline the use of tumor spheroids in oncology drug discovery. The possibility of incorporating different components of tumor microenvironment in this modular platform will serve various studies in cancer research to elucidate the role of tumor microenvironment in the response of cancer cells to therapeutics.

CHAPTER IX

FUTURE WORK

In the light of studies presented in this thesis, the following directions may be pursued in future.

1. The use of 3D cultures in the process of anti-cancer drug discovery is expected to increase the success rate of drug development, and thus significantly reduce associated costs. In its current form, the ATPS spheroid technology can be conveniently adapted in research centers and pharmaceutical settings to explore novel chemotherapy drugs. The increase in the throughput of this approach to a 384-well plate format will further expedite the process. In addition, recent availability of genomics data of tumor cells and information about mutations in important signaling pathways (e.g., through The Cancer Genome Atlas Network) has created a unique opportunity to identify small molecule inhibitors for targeted therapies without significant side effects[159].

2. It is well recognized that tumor microenvironment plays a major role in regulating different malignant phenotypes of cancer cells including uncontrolled proliferation, migration and invasion, and response to drugs[13], [17], [23], [24]. For example, signaling between cancer cells and fibroblasts, and cancer cells and the extracellular matrix increases cancer cells proliferation and tumor growth, induces local cell migration and matrix invasion, and causes drug resistance of cancer cells, all of which are implicated in metastatic progression of cancers[13], [17], [23], [24]. The ATPS

spheroid technology provides a unique approach to create the complexity of tumor microenvironment and decipher the role of environmental factors on various phenotypes of cancer cells. This technology is modular in the sense that it can accommodate individual components of tumor microenvironment such as stromal cells, matrix proteins, and immune cells to understand their regulation of function of cancer cells. The high throughput capability of this platform enables evaluating the efficacy of drug candidates for targeting tumor microenvironment.

3. Partition of cells in ATPS is a complex process that is influenced by several parameters including pH and temperature of separation medium, molecular weight of phase-forming polymers, ionic composition of aqueous phases, interfacial tension, hydrophobicity, and surface properties of cells. The cell partition study presented in this thesis can be expanded to consider effects of factors other than interfacial tension and elucidate the interplay between them. Other types of cells with different surface properties should also be considered for these studies. Further refinement of the theoretical model is also required to enable predicting the influence of individual factors on cell partition in ATPS and their collective effect. The approach can serve both partition of cells and fractionation of a particular cell type from a heterogeneous population.

4. Unlike conventional contact angle measurements with liquid drops on solid surfaces in air, the use of ATPS to determine contact angles on cells is the only available method that maintains cells hydrated during measurements. This provides a unique method to characterize the wettability of cells as a measure of their adhesive property. Although the polynomial fitting approach is a simple, yet reasonably accurate method for determination of contact angles on cells, the experimental setup used in this work needs

improvements for better detection of contact points of the drop with the non-transparent cell layer and implementing a temperature control system to maintain cells at a physiologic temperature during experiments.

BIBLIOGRAPHY

[1] "U. S. Department of Health and Human Services, National Institutes of Health, National Cancer Society, What is cancer?," Retrieved from http://www.cancer.gov/about-cancer/what-is-cancer/statistics, 2015.

[2] M. R. Alison, "Cancer," in *eLS*, John Wiley & Sons, Ltd, 2001.

[3] M. K. Bucci, A. Bevan, and M. Roach, "Advances in radiation therapy: conventional to 3D, to IMRT, to 4D, and beyond.," CA. Cancer J. Clin., vol. 55, no. 2, pp. 117–134, 2005.

[4] R. T. Skeel and N. A. Lachant, Handbook of cancer chemotherapy. Little, Brown and Company, 1995.

[5] I. Burney, "Cancer Chemotherapy and Biotherapy: Principles and Practice," Sultan Qaboos University Medical Journal, vol. 11, no. 3. Sultan Qaboos University, p. 424, 01-Aug-2011.

[6] K. H. Benam, S. Dauth, B. Hassell, A. Herland, A. Jain, K.-J. Jang, K. Karalis, H. J. Kim, L. MacQueen, R. Mahmoodian, S. Musah, Y. Torisawa, A. D. van der Meer, R. Villenave, M. Yadid, K. K. Parker, and D. E. Ingber, "Engineered In Vitro Disease Models," *Annu. Rev. Pathol. Mech. Dis.*, vol. 10, no. 1, pp. 195–262, 2015.

[7] J. C. M. Uitdehaag, J. D. M. de Roos, A. M. van Doornmalen, M. B. W. Prinsen, J. P. Spijkers-Hagelstein, J. R. F. de Vetter, J. de Man, R. C. Buijsman, and G. J. R. Zaman, "Selective Targeting of CTNBB1-, KRAS- or MYC-Driven Cell Growth by Combinations of Existing Drugs," *PLoS One*, vol. 10, no. 5, p. e0125021, 2015.

[8] C. Holohan, S. Van Schaeybroeck, D. B. Longley, and P. G. Johnston, "Cancer drug resistance: an evolving paradigm.," *Nat. Rev. Cancer*, vol. 13, no. 10, pp. 714–26, 2013.

[9] M. McDermott, A. J. Eustace, S. Busschots, L. Breen, J. Crown, M. Clynes, N. O'Donovan, and B. Stordal, "In vitro Development of Chemotherapy and Targeted Therapy Drug-Resistant Cancer Cell Lines: A Practical Guide with Case Studies.," *Front. Oncol.*, vol. 4, p. 40, Jan. 2014.

[10] L. R. L. Mataga, M. A. Rosenthal, S. Heerboth, S. Devalapalli, A. Kokolus, S. Evans, "Anti-breast Cancer Effects of Histone Deacetylase Inhibitors and Calpain Inhibitor," *Anticancer Res*, vol. 32, no. 7, pp. 2523–2529, Jul. 2012.

[11] M. Suggitt and M. C. Bibby, "50 years of preclinical anticancer drug screening: empirical to target-driven approaches.," *Clin. Cancer Res.*, vol. 11, no. 3, pp. 971–81, Mar. 2005.

[12] Biocentury Online Intelligence, "Pipeline Analyst," *retrieved from http://www.biocentury.com/BCIQ*, 2015. .

[13] L. C. Kimlin, G. Casagrande, and V. M. Virador, "In vitro three-dimensional (3D) models in cancer research: An update," *Mol. Carcinog.*, vol. 52, no. 3, pp. 167–182, 2013.

[14] F. Hirschhaeuser, H. Menne, C. Dittfeld, J. West, W. Mueller-Klieser, and L. a. Kunz-Schughart, "Multicellular tumor spheroids: An underestimated tool is catching up again," *J. Biotechnol.*, vol. 148, no. 1, pp. 3–15, 2010.

[15] T. Riss, "Selecting Cell - Based Assays For Drug Discovery Screening," *Cell Note Issue*, no. 13, pp. 16–21, 2005.

[16] A. W. Du, H. Lu, and M. H. Stenzel, "Core-crosslinking accelerates anti-tumor activities of paclitaxel-conjugate micelles to prostate multicellular tumor spheroids: a comparison of 2D and 3D models," *Biomacromolecules*, p. 150409213751005, 2015.

[17] S. Raghavan, M. R. Ward, S. T. Katelyn R Rowleyb, Rachel M. Woldb, and G. Mehta, "Formation of stable small cell number three-dimensional ovarian cancer spheroids using hanging drop arrays for preclinical drug sensitivity assays," *Gynecol. Oncol.*, vol. 138, no. 2, pp. 1–25, 2015.

[18] H. Kim, Y. Phung, and M. Ho, "Changes in global gene expression associated with 3D structure of tumors: an ex vivo matrix-free mesothelioma spheroid model.," *PLoS One*, vol. 7, no. 6, p. e39556, Jan. 2012.

[19] M. Lu, F. Zhou, K. Hao, J. Liu, Q. Chen, P. Ni, H. Zhou, G. Wang, and J. Zhang, "Alternation of adriamycin penetration kinetics in MCF-7 cells from 2D to 3D culture based on P-gp expression through the Chk2/p53/NF-κB pathway," *Biochem. Pharmacol.*, vol. 93, no. 2, pp. 210–220, 2015.

[20] T. Liu, R. Yacoub, L. D. Taliaferro-Smith, S.-Y. Sun, T. R. Graham, R. Dolan, C. Lobo, M. Tighiouart, L. Yang, A. Adams, and R. M. O'Regan, "Combinatorial effects of lapatinib and rapamycin in triple-negative breast cancer cells.," *Mol. Cancer Ther.*, vol. 10, no. 8, pp. 1460–1469, 2011.

[21] H. Kenny, M. Lal-Nag, E. a. White, M. Shen, C.-Y. Chiang, A. K. Mitra, Y. Zhang, M. Curtis, E. M. Schryver, S. Bettis, A. Jadhav, M. B. Boxer, Z. Li, M. Ferrer, and E. Lengyel, "Quantitative high throughput screening using a primary human three-dimensional organotypic culture predicts in vivo efficacy," *Nat. Commun.*, vol. 6, p. 6220, 2015.

[22] L. E. Jamieson, D. J. Harrison, and C. J. Campbell, "Chemical analysis of multicellular tumour spheroids," *Analyst*, vol. 140, no. 15, 2015.

[23] V. Das, F. Bruzzese, P. Konečný, F. Iannnell, A. Budillon, and M. Hajdúch, "Pathophysiologically relevant in vitro tumor models for drug screening," *Drug Discov. Today*, vol. 00, no. 00, 2015.

[24] B. M. Baker and C. S. Chen, "Deconstructing the third dimension - how 3D culture microenvironments alter cellular cues," *J. Cell Sci.*, vol. 125, no. 13, pp. 3015–3024, 2012.

[25] Y. Zhao, R. Yao, L. Ouyang, H. Ding, T. Zhang, K. Zhang, S. Cheng, and W. Sun, "Three-dimensional printing of Hela cells for cervical tumor model in vitro.," *Biofabrication*, vol. 6, no. 3, p. 035001, 2014.

[26] L. Zheng, X. Hu, Y. Huang, G. Xu, J. Yang, and L. Li, "*In vivo* bioengineered ovarian tumors based on collagen, matrigel, alginate and agarose hydrogels: a comparative study," *Biomed. Mater.*, vol. 10, no. 1, p. 015016, 2015.

[27] L.-B. Weiswald, D. Bellet, and V. Dangles-Marie, "Spherical Cancer Models in Tumor Biology," *Neoplasia*, vol. 17, no. 1, pp. 1–15, 2015.

[28] M. Fallahi-Sichani, S. Honarnejad, L. M. Heiser, J. W. Gray, and P. K. Sorger, "NIH Public Access," *Nat. Chem. Biol.*, vol. 9, no. 11, pp. 708–14, 2013.

[29] S. I. Montanez-Sauri, D. J. Beebe, and K. E. Sung, "Microscale screening systems for 3D cellular microenvironments: platforms, advances, and challenges," *Cell. Mol. Life Sci.*, vol. 72, no. 2, pp. 237–249, 2014.

[30] E. C. de Bruin and J. P. Medema, "Apoptosis and non-apoptotic deaths in cancer development and treatment response," *Cancer Treat. Rev.*, vol. 34, no. 8, pp. 737–749, 2008.

[31] a. W. Tolcher, K. Khan, M. Ong, U. Banerji, V. Papadimitrakopoulou, D. R. Gandara, a. Patnaik, R. D. Baird, D. Olmos, C. R. Garrett, J. M. Skolnik, E. H. Rubin, P. D. Smith, P. Huang, M. Learoyd, K. a. Shannon, a. Morosky, E. Tetteh, Y.-M. Jou, K. P. Papadopoulos, V. Moreno, B. Kaiser, T. a. Yap, L. Yan, and J. S. de Bono, "Antitumor Activity in RAS-Driven Tumors by Blocking AKT and MEK," *Clin. Cancer Res.*, vol. 21, no. 4, pp. 739–748, 2014.

[32] N. Nakajima, K. Yamakoshi, Y. Yajima, M. Yamada, and M. Seki, "Shape Control of Cell-embedding Hydrogel Microstructures Utilizing Non-equilibrium Aqueous Two-phase Systems," pp. 2–4.

[33] C. Hsieh, Y. Chen, S. Huang, H. Wang, and M. Wu, "The Effect of Primary Cancer Cell Culture Models on the Results of Drug Chemosensitivity Assays : The Application of Perfusion Microbioreactor System as Cell Culture Vessel," no. 1.

[34] S. Breslin and L. O'Driscoll, "Three-dimensional cell culture: The missing link in drug discovery," *Drug Discov. Today*, vol. 18, no. 5–6, pp. 240–249, 2013.

[35] E. C. Costa, V. M. Gaspar, P. Coutinho, and I. J. Correia, "Optimization of liquid overlay technique to formulate heterogenic 3D co-cultures models.," *Biotechnol. Bioeng.*, vol. 111, no. 8, pp. 1672–85, Aug. 2014.

[36] Z.-H. Peng and J. Kopecek, "Enhancing Accumulation and Penetration of HPMA Copolymer Doxorubicin Conjugates in 2D and 3D Prostate Cancer Cells via iRGD Conjugation with an MMP-2 Cleavable Spacer," *J. Am. Chem. Soc.*, p. 150512042324005, 2015.

[37] V. Härmä, R. Haavikko, J. Virtanen, I. Ahonen, H.-P. Schukov, S. Alakurtti, E. Purev, H. Rischer, J. Yli-Kauhaluoma, V. M. Moreira, M. Nees, and K.-M. Oksman-Caldentey, "Optimization of Invasion-Specific Effects of Betulin Derivatives on Prostate Cancer Cells through Lead Development," *PLoS One*, vol. 10, no. 5, p. e0126111, 2015.

[38] D. Wendt, S. A. Riboldi, M. Cioffi, and I. Martin, "Potential and Bottlenecks of Bioreactors in 3D Cell Culture and Tissue Manufacturing," *Adv. Mater.*, vol. 21, no. 32, 2009.

[39] B. M. Leung, S. C. Lesher-Perez, T. Matsuoka, C. Moraes, and S. Takayama, "Media additives to promote spheroid circularity and compactness in hanging drop platform," *Biomater. Sci.*, vol. 3, no. 2, pp. 336–344, 2015.

[40] M. Akashi, Misturu, Akagi, Takami, "Engineered Cell Manipulation for Biomedical Application," in *Springer Japan*, 2014.

[41] C. Kucukgul, S. B. Ozler, I. Inci, E. Karakas, S. Irmak, D. Gozuacik, A. Taralp, and B. Koc, "3D Bioprinting of Biomimetic Aortic Vascular Constructs with Self-Supporting Cells," *Biotechnol. Bioeng.*, pp. 300–15, 2014.

[42] V. van Duinen, S. J. Trietsch, J. Joore, P. Vulto, and T. Hankemeier, "Microfluidic 3D cell culture: from tools to tissue models.," *Curr. Opin. Biotechnol.*, vol. 35, pp. 118–126, Jun. 2015.

[43] S.-M. Ong, C. Zhang, Y.-C. Toh, S. H. Kim, H. L. Foo, C. H. Tan, D. van Noort, S. Park, and H. Yu, "A gel-free 3D microfluidic cell culture system.," *Biomaterials*, vol. 29, no. 22, pp. 3237–44, Aug. 2008.

[44] S. J. Trietsch, G. D. Israëls, J. Joore, T. Hankemeier, and P. Vulto, "Microfluidic titer plate for stratified 3D cell culture.," *Lab Chip*, vol. 13, no. 18, pp. 3548–54, Sep. 2013.

[45] X. J. Li, A. V Valadez, P. Zuo, and Z. Nie, "Microfluidic 3D cell culture: potential application for tissue-based bioassays.," *Bioanalysis*, vol. 4, no. 12, pp. 1509–25, Jun. 2012.

[46] R. Foty, "A simple hanging drop cell culture protocol for generation of 3D spheroids.," *J. Vis. Exp.*, no. 51, Jan. 2011.

[47] N. E. Timmins, S. Dietmair, and L. K. Nielsen, "Hanging-drop multicellular spheroids as a model of tumour angiogenesis.," *Angiogenesis*, vol. 7, no. 2, pp. 97–103, Jan. 2004.

[48] H. Hauser and M. Fussenegger, Eds., *Tissue Engineering*, vol. 140. Totowa, NJ: Humana Press, 2007.

[49] Y.-C. Tung, A. Y. Hsiao, S. G. Allen, Y. Torisawa, M. Ho, and S. Takayama, "High-throughput 3D spheroid culture and drug testing using a 384 hanging drop array.," *Analyst*, vol. 136, no. 3, pp. 473–8, Mar. 2011.

[50] E. Fennema, N. Rivron, J. Rouwkema, C. van Blitterswijk, and J. de Boer, "Spheroid culture as a tool for creating 3D complex tissues.," *Trends Biotechnol.*, vol. 31, no. 2, pp. 108–15, Feb. 2013.

[51] R.-Z. Lin, R.-Z. Lin, and H.-Y. Chang, "Recent advances in three-dimensional multicellular spheroid culture for biomedical research.," *Biotechnol. J.*, vol. 3, no. 9–10, pp. 1172–84, Oct. 2008.

[52] S. M. Ong, Z. Zhao, T. Arooz, D. Zhao, S. Zhang, T. Du, M. Wasser, D. van Noort, and H. Yu, "Engineering a scaffold-free 3D tumor model for in vitro drug penetration studies," *Biomaterials*, vol. 31, no. 6, pp. 1180–1190, 2010.

[53] S. I. Montanez-Sauri, K. E. Sung, J. P. Puccinelli, C. Pehlke, and D. J. Beebe, "Automation of Three-Dimensional Cell Culture in Arrayed Microfluidic Devices," *J. Lab. Autom.*, vol. 16, no. 3, pp. 171–185, 2011.

[54] M. Mehling and S. Tay, "Microfluidic cell culture," *Curr. Opin. Biotechnol.*, vol. 25, pp. 95–102, 2014.

[55] A. I. Minchinton and I. F. Tannock, "Drug penetration in solid tumours.," *Nat. Rev. Cancer*, vol. 6, no. 8, pp. 583–592, 2006.

[56] J.-Y. Kim, D. a. Fluri, R. Marchan, K. Boonen, S. Mohanty, P. Singh, S. Hammad, B. Landuyt, J. G. Hengstler, J. M. Kelm, A. Hierlemann, and O. Frey, "3D spherical microtissues and microfluidic technology for multi-tissue experiments and analysis," *J. Biotechnol.*, pp. 1–12, 2015.

[57] B. M. Leung, C. Moraes, S. P. Cavnar, K. E. Luker, G. D. Luker, and S. Takayama, "Microscale 3D Collagen Cell Culture Assays in Conventional Flat-Bottom 384-Well Plates," *J. Lab. Autom.*, 2014.

[58] A. L. Howes, R. D. Richardson, D. Finlay, and K. Vuori, "3-Dimensional Culture Systems for Anti-Cancer Compound Profiling and High-Throughput Screening Reveal Increases in EGFR Inhibitor-Mediated Cytotoxicity Compared to Monolayer Culture Systems," *PLoS One*, vol. 9, no. 9, p. e108283, 2014.

[59] E. Knight and S. Przyborski, "Advances in 3D cell culture technologies enabling tissue-like structures to be created in vitro," *J. Anat.*, p. n/a–n/a, 2014.

[60] T. Kojima, C. Moraes, S. P. Cavnar, G. D. Luker, and S. Takayama, "Surface-templated hydrogel patterns prompt matrix-dependent migration of breast cancer cells towards chemokine-secreting cells," *Acta Biomater.*, vol. 13, pp. 68–77, 2015.

[61] M. C. Frame and A. Serrels, "FAK to the Rescue: Activated Stroma Promotes a 'Safe Haven' for BRAF-Mutant Melanoma Cells by Inducing FAK Signaling," *Cancer Cell*, vol. 27, no. 4, pp. 429–431, 2015.

[62] C. H. K. and S. I. Sandler, "Effects of Polydispersivity on the Phase Behavior of Aqueous Two-Phase Polymer Systems," *Macromolecules*, vol. 21, pp. 3088–3095, 1988.

[63] Y. Guan, T. H. Lilley, M. N. Garcia-Lisbona, and T. E. Treffry, "New approaches to aqueous polymer systems: Theory, thermodynamics and applications to biomolecular separations," *Pure Appl. Chem.*, vol. 67, no. 6, pp. 955–962, 1995.

[64] J. a. Asenjo and B. a. Andrews, "Aqueous two-phase systems for protein separation: Phase separation and applications," *J. Chromatogr. A*, vol. 1238, no. September 2011, pp. 1–10, 2012.

[65] P. Å. Albertsson, *Partition of Cell Particles and Macromolecules: Distribution and Fractionation of Cells, Viruses, Microsomes, Proteins, Nucleic Acids, and Antigen-antibody Complexes in Aqueous Polymer Two-phase Systems*. J. Wiley, 1960.

[66] N. Pietruszka, I. Y. Galaev, A. Kumar, Z. K. Brzozowski, and B. Mattiasson, "New polymers forming aqueous two-phase polymer systems.," *Biotechnol. Prog.*, vol. 16, no. 3, pp. 408–15, Jan. .

[67] D. Fisher, "The separation of cells and organelles by partitioning in two-polymer aqueous phases.," *Biochem. J.*, vol. 196, no. 1, pp. 1–10, Apr. 1981.

[68] C. H. Kang and S. I. Sandler, "Effects of polydispersivity on the phase behavior of the aqueous two-phase polymer systems," *Macromolecules*, vol. 21, no. 10, pp. 3088–3095, 1988.

[69] M. Rito-Palomares and L. Cueto, "Effect of biological suspensions on the position of the binodal curve in aqueous two-phase systems," *J. Chromatogr. B Biomed. Sci. Appl.*, vol. 743, no. 1–2, pp. 5–12, 2000.

[70] J. D. E. and D. C. S. H. Cabezas, "A Statistical Mechanical Model of Aqueous Two-Phase Systems," *Fluid Phase Equilib.*, vol. 53, no. 1986, pp. 453–462, 1989.

[71] Å. Gustafsson, H. Wennerström, and F. Tjerneld, "The nature of phase separation in aqueous two-polymer systems," *Polymer (Guildf).*, vol. 27, no. 11, pp. 1768–1770, 1986.

[72] A. M. Bollen and J. A. Wesselingh, "The behaviour of the binodal and spinodal curves for near-binary compositions," *Fluid Phase Equilib.*, vol. 149, no. 1–2, pp. 17–25, 1998.

[73] D. J. Walsh and S. Rostami, "Binodal and spinodal curves: a simulation for various high polymer mixtures," *Polymer (Guildf).*, vol. 26, no. 3, pp. 418–422, 1985.

[74] H.-O. Johansson, E. Feitosa, and A. P. Junior, "Phase Diagrams of the Aqueous Two-Phase Systems of Poly(ethylene glycol)/Sodium Polyacrylate/Salts," *Polymers (Basel).*, vol. 3, no. 1, pp. 587–601, 2011.

[75] J. Schindler and H. G. Nothwang, "Aqueous polymer two-phase systems: Effective tools for plasma membrane proteomics," *Proteomics*, vol. 6, no. 20, pp. 5409–5417, 2006.

[76] C. H. Kang, "Phase Behavior of Aqueous Two-Polymer Systems," *Fluid Phase Equilib.*, vol. 38, pp. 245–272, 1987.

[77] D. Forciniti, C. K. Hall, and M. R. Kula, "Interfacial tension of polyethyleneglycol-dextran-water systems: influence of temperature and polymer molecular weight," *J. Biotechnol.*, vol. 16, no. 3–4, pp. 279–296, 1990.

[78] B. Y. W. D. Bonner, "Experimental Determination of Binodal Curves," *Phys. Rev*, vol. 27, no. 3, pp. 739–789, 1895.

[79] E. Edmond and a G. Ogston, “An approach to the study of phase separation in ternary aqueous systems.,” *Biochem. J.*, vol. 109, no. 4, pp. 569–576, 1968.

[80] K. T. and T. A. I. Inamura, “Effects of Molecular Weight on the Phase Equilibrium of a Polyvinyl Alcohol-Polyethylene Glycol Water System,” *Polym. J.*, vol. 16, no. 8, pp. 657–660, 1984.

[81] Y. Wu, M. Pereira, and A. Venancio, “Separation of endo-polygalacturonase using aqueous two-phase partitioning,” vol. 929, pp. 23–29, 2001.

[82] J. P. Frampton, B. M. Leung, E. L. Bingham, S. C. Lesher-Perez, J. D. Wang, H. T. Sarhan, M. E. H. El-Sayed, S. E. Feinberg, and S. Takayama, “Rapid Self-Assembly of Macroscale Tissue Constructs at Biphasic Aqueous Interfaces,” *Adv. Funct. Mater.*, vol. 25, no. 2, pp. 410–423, 2015.

[83] J. C. Merchuk, B. a Andrews, and J. a Asenjo, “Aqueous two-phase systems for protein separation. Studies on phase inversion.,” *J. Chromatogr. B. Biomed. Sci. Appl.*, vol. 711, no. 1–2, pp. 285–293, 1998.

[84] C. Q. S. and B. E. Eichinger, “Phase Diagrams of Binary Polymer Solutions and Blends,” vol. 200247, pp. 1655–1661, 1991.

[85] S. Raja, V. R. Murty, V. Thivaharan, V. Rajasekar, and V. Ramesh, “Aqueous Two Phase Systems for the Recovery of Biomolecules – A Review,” *Sci. Technol.*, vol. 1, no. 1, pp. 7–16, 2012.

[86] D. F. Gerson and D. Scheer, “Cell surface energy, contact angles and phase partition. III. Adhesion of bacterial cells to hydrophobic surfaces.,” *Biochim. Biophys. Acta*, vol. 602, no. 3, pp. 506–510, 1980.

[87] A. Hoffman, “Lecture on Contact Angles, May 4, 2005 A) Liquid and Solid Surface Energies B) Liquid Contact Angles on Solid Surfaces Prof. Allan S. Hoffman,” *Lect. Contact Angl.*, 2005.

[88] G. Bracco and B. Holst, *Surface science techniques*, vol. 51, no. 1. 2013.

[89] H. B. Eral, D. J. C. M. ’T Mannetje, and J. M. Oh, “Contact angle hysteresis: A review of fundamentals and applications,” *Colloid Polym. Sci.*, vol. 291, no. 2, pp. 247–260, 2013.

[90] W. Anderson, “Wettability Literature Survey- Part 2: Wettability Measurement,” *J. Pet. Technol.*, vol. 38, no. 11, pp. 1,246–1,262, Nov. 1986.

[91] A. Krishnan, Y.-H. Liu, P. Cha, R. Woodward, D. Allara, and E. A. Vogler, “An evaluation of methods for contact angle measurement.,” *Colloids Surf. B. Biointerfaces*, vol. 43, no. 2, pp. 95–8, Jun. 2005.

[92] O. Río and A. Neumann, “Axisymmetric Drop Shape Analysis: Computational Methods for the Measurement of Interfacial Properties from the Shape and Dimensions of Pendant and Sessile Drops.,” *J. Colloid Interface Sci.*, vol. 196, no. 2, pp. 136–147, Dec. 1997.

[93] A. Bateni, S. S. Susnar, A. Amirfazli, and A. W. Neumann, “A high-accuracy polynomial fitting approach to determine contact angles,” *Colloids Surfaces A Physicochem. Eng. Asp.*, vol. 219, no. 1–3, pp. 215–231, Jun. 2003.

[94] A. Kalantarian, R. David, J. Chen, and A. W. Neumann, “Simultaneous measurement of contact angle and surface tension using axisymmetric drop-shape analysis-no apex (ADSA-NA).,” *Langmuir*, vol. 27, no. 7, pp. 3485–95, Apr. 2011.

[95] A. Kalantarian, R. David, and A. W. Neumann, “Methodology for high accuracy contact angle measurement.,” *Langmuir*, vol. 25, no. 24, pp. 14146–54, Dec. 2009.

[96] B.-B. Lee, P. Ravindra, and E.-S. Chan, “A Critical Review: Surface And Interfacial Tension Measurement By The Drop Weight Method,” *Chem. Eng. Commun.*, vol. 195, no. 8, pp. 889–924, Apr. 2008.

[97] A. Agrawal, “Surface Tension of Polymers,” *Mass Inst. Technol.*, vol. 54, pp. 1–29, 2005.

[98] C. Zhang and P. Carloni, “Salt effects on water/hydrophobic liquid interfaces: a molecular dynamics study,” *J. Phys. Condens. Matter*, vol. 24, no. 12, p. 124109, 2012.

[99] M. T. H. and C. H. Byers, “An Advaced Technique for Interfacial Tensio Measurement in Liquid-Liquid systems,” 1989.

[100] J. Drelich, “Measurement of Interfacial Tension in Fluid-Fluid Systems,” *Encycl. Surf. Colloid Sci.*, vol. 18, pp. 3152–3166, 2002.

[101] P. L. Luque-Escamilla, “Measurement of surface tension and contact angle using entropic edge,” *Image (IN).*, vol. 12, pp. 288–298, 2001.

[102] W. Schirmer, “Physical Chemistry of Surfaces,” *Zeitschrift für Phys. Chemie*, vol. 210, no. Part_1, pp. 134–135, 1999.

[103] B. Gash and D. R. Parrish, “A Simple Spinning-Drop Interfacial Tensiometer,” *J. Pet. Technol.*, vol. 29, no. 01, pp. 30–31, Apr. 2013.

[104] H. H. H. and D. D. Joseph, “Evolution of a Liquid Drop in a Spinning Drop Tensiometer,” *J. Colloid Interface Sci.*, vol. 162, pp. 331–339, 1994.

[105] H.-J. Butt, K. Graf, and M. Kappl, “Physics and Chemistry of Interfaces,” in *Wiley-VCH GmbH & Co. KGaA*, 2003, pp. 118–144.

[106] P. Cheng, D. Li, L. Boruvka, Y. Rotenberg, and A. W. Neumann, “Automation of axisymmetric drop shape analysis for measurements of interfacial tensions and contact angles,” *Colloids and Surfaces*, vol. 43, no. 2, pp. 151–167, Jan. 1990.

[107] P. Cheng and A. W. Neumann, “Computational evaluation of axisymmetric drop shape analysis-profile (ADSA-P),” *Colloids and Surfaces*, vol. 62, no. 4, pp. 297–305, Mar. 1992.

[108] O. Río and A. Neumann, “Axisymmetric Drop Shape Analysis: Computational Methods for the Measurement of Interfacial Properties from the Shape and Dimensions of Pendant and Sessile Drops.,” *J. Colloid Interface Sci.*, vol. 196, no. 2, pp. 136–147, 1997.

[109] M. Hoorfar and A. W Neumann, “Recent progress in axisymmetric drop shape analysis (ADSA).,” *Adv. Colloid Interface Sci.*, vol. 121, no. 1–3, pp. 25–49, Sep. 2006.

[110] S. J. K. Neumann, A.W., “Applied Surface Thermodynamics,” in *Surfactant Science Series; v.63*, CRC Press, 1996, pp. 300–400.

[111] R. H. Whitehead and P. S. Robinson, “Establishment of conditionally immortalized epithelial cell lines from the intestinal tissue of adult normal and transgenic mice.,” *Am. J. Physiol. Gastrointest. Liver Physiol.*, vol. 296, no. 3, pp. G455–60, Mar. 2009.

[112] C. R. Mace, O. Akbulut, A. A. Kumar, N. D. Shapiro, R. Derda, M. R. Patton, and G. M. Whitesides, “Aqueous multiphase systems of polymers and surfactants provide self-assembling step-gradients in density.,” *J. Am. Chem. Soc.*, vol. 134, no. 22, pp. 9094–7, Jun. 2012.

[113] A. M. Bollen and J. A. Wesselingh, “The behaviour of the binodal and spinodal curves for near-binary compositions,” *Fluid Phase Equilib.*, vol. 149, no. 1–2, pp. 17–25, Aug. 1998.

[114] H. Cabezas, J. D. Evans, and D. C. Szlag, “A statistical mechanical model of aqueous two-phase systems,” *Fluid Phase Equilib.*, vol. 53, pp. 453–462, Dec. 1989.

[115] T. Croll, P. D. Munro, D. J. Winzor, M. Trau, and L. K. Nielsen, “Quantitative prediction of phase diagrams for polymer partitioning in aqueous two-phase systems,” *J. Polym. Sci. Part B Polym. Phys.*, vol. 41, no. 5, pp. 437–443, Mar. 2003.

[116] Y. Liu, R. Lipowsky, and R. Dimova, "Concentration dependence of the interfacial tension for aqueous two-phase polymer solutions of dextran and polyethylene glycol," *Langmuir*, vol. 28, no. 8, pp. 3831–3839, 2012.

[117] R. Ploeger, S. Musso, and O. Chiantore, "Contact angle measurements to determine the rate of surface oxidation of artists' alkyd paints during accelerated photo-ageing," *Prog. Org. Coatings*, vol. 65, no. 1, pp. 77–83, Apr. 2009.

[118] W. Shen, Y. Filonanko, Y. Truong, I. . Parker, N. Brack, P. Pigram, and J. Liesegang, "Contact angle measurement and surface energetics of sized and unsized paper," *Colloids Surfaces A Physicochem. Eng. Asp.*, vol. 173, no. 1–3, pp. 117–126, Nov. 2000.

[119] Y. Rotenberg, L. Boruvka, and A. . Neumann, "Determination of surface tension and contact angle from the shapes of axisymmetric fluid interfaces," *J. Colloid Interface Sci.*, vol. 93, no. 1, pp. 169–183, May 1983.

[120] H. Tavana, F. Simon, K. Grundke, D. Y. Kwok, M. L. Hair, and A. W. Neumann, "Interpretation of contact angle measurements on two different fluoropolymers for the determination of solid surface tension.," *J. Colloid Interface Sci.*, vol. 291, no. 2, pp. 497–506, Dec. 2005.

[121] H. Tavana, C. N. C. Lam, K. Grundke, P. Friedel, D. Y. Kwok, M. L. Hair, and A. W. Neumann, "Contact angle measurements with liquids consisting of bulky molecules.," *J. Colloid Interface Sci.*, vol. 279, no. 2, pp. 493–502, Nov. 2004.

[122] M. G. Cabezas, A. Bateni, J. M. Montanero, and A. W. Neumann, "A new method of image processing in the analysis of axisymmetric drop shapes," *Colloids Surfaces A Physicochem. Eng. Asp.*, vol. 255, no. 1–3, pp. 193–200, Mar. 2005.

[123] E. Atefi, J. A. Mann, and H. Tavana, "A robust polynomial fitting approach for contact angle measurements.," *Langmuir*, vol. 29, no. 19, pp. 5677–88, May 2013.

[124] H. Tavana, D. Jehnichen, K. Grundke, M. L. Hair, and A. W. Neumann, "Contact angle hysteresis on fluoropolymer surfaces.," *Adv. Colloid Interface Sci.*, vol. 134–135, pp. 236–48, Oct. 2007.

[125] H. Tavana, N. Petong, A. Hennig, K. Grundke, and A. W. Neumann, "Contact Angles and Coating Film Thickness," *J. Adhes.*, vol. 81, no. 1, pp. 29–39, Sep. 2006.

[126] H. Tavana, R. Gitiafroz, M. L. Hair, and A. W. Neumann, "Determination of Solid Surface Tension from Contact Angles: The Role of Shape and Size of Liquid Molecules," *J. Adhes.*, vol. 80, no. 8, pp. 705–725, Aug. 2010.

[127] M. Gille, Y. Gorbacheva, A. Hahn, V. Polevikov, and L. Tobiska, “Simulation of a pending drop at a capillary tip,” *Commun. Nonlinear Sci. Numer. Simul.*, vol. 26, no. 3, pp. 137–151, 2015.

[128] S. M. I. Saad and a. W. Neumann, “Total Gaussian curvature, drop shapes and the range of applicability of drop shape techniques,” *Adv. Colloid Interface Sci.*, vol. 204, pp. 1–14, 2014.

[129] M. Żenkiewicz, “Methods for the calculation of surface free energy of solids,” *J. Achiev. Mater. Manuf. Eng.*, vol. 24, no. 1, pp. 137–145, 2007.

[130] P. Than, L. Preziosi, D. . Josephl, and M. Arney, “Measurement of interfacial tension between immiscible liquids with the spinning road tensiometer,” *Journal of Colloid and Interface Science*, vol. 124, no. 2. pp. 552–559, 1988.

[131] D. Y. Kwok, W. Hui, R. Lin, and a W. Neumann, “Liquid-Fluid Interfacial Tensions Measured by Axisymmetric Drop Shape Analysis: Comparison between the Pattern of Interfacial Tensions of Liquid-Liquid and Solid-Liquid Systems,” *Langmuir*, vol. 11, no. 7, pp. 2669–2673, 1995.

[132] S. M. I. Saad, Z. Policova, E. J. Acosta, and a. W. Neumann, “Range of validity of drop shape techniques for surface tension measurement,” *Langmuir*, vol. 26, no. 17, pp. 14004–14013, 2010.

[133] E. Atefi, J. A. Mann, and H. Tavana, “Ultralow interfacial tensions of aqueous two-phase systems measured using drop shape.,” *Langmuir*, vol. 30, no. 32, pp. 9691–9, Aug. 2014.

[134] J. J. Jasper, “The Surface Tension of Pure Liquid Compounds,” *J. Phys. Chem. Ref. Data*, vol. 1, no. 4, p. 841, Oct. 1972.

[135] H. Tavana, B. Mosadegh, P. Zamankhan, J. B. Grotberg, and S. Takayama, “Microprinted feeder cells guide embryonic stem cell fate.,” *Biotechnol. Bioeng.*, vol. 108, no. 10, pp. 2509–16, Oct. 2011.

[136] S. Lemmo, S. Nasrollahi, and H. Tavana, “Aqueous biphasic cancer cell migration assay enables robust, high-throughput screening of anti-cancer compounds.,” *Biotechnol. J.*, vol. 9, no. 3, pp. 426–34, Mar. 2014.

[137] H. Tavana, B. Mosadegh, and S. Takayama, “Polymeric aqueous biphasic systems for non-contact cell printing on cells: engineering heterocellular embryonic stem cell niches.,” *Adv. Mater.*, vol. 22, no. 24, pp. 2628–31, Jul. 2010.

[138] H. Tavana, A. Jovic, B. Mosadegh, Q. Y. Lee, X. Liu, K. E. Luker, G. D. Luker, S. J. Weiss, and S. Takayama, “Nanolitre liquid patterning in aqueous environments

for spatially defined reagent delivery to mammalian cells.," *Nat. Mater.*, vol. 8, no. 9, pp. 736–41, Oct. 2009.

[139] S. D. Hann, M. Goulian, D. Lee, and K. J. Stebe, "Trapping and assembly of living colloids at water-water interfaces.," *Soft Matter*, vol. 11, no. 9, pp. 1733–8, Mar. 2015.

[140] H. Umakoshi, R. Kuboi, and I. Komasawa, "Control of partitioning of bacterial cells and characterization of their surface properties in aqueous two-phase systems," *J. Ferment. Bioeng.*, vol. 84, no. 6, pp. 572–578, Jan. 1997.

[141] G. Mehta, A. Y. Hsiao, M. Ingram, G. D. Luker, and S. Takayama, "Opportunities and challenges for use of tumor spheroids as models to test drug delivery and efficacy.," *J. Control. Release*, vol. 164, no. 2, pp. 192–204, Dec. 2012.

[142] H. Qi, Y. Du, L. Wang, H. Kaji, H. Bae, and A. Khademhosseini, "Patterned differentiation of individual embryoid bodies in spatially organized 3D hybrid microgels.," *Adv. Mater.*, vol. 22, no. 46, pp. 5276–81, Dec. 2010.

[143] E. Atefi, S. Lemmo, D. Fyffe, G. D. Luker, and H. Tavana, "High Throughput, Polymeric Aqueous Two-Phase Printing of Tumor Spheroids.," *Adv. Funct. Mater.*, vol. 24, no. 41, pp. 6509–6515, Nov. 2014.

[144] M. W. Tibbitt and K. S. Anseth, "Hydrogels as extracellular matrix mimics for 3D cell culture.," *Biotechnol. Bioeng.*, vol. 103, no. 4, pp. 655–63, Jul. 2009.

[145] N. E. Timmins and L. K. Nielsen, "Generation of multicellular tumor spheroids by the hanging-drop method.," *Methods Mol. Med.*, vol. 140, pp. 141–51, Jan. 2007.

[146] J. P. F. A. B. Yeatts, "Bone tissue engineering bioreactors: Dynamic culture and the influence of shear stress," *Bone*, vol. 48, pp. 171–181, 2011.

[147] S. Breslin and L. O'Driscoll, "Three-dimensional cell culture: the missing link in drug discovery.," *Drug Discov. Today*, vol. 18, no. 5–6, pp. 240–9, Mar. 2013.

[148] A. Y. Hsiao, Y.-C. Tung, X. Qu, L. R. Patel, K. J. Pienta, and S. Takayama, "384 hanging drop arrays give excellent Z-factors and allow versatile formation of co-culture spheroids.," *Biotechnol. Bioeng.*, vol. 109, no. 5, pp. 1293–304, May 2012.

[149] M.-H. Wu, S.-B. Huang, Z. Cui, Z. Cui, and G.-B. Lee, "Development of perfusion-based micro 3-D cell culture platform and its application for high throughput drug testing," *Sensors Actuators B Chem.*, vol. 129, no. 1, pp. 231–240, Jan. 2008.

[150] K. E. Sung, G. Su, C. Pehlke, S. M. Trier, K. W. Eliceiri, P. J. Keely, A. Friedl, and D. J. Beebe, "Control of 3-dimensional collagen matrix polymerization for

reproducible human mammary fibroblast cell culture in microfluidic devices.," *Biomaterials*, vol. 30, no. 27, pp. 4833–41, Sep. 2009.

[151] I. Meyvantsson and D. J. Beebe, "Cell culture models in microfluidic systems.," *Annu. Rev. Anal. Chem. (Palo Alto. Calif).*, vol. 1, pp. 423–49, Jan. 2008.

[152] J. W. Haycock, "3D cell culture: a review of current approaches and techniques.," *Methods Mol. Biol.*, vol. 695, pp. 1–15, Jan. 2011.

[153] E. Carletti, A. Motta, and C. Migliaresi, "Scaffolds for tissue engineering and 3D cell culture.," *Methods Mol. Biol.*, vol. 695, pp. 17–39, Jan. 2011.

[154] J. W. Haycock, Ed., "3D Cell Culture," vol. 695, Totowa, NJ: Humana Press, 2011.

[155] T. Chou, "Theoretical Basis , Experimental Design , and Computerized Simulation of Synergism and Antagonism in Drug Combination Studies," pp. 621–681, 2007.

[156] B. A. Justice, N. A. Badr, and R. A. Felder, "3D cell culture opens new dimensions in cell-based assays.," *Drug Discov. Today*, vol. 14, no. 1–2, pp. 102–7, Jan. 2009.

[157] J. Zhang, T. Chung, and K. Oldenburg, "A Simple Statistical Parameter for Use in Evaluation and Validation of High Throughput Screening Assays.," *J. Biomol. Screen.*, vol. 4, no. 2, pp. 67–73, Jan. 1999.

[158] R. Ismail-khan and M. M. Bui, "A Review of Triple-Negative Breast Cancer," *Cancer Control*, vol. 17, no. 3, pp. 173–176, 2010.

[159] "Comprehensive molecular portraits of human breast tumours.," *Nature*, vol. 490, no. 7418, pp. 61–70, Oct. 2012.

APPENDIX

OPTIMIZATION PROCEDURE AND FORMING PHASE COMPOSITIONS

The total error is initially defined as $E = \sqrt{\left(\sum_{i=1}^{n} \varepsilon_{1,i}\right)^2 + \left(\sum_{i=1}^{n} \varepsilon_{2,i}\right)^2}$, with the same weight for $\varepsilon_{1,i}$ and $\varepsilon_{2,i}$. This total error is modified having weight fraction of w as $E = \sqrt{\left(\sum_{i=1}^{n} \varepsilon_{1,i}\right)^2 + \left(\sum_{i=1}^{n} w\varepsilon_{2,i}\right)^2}$, where a weight factor (w) is included to balance the weight of $\varepsilon_{1,i}$ and $\varepsilon_{2,i}$ in the total error (E). The value of w is determined through a multi-objective optimization approach in Matlab (Mathworks).

For a given ATPS such as the PEG 35k – DEX 500k ATPS, $\sum_{i=1}^{n} \varepsilon_{1,i}$ gives the sum of differences between exact mass of PEG (known from preparing stock solutions) and estimated mass quantities of PEG from equilibrated phases of all two-phase solutions made with varying concentrations of polymers (calculated from steps 1-6 of the manuscript). Similarly, $\sum_{i=1}^{n} \varepsilon_{2,i}$ provides this quantity for DEX. A multi-objective optimization method is implemented to optimize the total error (E). This method optimizes $\varepsilon_{1,i}$ and $\varepsilon_{2,i}$ independently and returns a set of optimized E-values (Figure A-1). Each point in this figure represents optimized $\sum_{i=1}^{n} \varepsilon_{1,i}$ and $\sum_{i=1}^{n} \varepsilon_{2,i}$ resulting from the multi-objective optimization. In principle, each of these points may be selected as a solution of the multi-objective optimization. To facilitate this, we defined a criterion as minimized total error (E); according to the Figure A-1 inset, the points representing a minimum E value could be selected. At each of these points in Figure A-1, $\sum_{i=1}^{n} \varepsilon_{1,i} \cong 4 \sum_{i=1}^{n} \varepsilon_{2,i}$. Therefore to

increase the accuracy of results, the total error is modified by including a weight factor of w=2 to $E = \sqrt{\left(\sum_{i=1}^{n} \varepsilon_{1,i}\right)^2 + \left(\sum_{i=1}^{n} w\varepsilon_{2,i}\right)^2}$. Then the entire optimization process (steps 1-6 of the manuscript) is repeated to resolve the coefficients of the binodal equation.

Table A-1 Concentrations of PEG and DEX in stock solutions, density of stock solutions, and volume and density of equilibrated phases of two-phase solutions made with the PEG 8k – DEX 500k ATPS. Each solution was made using 5 mL of its constituting aqueous phases (total volume=10 mL).

Concentration of stock solutions		Density of stock solutions		Volume of equilibrated phases		Density of equilibrated phases	
DEX solution %(w/v)	PEG solution %(w/v)	DEX solution (g/mL)	PEG solution (g/mL)	Bottom phase (mL)	Top phase (mL)	Bottom phase (g/mL)	Top phase (g/mL)
10	8	1.034	1.012	4.0	6.0	1.037	1.011
11.9	7	1.042	1.009	4.8	5.2	1.038	1.011
12.24	7.2	1.043	1.010	4.9	5.1	1.040	1.011
12.92	7.6	1.046	1.010	4.6	5.4	1.046	1.012
13.6	8	1.048	1.012	4.5	5.5	1.050	1.012
15	7	1.054	1.009	5.6	4.4	1.047	1.012
15	8.8	1.054	1.012	4.7	5.3	1.058	1.013
17	10	1.066	1.014	4.6	5.4	1.070	1.014
20	5	1.074	1.005	7.4	2.6	1.049	1.012

Table A-2 Concentrations of PEG and DEX in stock solutions, density of stock solutions, and volume and density of equilibrated phases of two-phase solutions made with the PEG 35k – DEX 40k ATPS. Each solution was made using 5 mL of its constituting aqueous phases (total volume=10 mL).

Concentration of stock solutions		Density of stock solutions		Volume of equilibrated phases		Density of equilibrated phases	
DEX solution %(w/v)	PEG solution %(w/v)	DEX solution (g/mL)	PEG solution (g/mL)	Bottom phase (mL)	Top phase (mL)	Bottom phase (g/mL)	Top phase (g/mL)
8	8	1.028	1.011	1.2	8.8	1.041	1.013
9	9	1.031	1.012	2.2	7.8	1.044	1.014
10	10	1.038	1.015	2.8	7.2	1.045	1.014
12	12	1.046	1.018	3	7	1.064	1.015
14	14	1.054	1.021	6.8	3.2	1.074	1.016
16	16	1.062	1.025	6.7	3.3	1.085	1.018
18	18	1.068	1.029	6.6	3.4	1.095	1.021
20	20	1.074	1.032	6.5	3.5	1.108	1.024

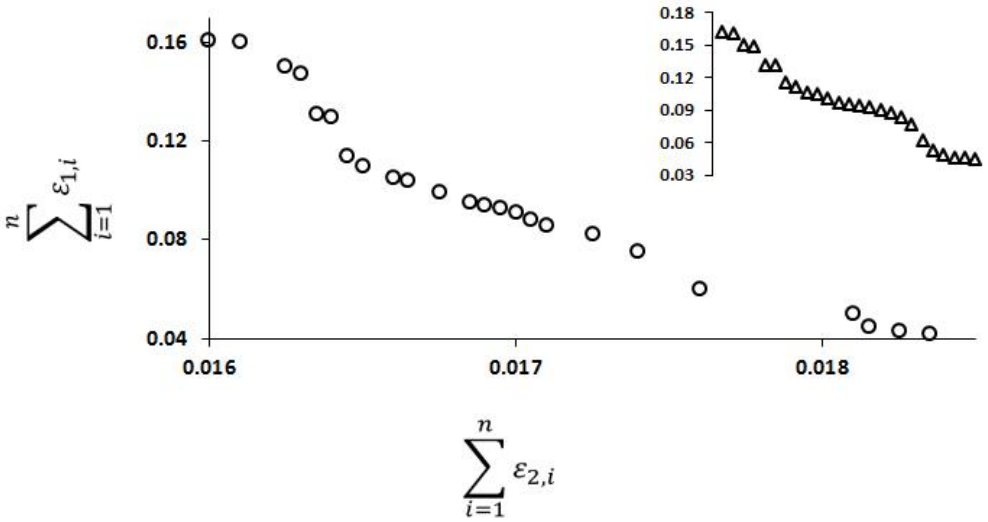

Figure A-1 Variations of errors in the mass balance of PEG ($\sum_{i=1}^{n} \varepsilon_{1,i}$) and DEX ($\sum_{i=1}^{n} \varepsilon_{2,i}$) is shown during the multi-objective optimization of the errors. Data correspond to the ATPS made with PEG 35k – DEX 500k ATPS. Corresponding to each point, there is a total error (E) shown in the inset figure.